VELOCITY PROFILES AND SKIN FRICTION ON A RIBLETTED FLAT PLATE IN ADVERSE PRESSURE GRADIENT

THESIS

Richard D. Branam, Captain, USAF

AFIT/GAE/ENY/97D-01

DEPARTMENT OF THE AIR FORCE
AIR UNIVERSITY
AIR FORCE INSTITUTE OF TECHNOLOGY

Wright-Patterson Air Force Base, Ohio

AFIT/GAE/ENY/97D-01

VELOCITY PROFILES AND SKIN FRICTION ON A RIBLETTED FLAT PLATE IN ADVERSE PRESSURE GRADIENT

THESIS

Richard D. Branam, Captain, USAF

AFIT/GAE/ENY/97D-01

The views expressed in this thesis are those of the author and do not reflect the official policy or position of the Department of Defense or the U.S. Government.

AFIT/GAE/ENY/97D-01

VELOCITY PROFILES AND SKIN FRICTION ON A RIBLETTED FLAT PLATE IN ADVERSE PRESSURE GRADIENT

Richard D. Branam, B.S., M.S.
Captain, USAF

Approved:

Chairman	12/2/97 date
	12/2/97 date
	12/2/97 date

VELOCITY PROFILES AND SKIN FRICTION ON A RIBLETTED FLAT PLATE IN ADVERSE PRESSURE GRADIENT

THESIS

Presented to the Faculty of the Graduate School of Engineering

Air Education and Training Command

In Partial Fulfillment of the Requirements for the Degree of

Master of Science in Aeronautical Engineering

Richard D. Branam, B.S.A.E

Captain, USAF

November, 97

Acknowledgments

I would like to show my appreciation to my advisor, Dr. Paul I. King. His guidance and knowledge taught me a great deal and helped me accomplish this research project. I would like to also thank Jay Anderson, Dan Rioux and the other lab technicians for their help in learning how to use the equipment and the support they provided in completing this research task.

I would also like to acknowledge the tireless understanding provided by my wife, Karen, during the time I spent at the Air Force Institute of Technology. Her support made it possible to complete this research project in a timely and productive manner.

Richard D. Branam

Table of Contents

List of Figures

List of Tables

List of Symbols

Symbol

AFIT	Air Force Institute of Technology
BSA	Burst Spectrum Analyzer
LDA	Laser Doppler Anemometery

Arabic Symbols

B	Constant used in log-law relationships for turbulent boundary layer profiles
C_f	Local skin friction coefficient
f	Flat plate boundary layer variable
f'	First derivative of the flat plate boundary layer variable (u/U)
f''	Second derivative of the flat plate boundary layer variable
f'''	Third derivative of the flat plate boundary layer variable
F	Log-law wall roughness parameter
h	Riblet height (mm)
h^+	Riblet height non-dimensionalized by wall variables, u_τ and ν
H	Shape parameter for turbulent boundary layer profiles
K	Coefficient for velocity power law relationship
m	Exponent for velocity power law relationship
n	Number of samples
p	Static pressure (Pa)
p_e	Static pressure in the freestream (Pa)
Re_x	Local Reynold's number

Re_θ	Reynold's number based on momentum thickness
s	Riblet spacing, sample standard deviation
s	Sample standard deviation
s^+	Riblet spacing non-dimensionalized by wall variables, u_τ and ν
t	Student t distribution variable
T	Turbulence intensity (%)
u	Local streamwise velocity (m/s)
u	Average local streamwise velocity (m/s)
u_τ	Friction velocity (m/s)
u^+	Local streamwise velocity nondimensionalized by wall variables, u_τ and ν
u'	Streamwise velocity fluctuation, rms (m/s)
U	Freestream, streamwise velocity (m/s)
U(x)	Local freestream, streamwise velocity (m/s)
v	Local normal velocity (m/s)
v'	Normal velocity fluctuation, rms (m/s)
w	Local spanwise velocity (m/s)
w'	Spanwise velocity fluctuation, rms (m/s)
x	Streamwise coordinate (m)
x_i	Sample value
X	Chauvenet statistic
y	Normal coordinate (m)
y_o	Virtual origin (m)
y^+	Normal coordinate non-dimensionalized by wall variables, u_τ and ν
z	Spanwise coordinate (m)

z^+	Spanwise coordinate non-dimensionalized by wall variables, u_τ and ν
$\frac{d(\_)}{dx}$	Change in the x direction, derivative with respect to x
$\frac{d(\_)}{dy}$	Change in the y direction, derivative with respect to y
$(\ )_i$	The ith measurement
$(\ )_w$	Evaluated near the wall
$< >$	Averaged value, mean

Greek Symbols

α	Riblet peak inclination (deg), confidence interval parameter
β	Falkner-Skan pressure gradient parameter
β_c	Clauser equilibrium parameter
δ	Boundary layer thickness (m)
δ^*	Boundary layer displacement thickness (m)
Δt	Dwell time for seeding particles in LDA measurement volume (s)
κ	Log-law constant for turbulent boundary layer profiles
η	Non-dimensional coordinate for laminar boundary layer (Blassius variable)
θ	Momentum thickness (m)
ρ	Fluid density (kg/m^3)
μ	Fluid viscosity (kg/m-s)
ν	Kinemtic fluid viscosity (m^2/s)
Π	Coles wake parameter
σ	Standard deviation
τ_w	Local shear stress at the wall (Pa)

Abstract

This project investigated the flow field characteristics over a flat, ribletted plate and the effectsof an adverse pressure gradient on this flow field. Testing examined the development of the flow over the ribletted plate from laminar through fully turbulent flow fields. The flow field states (laminar, transitional, and turbulent) were determined using local turbulence intensity values and boundary layer profiles. Several parameters were examined to help better describe the flow characteristics, boundary layer profiles, and influence on skin friction drag. The skin friction drag coefficients were calculated using a numerical integration technique to determine an average value and scaled to the planform area of the plate to compare results with smooth plate values. Although the geometry and flow conditions produced a drag augmenting case, skin friction followed trends described by the other flow parameters; streamwise velocity, Reynolds stress, etc. At locations where the boundary layer developed in the riblet valley, the skin friction was higher. As the flow developed to transitional and fully turbulent, higher values were also experienced. For the zero pressure gradient and mild adverse pressure gradient, counter rotating vortices developed in the riblet valley. This more organized motion also had slightly reduced skin friction below the transitional flow field for the plate as well.

Other significant findings included boundary layer behavior and secondary velocity structures. The laminar boundary layers also conformed to a modified similarity solution. Secondary velocity structures included counter rotating vortices in the fully turbulent flow field. These vortices dissipated with increased adverse pressure gradient.

1. Introduction

1.1 Background

Often in aerodynamic applications, the reduction of skin friction drag and fluid flow control are of primary importance. Many methods have been employed to control these aspects of fluid flow over a surface. The use of riblets has been employed in several applications and research projects to reduce drag and the fluid flow. Riblets are longitudinal grooves in the surface oriented primarily in the stream wise direction of the fluid flow. Practical applications could include aerodynamic surfaces, turbo jet/fan engine components (inlet, nozzle, compressor blades, turbine blades), or perhaps even automobile surfaces.

Much research has been centered around riblet flow interactions with turbulent boundary layer profiles to investigate if the flow stayed attached to the aerodynamic surface. The investigators also hoped to reduce the higher skin friction drag seen in turbulent boundary layers. Experiments by Walsh (1990) have shown skin friction drag reductions of six to eight percent ($s^+ = 12$). Although Walsh (1990) experimented with several different cross sections for riblets, the most commonly used are the V groove. The V groove offers the ability to easily fabricate and reproduce as needed while providing much of the benefits seen from riblets.

Past research in the Air Force Institute of Technology (AFIT) Boundary Layer Research Facility included two main projects. Rothenflue (1996) investigated the effects of riblets on flat and constant curvature plates under a zero pressure gradient. The primary purpose of his investigation centered on the effects on Görtler Vortex formation and control. Since Görtler vortices are responsible for a significant portion of the skin friction drag (20 - 40% , Rothenflue, 1996), control of these aerodynamic structures could be quite significant. Another research project considered the

effects on boundary layers in an adverse pressure gradient (Dement, 1996). The investigator's measured data showed turbulent flow characteristics generated over the ribletted flat plate.

The research project described in this thesis continued the work of these previous experiments and investigated the effect of the ribletted plate in a zero pressure gradient as well as an adverse pressure gradient. Flow locations on the plate were chosen in order to determine the aerodynamic flow characteristics formed in laminar, transitional and turbulent boundary layers. The project employed only flat plates for the investigation.

1.2 Importance of Research

This project was designed to examine the flow characteristics caused by riblets over a flat plate. Although much research has been accomplished on riblets, several areas of interest have yet to be explored. These areas include riblet effects on flows under an adverse pressure gradient. While several active boundary layer controls have proved to be significantly useful for this specific application, a more passive and less complex method would be preferred as an engineering solution. By employing riblets on aerodynamic surfaces, such a solution might be possible. This research helps provide a building block toward a better understanding of a potential boundary layer control which could have significant benefit for more realistic applications.

Some of these benefits include fuel economy for commercial aircraft and the victory of the 1991 America's cup for example. The commercial aircraft industry could significantly benefit from a small decrease in overall drag in fuel economy. Even for just one year of an aircraft fleet, the savings could be significant (Walsh, 1990). The America's Cup regatta winner in 1991 had riblets incorporated into the hull to improve the flow conditions and reduce the drag (Wallace et al., 1991). This team performed several water tunnel tests to determine optimal geometry for the riblets on the hull. Their efforts and hard work brought them to the winners circle.

1.3 Research Objectives

The project had three main objectives. The first included the velocity profiles and the flow field at various streamwise location on the ribletted plate under three specified pressure gradients. This objective determined the type (laminar, transitional, or turbulent) of flow field and the turbulence characteristics. The second objective centered around the relationship of the measured flow parameters (velocity, turbulence, skewness, flatness, vortex formation and Reynold's stress). This objective also included modeling the boundary layer above the flat, ribletted plate. The third objective involved calculating values of the local skin friction and comparing these with predicted flat plate values. To accomplish these objectives, two intermediate tasks were necessary. The first of these included assembly and configuration of the Boundary Layer Research Facility such that both zero pressure gradient and adverse pressure gradient flows over a flat plate were possible. The second required testing and equipment adjusting to ensure the apparatus provided accurate test data.

The previous researcher (Dement, 1996) accomplished much of the assembly of the apparatus. Some of the equipment only needed to be aligned and readjusted. The test assembly used much of the apparatus from the Rothenflue (1996) investigation, as well. One major difference Dement (1996) incorporated into the wind tunnel was the ability to adjust the pressure gradient. To be able to adjust the pressure gradient in the wind tunnel, the AFIT fabrication shop built a new test section. The test section design allowed for the adjustment of side walls to adjust so specified pressure gradient flows were possible. This investigator added another significant difference, the addition of optic glass plates placed over laser slots in the side wall. These plates eliminated any turbulence introduced from flow entering this slot from the laboratory. Without the optic glass enclosing the sides of the test section, achieving a specific pressure gradient would be very difficult.

Several changes were made to the data acquisition system based on recommendations from previous experiments. Among these included a newer traverse system for the Laser Doppler Anemometry system, a two watt Argon Ion laser, and a more capable controlling computer. Air flow to the test section remained the same as previous experiments.

To ensure reliable and accurate test data, the first objective included reproducing the Blasius boundary layer solution for a smooth, flat plate. This known analytical solution provided a means to validate proper orientation of the equipment, software, data reduction, and experimenter in performing this investigation.

The primary investigation centered around the flow characteristics over the ribletted plate. After establishing a zero pressure gradient flow over a smooth, flat plate, the ribletted plate investigation began. The flow study over the plate included an in depth analysis of the aerodynamic characteristics. The zero pressure gradient case provided boundary layer profiles and drag characteristics comparable to previous experiments under similar conditions. Investigation of the adverse pressure gradient was performed for two different conditions in the wind tunnel. These corresponded to the Falkner-Skan pressure gradient parameters (β) of -0.1 and -0.18 (White, 1991). To meet the objectives, three measurement profiles were employed. These profiles were freestream velocity measurements at various locations in the streamwise direction, boundary layer profiles starting at a riblet peak, and a grid profile at data points between the riblet peaks. These measurement profiles provided the data to identify the velocity structures and characteristics for a ribletted plate in an adverse pressure gradient.

The three objectives for this investigation were met.

1.4 Thesis Overview

The author provides the investigation results in several sections. Chapter 2 contains the discussion of the theory applied to meet the objectives. The theory and governing principles include a discussion of a flat plate, laminar boundary layer, expected flow over a ribletted plate for both zero pressure gradient and adverse pressure gradient, and the Laser Doppler Anemometry (LDA) system principles. Chapter 3 is the description of the experimental apparatus used while the procedures followed to obtain the data needed to satisfy the objectives is contained in Chapter 4. The experimental data and a discussion of these results was placed in Chapter 5. The last section (Chapter 6) concludes with significant findings and recommendations for further research on this subject.

2. Governing Principles

2.1 Flat Plate Flow

Measuring flat plate flow in a zero pressure gradient provided a tool to adjust the equipment and wind tunnel. By recreating the known analytical solution for Blasius flow, several aspects of this investigation were validated. These included the wind tunnel, wind tunnel operation, Laser Doppler Anemometry operation, laser incident angles with respect to the test section, and coordinate transformations. Data measurements also allowed determination of turbulence levels in the wind tunnel. The freestream turbulence levels provided information on flow characteristics of the wind tunnel.

The governing principles for the boundary layer over a flat plate in a zero pressure gradient flow were defined by Blasius using non-dimensional variables and the equations of motion for a two

dimensional flow. The steady, two-dimensional boundary layer equations can be reduced to an ordinary differential equation which can be numerically integrated and solved using a similarity variable. The final boundary layer equation for Blasius flow is (White, 1991)

$$f''' + ff'' = 0 \tag{2-1}$$

The similarity variable, η, and velocity components are defined by (White, 1991):

$$\eta = y\sqrt{\frac{U}{2\nu x}} \tag{2-2}$$

$$u = Uf' \tag{2-3}$$

$$v = \sqrt{\frac{\nu U}{2x}}\left(\eta f' - f\right) \tag{2-4}$$

To determine turbulence levels in the flow, the weighted squared sums of each of the velocity components variations was used (White, 1991). This relationship provided a relative turbulence intensity at a given point in the flow averaged over time.

$$T = \frac{1}{U}\sqrt{\frac{\overline{u'}^2 + \overline{v'}^2 + \overline{w'}^2}{3}} \tag{2-5}$$

Turbulence levels defined the flow state as either laminar, transitional or turbulent. This definition was also used for both the smooth plate as well as the ribletted plate.

For comparison, the Falkner-Skan Wedge flow relationship was used for the adverse pressure gradient conditions on the ribletted plate. This relationship for a flat plate was defined as (White, 1991):

$$f''' + ff'' + \beta\left(1 - f'^2\right) = 0 \tag{2-6}$$

The freestream flow followed a power law distribution ($U(x) = Kx^m$). The parameters for the velocity distribution (K and m) also define the similarity variable (η) and the pressure gradient variable (β). These relationships are (White, 1991):

$$\eta = y\sqrt{\frac{(m+1)}{2}\frac{U(x)}{vx}} \tag{2-7}$$

$$\beta = \frac{2m}{m+1} \tag{2-8}$$

2.2 Ribletted Plate Flow

Riblets in the plate run longitudinal to the plate parallel to the nominal direction of the air flow. Earlier testing investigated various ribletted shapes (Bechert et al., 1989) with V-groove riblets showing some of the best performance for reducing drag. V-groove or triangular shaped riblets have been investigated for various reasons. The primary purpose for employing riblets was to reduce skin friction and delay separation of the flow. Research in turbulent boundary layers has shown a reduction in skin friction over a flat plate by six to eight percent for V-groove shaped riblets (Walsh, 1990). Due to the increased drag in turbulent flows, much of the research has centered around turbulent boundary layer problems. Some research into laminar flows have proved little benefit. Rothenflue (1996) investigated some laminar flow properties but was more interested in the effect of the riblets on Görtler vortices.

Previous testing and research has provided a basis for comparison. The results of the tests performed by Rothenflue (1996) and Dement (1996) suggested the presence of a sustained vortex velocity structure between the riblets. Preliminary testing showed the flow characteristics at 80 mm from the leading edge would be laminar, at 200 mm, transitional, and at 400 mm, turbulent under a zero pressure gradient. The major influence riblets have on laminar boundary layers is the

acceleration of the transition region (Walsh, 1990). For this reason, several streamwise locations were explored to include laminar, transitional and turbulent flow field characteristics.

Riblets have been the subject of many studies since the 1970's. These studies, both experimental and numerical have explored many aspects of the turbulent statistics in trying to discover the mechanisms responsible for the skin friction benefits. These areas were identified in Choi et al. (1993) as: an increase in the viscous sublayer of the boundary layer causing a shift in the log-law velocity profile, a displaced origin for the wall, reduced turbulence and Reynolds shear stresses, a decrease in momentum thickness, limited changes of the mean velocity and turbulence in the inner regions of the boundary layer, among others. Most of the research performed to date involved zero pressure gradient conditions.

2.2.1 Velocity Profiles

The turbulent and laminar boundary layer profiles for a smooth plate offered some means of comparison for similar conditions over the ribletted plate. For the specified flow conditions (zero pressure gradient, adverse pressure gradient), the riblet plate profiles were compared to the Falkner-Skan solution for laminar and transitional flow fields while turbulent and transitional flow fields were compared to the Law of the Wall and Law of the Wake profiles.

The velocity profiles were investigated from the peaks of the riblets. Since the velocity profiles were being investigated for the profile of the boundary layer above the plate, the profile above the riblet peaks was considered more representative. Choi et al. (1993) showed the spanwise changes in the mean streamwise velocity distribution occurred only near the riblets. There will be little variation to the boundary layer profile shape above the plate when measured above the riblet peak or above the valley. The differences in the boundary layer velocity near the riblets was investigated using a grid profile in the riblet valley.

The pressure gradient for the flow field was characterized by the Falkner-Skan gradient characteristic, β, as discussed earlier. The Falkner-Skan profile and characteristics were used for comparison to the laminar locations on the ribletted plate. The Clauser equilibrium parameter (β_c) was calculated for all locations along the plate as well. For equilibrium turbulent flows (constant β_c), the velocity profile follows the power law (White, 1991). The Clauser equilibrium parameter is defined as (White, 1991):

$$\beta_c = \frac{\delta^*}{\tau_w}\frac{dp_e}{dx} \tag{2-9}$$

The relationship for the displacement thickness (δ^*) and calculated wall shear stress resulted from the measured velocity profiles. The displacement thickness was calculated as (Nieuwstadt et al., 1993):

$$\delta^* = \int_0^\infty \left(1 - \frac{u}{U}\right) dy \tag{2-10}$$

The local shear stress at the wall (τ_w) was estimated using a linear profile for the change in the velocity at the wall for each boundary layer profile.

$$\tau_w = \mu\left(\frac{du}{dy}\right)_w \tag{2-11}$$

The pressure gradient was calculated using Bernoulli's relationship for an incompressible flow and the change in velocity as calculated from the power law variables (White, 1991).

$$\frac{dp}{dx} \approx -\rho U \frac{dU}{dx} \tag{2-12}$$

Momentum thickness and the shape factor provided further boundary layer characterizations. These relationships include (Niewstadt et. al, 1993):

$$\theta = \int_0^{\infty} \frac{u}{U}\left(1 - \frac{u}{U}\right) dy \tag{2-13}$$

$$H = \frac{\delta^*}{\theta} \tag{2-14}$$

$$\mathrm{Re}_\theta = \frac{\theta U_m}{\nu} \tag{2-15}$$

The flow measurements taken in the laminar flow regimes were plotted using the Falkner-Skan similarity variable. The small amount of riblet research under laminar flow conditions provided very little data for this investigation to compare. Experiments in pipe flow and with direct numerical simulations of the flow show very little benefit to ribletted surfaces under laminar conditions. The major effort for this flow condition was to investigate the effects of the pressure gradient and to determine if there were any drag benefits.

Several models were used to compare to the measured data for the turbulent and transitional flow fields. These models take into account different aspects of the velocity profiles. The inner and outer profiles accounted for the logarithmic region of the turbulent boundary layer. The inner profile addressed the flow closer to the wall (Law of the Wall), while the outer profile suggested by Clauser addressed the wake at the edge of the boundary layer (Law of the Wake). The velocity profiles were also plotted using edge variables for comparison.

Law of the Wall. Under a zero pressure gradient, flow measurements were made in a transitional zone and turbulent zone of the boundary layer. No analytical or empirical models of the transitional boundary layer have proved universally acceptable (White, 1991). This region of the boundary layer has both areas of turbulent and laminar flow. The Law of the Wall provided a means to predict velocity profile behavior in the viscous sublayer as well as the log-law region of fully turbulent flow.

This boundary layer profile can be fitted to the viscous sublayer of the transitional and turbulent flow fields.

The turbulent velocity profiles over a flat plate follow a logarithmic region for a significant portion of the thickness. Near the wall, the flow deviates from this profile somewhat. The Spalding (White, 1991) solution provided an empirical equation for the boundary layer over a flat plate.

$$y^+ = u^+ + e^{-KB}\left[e^{Ku^+} - 1 - Ku^+ - \frac{(Ku^+)^2}{2} - \frac{(Ku^+)^3}{6}\right] \tag{2-16}$$

The relationship shows a good fit to the inner portion of the boundary layer. This region corresponds to approximately $35 \leq y^+ \leq 350$. Values for K and B are considered empirical constants. For low-Reynolds number flows, typical values are K = 0.41 and B = 5.0. To fit this equation to the viscous sublayer of the transitional regime, the value for B was varied. Equation 2-16 is expressed in the inner variables as defined by:

$$y^+ = \frac{yu_\tau}{\nu} \tag{2-17}$$

$$u^+ = \frac{\bar{u}}{u_\tau} \tag{2-18}$$

$$u_\tau = \left(\frac{\tau_w}{\rho}\right)^{1/2} \tag{2-19}$$

Law of the Wake. Walsh (1990) presented Cole's approach to predict turbulent boundary layer velocity profiles closer to the edge of the boundary layer. This relationship is expressed in equation 2-20 (Walsh, 1990). Cole's wake parameter (Π) is directly related to the pressure gradient in the flow. For a zero pressure gradient case, Equation 2-20 and Equation 2-16 converge in the upper region of the boundary layer. As the adverse pressure gradient increased, this relationship takes into

account the wake found on the edge of the boundary layer. The wall roughness factor (F) introduced by Gaudet (Walsh, 1990) represented a surface roughness and was tested on flat plates for various sand grain roughness (Walsh, 1990). The sign for F in Equation 2-20 was changed from the orientation defined by Walsh (1990) to correspond to the definition in Choi et al. (1993). The wall roughness parameter was determined by fitting the experimental data with the Law of the Wake (Equation 2-20). Choi et al. (1993) has implied positive values of F correspond to drag-reducing cases while negative values correlate to drag-increasing for Equation 2-20.

$$u^+ \approx \frac{1}{\mathrm{K}}\ln(y^+) + B + \frac{2\Pi}{\mathrm{K}}\sin^2\left(\frac{\pi}{2}\frac{y}{\delta}\right) + F \qquad (2\text{-}20)$$

The ribletted plate velocity profiles were compared to the expected flat plate velocity profiles for the flow field conditions. These profiles were also compared to similar riblet research to better validate these results. Of significant importance in comparing this data included determining a virtual origin for the boundary layer. Several methods have been used to determine this critical parameter.

2.2.2 Virtual Origin

For laminar, transitional and turbulent velocity profiles, the riblets caused some confusion as to the location of the origin. For this reason, a virtual origin was employed. The virtual origin is the location of an imaginary smooth flat plate which has the same drag for the ribletted plate. The velocity profile above the plate will match using the virtual origin. Choi et al. (1989) identified four methods used to locate the virtual origin. These include: (i) using a modified Clauser's method as described by Houshmand et al.(1983), (ii) Houshmand et al. (1983) also suggested using a measured linear velocity profile inside the viscous sublayer, (iii) measurements of the velocity defect profile above the inner region (Choi, 1989), and (iv) by assuming a linear velocity region exists in the viscous sublayer, using conformal mapping (Bechert & Bertenwerfer, 1989).

Since the logarithmic region was expected to be somewhat narrow, methods (i) and (iii) would be somewhat inaccurate. Nevertheless, fitting the logarithmic profile to the tested data provided one means to compare other methods of determining the origin. Method (ii) relied on the baseline of the mean velocity and will not be useful in determining the virtual origin.

Choi et al. (1989) suggested Bechert & Bertenwerfer's (1989) method (iv) provided the best results. The linear approximation of the boundary layer in the viscous sublayer region of the profile proved to be the most useful. The velocity profile was shifted in the normal direction until a linear projection of the profile near the surface intersected the origin.

Another important flow characteristic to be considered should be the turbulence intensity structure. The maximum turbulence intensity of a flat plate occurs at $y^+ = 13$ (Choi et. al., 1993). The definition of the inner variable can then be used to determine an equation for the virtual origin. Choi et. al. (1993) states this equation as:

$$y_o = y_m - \frac{13\nu}{u_\tau} \tag{2-21}$$

These two methods were compared to provide support for one another and to determine any possible position error in the data.

2.2.3 Turbulence and Reynolds stresses

The turbulence equation given earlier (Equation 2-5) was used to calculate the relative turbulence at a point in the flow. This equation takes into account variations in all three velocity components. These turbulence levels provided a means to initially determine the flow state. Using peak turbulence values for a given boundary layer profile, those below 3% turbulent were considered laminar (Rothenflue, 1996). Transitional flow fields contain areas of laminar flow with locally embedded turbulent flow. For a fully turbulent boundary layer profile, the flow needed to be

at least 9% turbulent. For this reason, the lower limit for turbulent flow was a peak value of 9% in the boundary layer.

Turbulence levels in the valley have shown to be lower near the center of the valley and increasing in the spanwise direction toward the peak at a fixed distance from the surface of the riblet (Wallace et al., 1991). Choi et al. (1993) showed variations for turbulence in the spanwise direction in regions where there were no spanwise variations of the streamwise velocity. This suggests the cross flow was more sensitive to the riblets than the streamwise flow. A reduction in the turbulence intensity would suggest a drag reduction (Choi et al, 1993). Under an adverse pressure gradient, turbulence intensities would be expected to increase at the same streamwise location on the plate. For this investigation, a comparison of the turbulence intensities was performed for the various pressure gradient conditions.

Using the LDA system, measurements of the Reynold's stresses were possible. These stresses provided another means to explore the turbulence and drag reductions in a ribletted flow. Changes in the Reynold's stresses suggested a change in the average production of turbulent kinetic energy (Djenidi et. al. 1996). These changes affect the average energy production and dissipation rates. For the drag reducing case, Walsh (1980) showed a maximum reduction in the Reynold's stress of 16% below flat plate values. For drag increasing configurations, the Reynold's stresses were unaffected above the valley while increasing above the riblet peaks (Choi et al., 1993). As the riblet spacing increases in wall units, the Reynold's stresses increase but the reduced turbulence intensities remain (Choi et al., 1993).

2.2.4 Skin Friction Drag

One primary interest in researching the flow characteristics of ribletted surfaces includes their ability to reduce skin friction drag in turbulent boundary layers. This research looks at changes of

the skin friction as a result of an applied pressure gradient. Several methods have been employed to calculate drag and skin friction characteristics of boundary layers.

For a zero pressure gradient, the skin friction relationship reduces to a simple expression involving the momentum thickness gradient. To calculate an average, local skin friction coefficient, Walsh (1990) suggested using:

$$C_f = 2\frac{d\theta}{dx} \tag{2-22}$$

This momentum balance method has proved to vary depending on the experiment (Nieuwstadt et. al., 1993). For this reason, this method is not used in this investigation. Calculated values were compared to the expected theoretical measurements from flat plate approximations, though (White, 1991):

$$C_{f,laminar} = \frac{0.664}{\sqrt{\mathrm{Re}_x}} \tag{2-23}$$

$$C_{f,turbulent} = \frac{0.027}{\mathrm{Re}_x^{1/7}} \tag{2-24}$$

Under an adverse pressure gradient, two relationships were used to compare calculated values for the skin friction coefficient. Laminar flow conditions used the Reynold's analogy for Falkner-Skan flow to give (White, 1991):

$$C_f(x) = f_o'' \sqrt{\frac{2(1+m)\nu}{Ux}} \tag{2-25}$$

The local skin friction relationship for turbulent flow can be approximated by the Karman Integral Relationship (White, 1991). This relationship employed the shape factor and Reynold's number based on momentum thickness. These values were calculated from the measured velocity profiles.

$$C_f = \frac{0.3e^{-1.33H}}{(\log_{10} \mathrm{Re}_\theta)^{1.74+0.31H}} \tag{2-26}$$

The investigation calculated the skin friction coefficient using a linear approximation of the velocity profile near the wall. This method employed the slope of the boundary layer profile in the linear viscous sublayer. This slope then was used to calculate τ_w using Equation 2-11. The skin friction coefficient could then be calculated from Equation 2-26 (White, 1991):

$$C_f = \frac{2\tau_w}{\rho U^2} \tag{2-27}$$

By using a linear approximation for the velocity measurements near the surface between two peaks at the various grid locations and integrating over this surface, a value for the skin friction could be calculated more accurately using Equation 2-28. This relationship provides a local, average shear stress at a given streamwise location. The integration was carried out numerically between two peaks and normalized by the wetted surface area for this interval.

$$\tau_{w_{ave}} = \frac{\int \tau_w dA}{\int dA} \tag{2-28}$$

The average shear stress from Equation 2-28 was then used in Equation 2-27 to calculate local values for the skin friction coefficient. The skin friction coefficient was then scaled to the planform area of the ribletted plate to be able to compare to smooth plate values. The average shear stress method reduced any variability introduced by measurement or position error.

2.2.5 Velocity Structures

Velocity structures investigated by this research included searching for stable formation of vortex pairs between the riblet peaks. These vortices have been observed as two counter-rotating vortices which vary in strength with respect to riblet spacing, s^+ (Suzuki and Kasagi,1994). Suzuki

and Kasagi (1994) also suggested a higher s^+ caused the centers of the vortices to move toward the peaks. Figure 2-1 shows the predicted vortex structures for the y-z plane

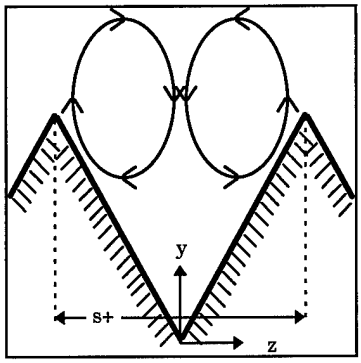

Figure 2-1: Vortices in riblet valley

Suzuki and Kasagi (1994) also suggested at lower s^+, the y-z plane velocity components tended to be lower in strength when compared to the freestream velocity. For closer spacing, the vortex motion has a much lower strength and tends to be more random. These researchers suggested this vector field is a result of averaged streamwise vortices appearing randomly in both time and space near the riblets. With closer spacing of the riblets, the strength of the vortices would be much lower and appear to be a random motion when ensemble averaged. For highly random motion, the ensemble averaging would produce a vector result approaching zero magnitude as more samples are taken.

Rothenflue and King (1995) suggested the rotating vortices originated in the transitional region of the flow field. They stated the vortex vector magnitudes (v-w velocity vector) can be as high as 4% of the freestream velocity values once fully developed in the flow. Suzuki and Kasagi (1994) showed the strength of the vortex velocity could reach 0.8% of the freestream under their testing conditions. Rothenflue (1995) also suggested these velocity structures remain apparent for the length of the turbulent flow field.

The DNS research of Choi et al. (1993) identified these secondary velocity structures as well. This data showed the counter rotating vortices relative strength to be less than 1% of the freestream velocity. The relative strength and spacing of the vortices found by the DNS data was a function of the riblet geometry. For the drag reducing geometry ($s^+ \approx 20$), the strength was much lower (0.2% of freestream velocity) (Choi et al., 1993). This study also noted in laminar flow, the secondary velocity structures were not sustained.

2.2.6 Flatness and Skewness

The flatness and skewness (third and fourth moments of velocity) provided an indication of the variations of the velocity components. High values of these factors would indicate large amplitude velocity fluctuations (Park and Wallace, 1991). Low values indicate just the opposite. Large values of skewness correspond to a local velocity generally below the mean value with occasional large excursion to values above the mean (Walsh, 1990). Flatness factor provides an indication of the frequency of the large excursion of the velocity above the mean. Larger flatness factors indicate a shorter period between large excursions from the mean velocity value (Walsh, 1990). Near the wall, skewness and flatness values would be expected to be larger than in the rest of the flow.

Park and Wallace (1994) further investigated these moments using hot wire measurements. They discovered the maximum flatness and skewness occurred just above the midpoint of the riblet near $y^+ = 10$ from the valley ($s^+ \approx 30$). These maximum locations along with low values of turbulence in these areas suggested large-amplitude, positive streamwise fluctuations occasionally reach to about the mid-plane of the riblet valleys but not much further into the valley. Walsh (1990) found no change from flat plate data for drag reducing geometry for these statistics of the flow. For drag augmenting, the skewness and flatness zero points tend to be further away from the plate in the normal direction (Walsh, 1990).

3. Instrumentation and Test Equipment

3.1 Wind Tunnel

The wind tunnel designed for the Boundary Layer Research Facility provided the primary testing equipment. The tunnel design is discussed at length by Rothenflue (1996). The tunnel consisted of the stilling chamber and test section while being supplied by a common air supply for the laboratories. The primary purpose for the Boundary Layer Research Facility included the investigation of various boundary layer flow properties for different configurations and surface conditions. The tunnel has provided between one half and one kilogram per second mass flow rates for previous testing with velocities ranging from 3 to 15 m/s (largely dependent on the test section being used). For these velocities and mass flow conditions, maximum Reynold's numbers in the tunnel ranged from 200,000 to 993,000. The current test section is one meter in length. Testing conditions for this experiment had Reynold's numbers between 25,000 and 155,000.

3.1.1 Air Supply

The purpose of the air supply was to provide a steady mass flow to the test section. Two Atlas air compressors provided the common air supply at a nominal 690 kPa. The compressors were configured to operate continuously when the pressure dropped below 634 kPa and continued until pressure reached 827 kPa. These compressors along with the necessary pressure tanks, distribution lines and system controls are located in the basement of Building 640 of AFIT.

With the compressors providing flow based on pressure level, additional flow control hardware was necessary to maintain a steady mass flow provided to the wind tunnel. This plumbing, located in the Boundary Layer Research Facility, consisted of a flow regulator, air supply filter, external vent

valve and purge valve. This air supply and flow control hardware were also attached to the Cascade Research Facility in the same laboratory.

The filter prevents rust, water, and compressor lubricants from contaminating the air supplied to the wind tunnel. A clogged filter caused significant pressure fluctuations in previous experimentation and prevented meaningful data from being acquired. Use of the purge valve aided in this task by allowing excess water, oil and other particles accumulating in the lines and water separator to be vented to the outside before running the air flow through the filters.

The flow regulator made it easier to provide a steady flow to the wind tunnel. This valve was set with a screw on the regulator's pilot valve. The upstream supply pressure controlled the valve orifice with feedback from the downstream back pressure. The flow regulator was a pressure regulator and therefore a fairly constant upstream pressure to the valve was necessary. The external vent valve provided a means to establish this constant upstream pressure.

The external vent valve allowed excess mass flow from the compressors to be bled off instead of letting the compressors build up pressure. A flow condition was initially set in the wind tunnel by the flow regulator. The external vent valve was then used to establish a constant pressure level at which the compressors could maintain without shutting off or causing pressure fluctuations. A circuit diagram of the air supply is provided in Figure 3-1. The figure also shows the connection and shut off valve for the Cascade Research Facility.

The differences from this test investigation as compared with previous Boundary Layer Research Facility configurations included some plumbing differences. Rothenflue (1996) used some of the plumbing currently being used by the Cascade Research Facility. This allowed him the means to increase the mass flow rate to nearly one kilogram per second. Current configuration had maximum capabilities around 0.5 kg/s. Rothenflue also used this section of plumbing to inject the seeding

material. For this reason, the wind tunnel was modified to incorporate an alternate method to seed the flow. Also, the alternate inlet plumbing required a diffuser cone to slow the flow before entering the stilling chamber. The diffuser cone and stilling chamber slowed and straightened the flow before it entered the test section.

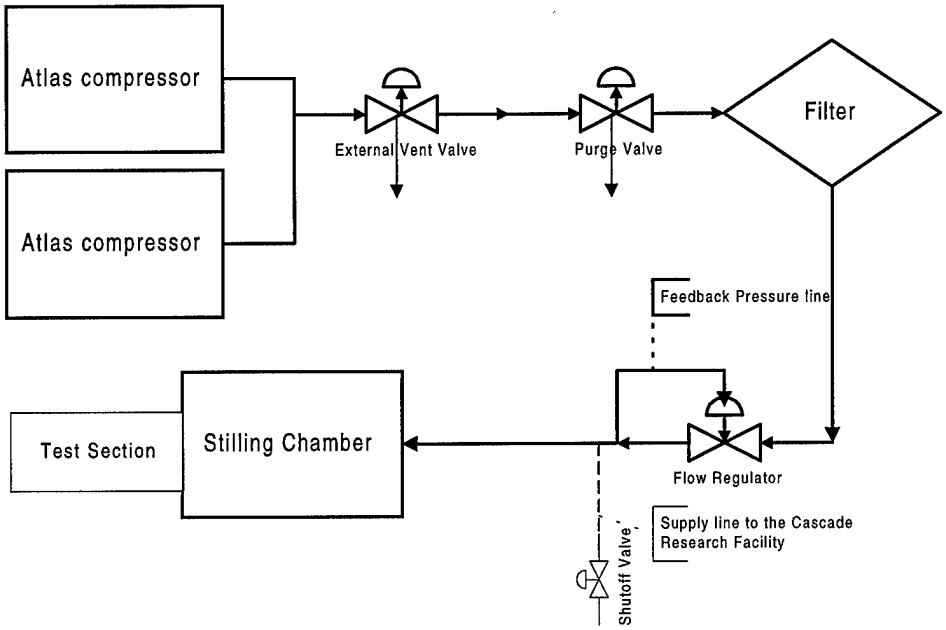

Figure 3-1: Circuit diagram of the air supply system

3.1.2 Stilling Chamber.

The stilling chamber was designed according to generally accepted principles as discussed in Rothenflue (1996). The primary purpose of the stilling chamber was to straighten the flow before entering the test section and to evenly distribute the seeding material needed for the Laser Doppler Anemometry (LDA) measurements. The stilling chamber was also modified to inject the seeding material. A pressurized chamber was attached to the top of the stilling chamber which housed a TSI 6-jet atomizer and Roscoe Fog Generator which produced the seeding material. The pressure in the chamber forced the seeding fog into the stilling chamber through passages in the top of the chamber.

The atomizer was operated by pressurized air provided by the shop air system. In order to pressurize the fog chamber, a separate pressure line from the shop air entered the chamber. This line ensured the seed fog entered the stilling chamber. The Roscoe Fog Generator produced much larger quantities of seeding material. The higher seeding material mass flow made it possible to take data measurements at much higher rates. This seeding method was introduced to make final measurements in the flow field.

The air supply entered the stilling chamber through a diffuser cone. This cone was fabricated for this test configuration. The diffuser used for Rothenflue's (1996) experiment was longer and expanded the flow slower. Although the cone was designed to prevent separation of the flow, turbulence in the freestream suggested it might be the cause of the higher levels of turbulence over those measured by Rothenflue.

3.1.3 Test Section

The test section was specifically fabricated for boundary layer investigations over a flat plate (smooth and ribletted) and to be able to investigate affects of adverse pressure gradient on the boundary layers. The test section used the same entrance dimensions and attachment points employed by Rothenflue (1996). Adjustments to accomplish specified pressure gradients were not possible with the Rothenflue test section.. The new test section consisted of a rigid top and bottom plate, flexible side walls, and removable test plates.

The side walls were hinged to the aluminum entrance plate from the stilling chamber. The inlet area was 16 cm by 40 cm. The walls consisted of 1/8 inch plexiglass for flexibility with L-shaped brackets to hold the walls in place. Hinge clamps were used on the side wall brackets for ease of adjustment. These clamps made it possible to easily readjust the positions of the walls to specific pressure gradients in the wind tunnel. The wall nearest the laser had a slot cut into it to allow the

laser an unobstructed path to the measurement location. The slot was covered with laser quality optical glass. The glass enclosed the test section without interfering with the laser system's ability to take accurate measurements. The side walls are shown in Figure 3-2.

The top and bottom rigid plates primary purpose was to hold the test plate, eliminate any spanwise flow and to attach the side walls. They were positioned on a stand and held in place by four threaded steel rods. These rods were positioned to ensure the plates were at a constant distance apart for the entire length of the test section. Slots were cut in the top and bottom plates to slide the test specimens into and out of the test section. The test section configuration can be seen in Figure 3-2.

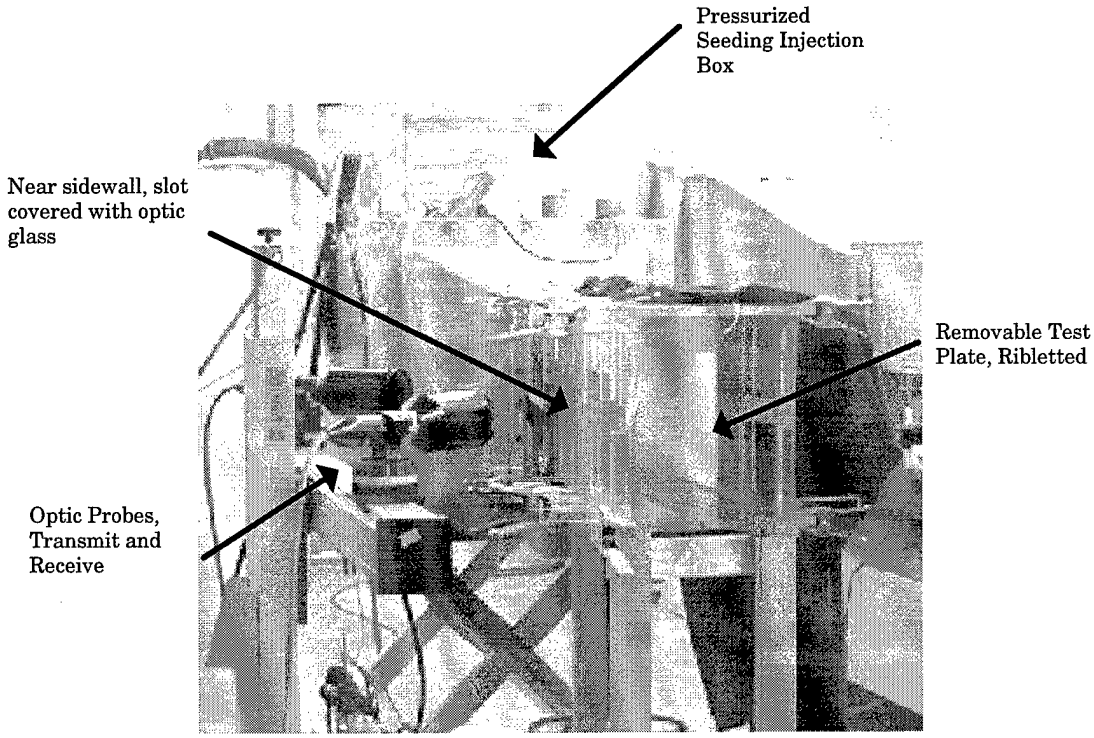

Figure 3-2: Wind tunnel test section and apparatus

There were two test plates used for this investigation, a smooth, flat plate and a ribletted, flat plate. These plates were one meter long and 41 cm wide. They were fabricated with a 30° wedge to give a sharp leading edge. The ribletted plate had V-shaped groves cut into the plate along the

length of one meter. The riblets covered a 25.4 cm section in the middle of the plate. The peaks of the V-shaped grooves were 3±0.1 mm apart and 2.6±0.1 mm tall. The plate dimensions can be seen in Figure 3-3.

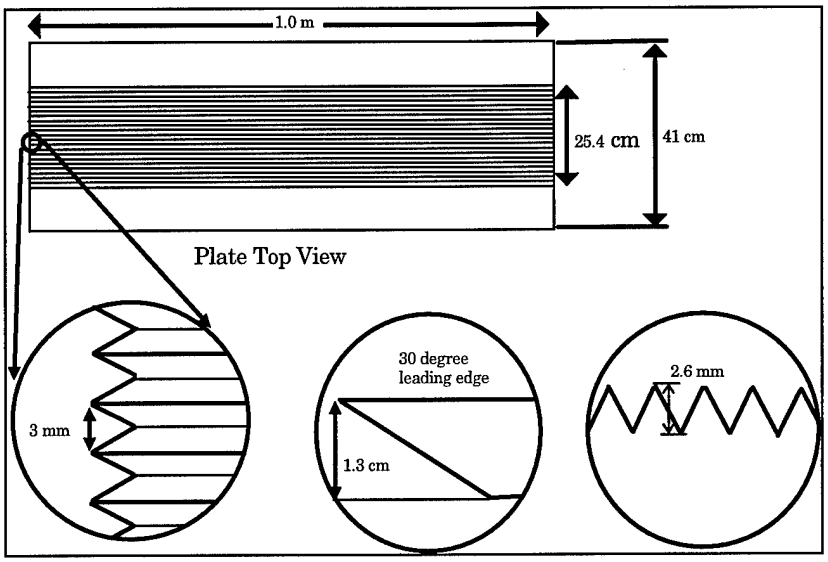

Figure 3-3: Riblet plate geometry

3.2 Laser Doppler Anemometry Instrumentation

The LDA system consisted of several major components. Among these include the laser, laser transmission system, measurement probes, photo-multiplier tubes, Burst Spectrum Analyzers (BSA), acquisition computer, Burstware® Software and Traverse System. Each of these components provided specific vital functions for the acquisition of the test data.

3.2.1 Laser

Two lasers were used during the course of this investigation. For the flat plate data measurements, a 300 mW Argon Ion laser was used. This portion of the investigation was primarily to adjust the tunnel and become familiar with the test equipment. The 300 mW laser provided sufficient power to take data readings, but the rate was somewhat restricted. After the last research effort using this laser, it was sent to the manufacturer for cleaning and inspection. The manufacturer determined a new laser tube was necessary and the mirrors needed cleaning. Power

output measured over 300 mW at a wavelength of 488 nm. This allowed data rates near 1000 Hz in the freestream flow with the proper seeding rates.

The introduction of the second laser, a two Watt Argon Ion laser, allowed much higher data rates and more reliable data. This laser required a new power source and continuous water supply for cooling. The laser also offered easier methods to optimize and adjust the laser output. These adjustments made it possible to optimize the laser for the lower power wavelength, 476.5 nm. This new laser was able to provide up to five watts of power under optimal conditions and allowed for data rates in excess of 6000 Hz. The limiting factor appeared to be the seeding in the air flow. The Roscoe Fog Generator allowed these higher data rates to benefit the investigation.

3.2.2 Laser Transmission System

The transmission system consisted of the Bragg cell to split the beams, six manipulators to direct the laser beams, and the routing mirrors, prisms and fiber cables. The Bragg cell housed in the Transmitter (Figure 3-4) separated the laser beam into two beams and shifted one with the use of a 40 MHz signal from the Burst Spectrum Analyzers. This frequency shift was necessary to create the fringe patterns for the LDA system to measure the velocity vectors in the flow. The Bragg cell had an adjustment to allow the power level of the beams to be equalized during adjustment. The Transmitter housing had to be removed for access to this adjustment. A beam level adjustment on the Bragg cell was also available through a screw hole on the back side of the housing. This adjustment allowed some level of power adjustments between the beam pair as well. Prisms in the Transmitter then split the two beams into the three pairs of beams at specific nominal wavelengths: green, 514.5 nm; blue, 488.0 nm; and violet, 476.5 nm.

The mirror system then directs the beams up through the manipulators. The manipulators have four adjustments which position a glass tube. The glass tube directs the laser beam into the optic

fiber. The fiber plug was attached to the top of the manipulator. The fiber plug contained an adjustment ring to focus the laser beam into the fiber cable. These five adjustments were the primary means to optimize and increase the laser output to the measurement probes. Figure 3-4 illustrates the Transmitter and the location of these components.

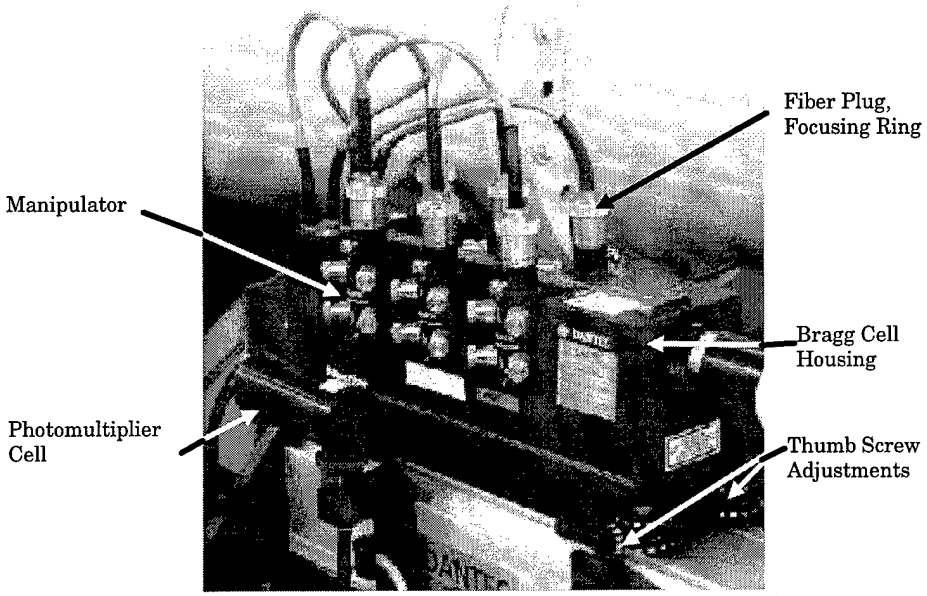

Figure 3-4: Laser Doppler Anemometry transmitter

3.2.3 Measurement Probes

The fiber cables transmit the beams to the measurement probes. For this experiment, the probes were fitted with a beam expander with a 600 mm focal length. The expander increased the distance between each of the pairs of beams to 75 mm. The probes direct the beam pairs to intersect at the focal length. For the 3-D LDA system, two probes were necessary, a 1-D probe and a 2-D probe. The 1-D probe was attached to the traverse system with a base having three degrees of freedom; rotation, tilt, and translation. This probe transmitted the violet (476.5 nm) laser beams. The 2-D probe transmitted the green (514.5 nm) and blue (488.0 nm) laser beams. Each probe captured the Doppler burst from the measurement volume and focused them into a fiber cable routed to photo-multiplier tubes.

3.2.4 Photo-Multiplier Tubes

For three dimensional measurements, three photo-multiplier (PM) tubes were necessary. The off-axis configuration directed the return Doppler signal from the 1-D probe through a color separator and then each beam to a PM tube. The return Doppler signal from the 2-D probe went through a violet (476.5 nm) filter before entering the PM tube. The PM tubes converted the Doppler bursts into electrical signals and directed them to the Burst Spectrum Analyzers (BSA) for conversion to velocity data.

3.2.5 Burst Spectrum Analyzers

The Burst Spectrum Analyzers (BSA) converted the electrical signal from the PM tubes into velocity data. Each signal was attached to a separate BSA. The BSA's were numbered as follows: green (514.5 nm), BSA #1; blue (488.0 nm), BSA #2; and violet (476.5 nm), BSA #3. A timing cable connected the three BSA's to allow for hardware coincidence filtering. The coincidence filtering increased the reliability of the resulting data. For the hardware coincidence, one BSA was a master enhanced model (Dantec 57N25) while the other two were enhanced slaves (Dantec 57N35). The BSA's were controlled by the Burstware® software from the acquisition computer.

3.2.6 Acquisition computer and Burstware® software

The computer controlled the LDA and traverse systems. It also provided a means to reduce and convert the raw data into meaningful velocity vectors. The software provided a means to further ensure the three BSA's provide coincident data from the same seeding particle. The software had four main function; configuration, setup and acquisition, processing and presentation. The Burstware® software performed most of the major data acquisition and reduction.

3.2.7 Traverse System

The traverse system provided a means to move the measurement volume in the test section. The Dantec traverse system allowed for three axis motion and could be programmed to follow a

specified pattern. The transmit/receive optic probes were mounted on the traverse system bench as seen in Figure 3-2. The software controlled the movement of the traverse bench.

3.3 Miscellaneous Equipment

Several other items such as the Digital Inclinometer were used in the construction of the Boundary Layer Research Facility and investigation of riblets. These items are included in the equipment list (Appendix A). Their usage is discussed in the next section.

4. Experimental Procedure

The investigation required several involved steps to accomplish the final data acquisition for the adverse pressure gradient flow over the ribletted plate. In order to take velocity readings, several main tasks were accomplished. Among these include the wind tunnel set up, optical alignment of the LDA system, establishing appropriate software acquisition parameters, achieving a specified pressure gradient condition in the wind tunnel, maintaining a steady air flow in the wind tunnel, and data reduction.

4.1 Wind Tunnel Set Up

The wind tunnel orientation in Figure 4-1 simplified data reduction and produced the most accurate results. The wind tunnel coordinate system was fixed to the test plate. The positive x-direction pointed in the streamwise direction of the air flow through the tunnel with the leading edge as $x = 0$. The positive y-direction started at the surface of the test plate and was perpendicular to the plate. For the ribletted plate, the bottom of the valley between the peaks was specified as $y = 0$. The positive z-direction was in the spanwise direction pointing toward the floor. The $z = 0$ coordinate location was arbitrary and usually corresponded with a valley on the ribletted plate. Velocity measurements were taken at several locations in the z-direction for the ribletted plate. For the flat plate, the velocity profile was constant in the spanwise direction at a given streamwise location when sufficiently clear of the boundary layer generated from the top and bottom of the test section. Also, the flow condition goal in the wind tunnel was to eliminate any spanwise flow. For these reason, no specified $z = 0$ location was necessary as long as the measurements were being taken away form the edges of the test plate. The coordinate system can be seen in Figure 4-1.

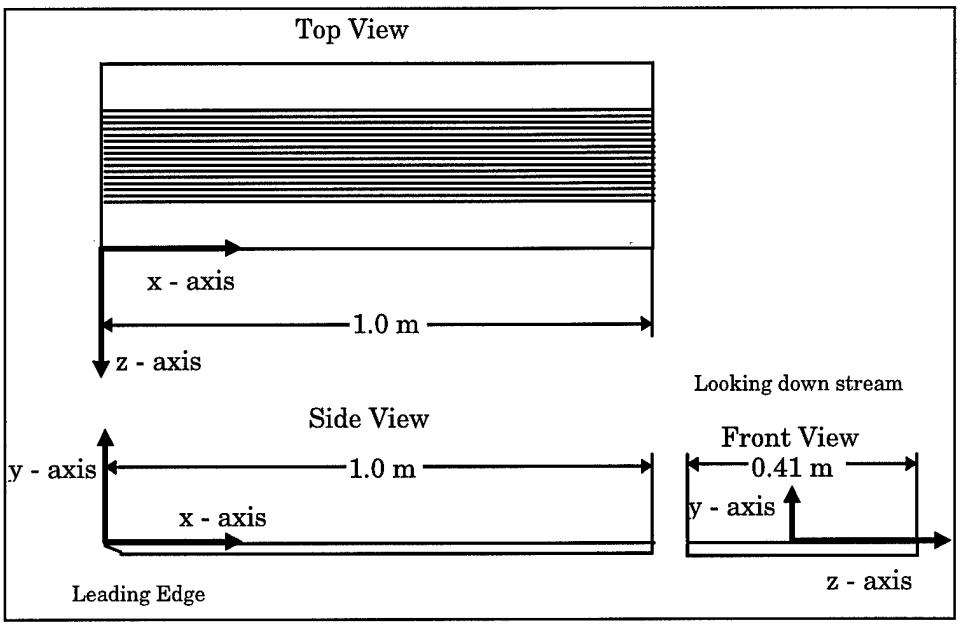

Figure 4-1: Laboratory coordinate system

The wind tunnel components were assembled as shown in Figure 3-2. This assembly employed a digital inclinometer to ensure the mounting flange and test section were level. The test section was within 0.5 deg rotation about either the x- or y-axes from level. Measuring rotations about the z-axis required a clearance gage and 3-D coordinate mapping equipment. The coordinate mapping equipment provided coordinate locations of the test plate with respect to the optics support beam. These measurements made it possible to determine the angle between the test plate and the optics support beam.

The flat plate and the ribletted plate slid into the plate slot as designed. Optic glass was placed over the slot in the side wall for the laser to enter the test section. The optic glass allowed a clear path for the lasers to enter the test section with minimal interference. This modification eliminated any turbulence introduced from an open slot observed in previous experiments. It also provided a reliable means to create a pressure gradient without introducing another flow path for the test section air flow.

The wind tunnel set up included the installation of the 6 jet TSI atomizer and Roscoe Fog Generator. The atomizer was filled with olive oil. A pressure line was attached to operate the atomizer. It was then placed into the pressure chamber on top of the stilling chamber along with the fog generator. A second pressure line to this chamber was also installed. The top of the chamber was bolted into place. The atomizer and fog generator had to be replenished several times during this investigation.

4.2 Laser Doppler Anemometry and Optical Set Up

The system consisted of a new traverse system, the laser and optics. Proper alignment and optimization was critical to data acquisition. The fringe patterns in the measurement volume depend heavily on the power level. The LDA tuning process is discussed in detail in Appendix D. The laser was attached to a mounting and adjustment bench with the power supply next to it. The mounting bench also had the transmitter mounted to it. Fiber optics cables attached to the FiberFlow® transmitter ran to the focusing probes which were attached to the traverse system.

4.2.1 Traverse System

The traverse system was installed beside the wind tunnel in the best vantage point to focus the lasers into the test section. The traverse had three degrees of freedom and was computer controlled. Movement of the traverse could be programmed in Cartesian, cylindrical, or spherical coordinates. The traverse system control box was attached to the computer through the serial port. The investigator mounted the laser focusing probes to the traverse bench. The bench was leveled with the digital inclinometer by adjusting the four feet pads of the traverse system. The 3-D coordinate mapping equipment helped place the traverse in a position parallel to the wind tunnel test plate. Maximum variations for the traverse probe bench were within $\pm 0.5°$ in rotation about the x- and y-axes and less than one degree about the z-axis.

The traverse system was used to find the surface of the test plate after a measurement volume had been established. The ammeter measuring the anode current on the front panel of BSA #1 was employed for this task. The high voltage for the PM tubes was set to 1000 V to protect the tubes from strong reflections from the surface. Since the measurements were being taken successively away from the plate, the measurement volume was then moved into the surface of the plate (visually verified). The traverse system was then moved in the positive y-direction 0.1 mm at a time until a spike was evident in the ammeter which indicated the surface of the plate (to find the peaks and valleys in the ribletted plate, movements in both the z- and y- directions were necessary). By moving the measurement volume in the same direction to be traversed for the data run, any variation in position due to gear clearances in the traverse system were eliminated. Expected position accuracy was approximately ± 0.05 mm for the traverse system.

In order to get good valid data, the traverse system was moved to 0.3 mm away from the surface to eliminate reflections which would corrupt the data. The oscilloscope used to fine tune the measurement volume was used to verify the surface indication. A high noise level was present on the scope when the surface was encountered. Once the surface was found, a traverse file with specified data point location automated the data taking at the various specified points. Location of the surface was necessary before each data acquisition.

4.2.2 Laser

The laser was attached to a mounting bench and directed into the FiberFlow® transmitter. The installation and adjustments of these components is discussed in detail in Appendix D. The primary tasks involved with the laser installation include mounting and maximizing power output. The 300 mW Argon Ion laser needed no special adapters or equipment. Incorporation of the two watt laser added a new power source and water supply requirement.

Mounting. The laser and transmitter were attached to the mounting bench approximately 15 cm apart. Care was taken to unsure the beam directed into the transmitter was parallel to the mounting bench to facilitate the transmitter alignment. The transmitter adjustments (three thumb wheels and finger screws) provided alignment capability as shown in Figure 3-4. The transmitter had internal mirrors used to align the laser into the transmitter. A shutter on the transmitter directed the incoming laser beam either to the Bragg cell or to the alignment mirror. Setting the shutter to the alignment mirror path reflected the laser back onto itself. The adjustments were made accordingly to ensure the reflected beam coincided directly with the incident beam. Once these adjustments were made, the thumbscrews were locked into place.

Power level. The 300 mW laser was recently returned to the manufacturer for repair and optimization. The laser returned with over a 300 mW power level output in the 514.5 nm wavelength. For this reason, power level adjustments on the laser were not necessary. The two watt laser provided a means to adjust the power from a control panel as well as by aligning the internal mirrors. These adjustments made it possible to center the mirrors to increase the power levels of the violet beams (476.5 nm). The control panel on the laser provided a light power meter which could be set to specific wavelengths. Using this panel to monitor laser output, the adjustments were easily made.

4.2.3 Optics

The installation of the optics system included mounting the focusing probes to the traverse system bench. Once mounted, the optics adjustments started with adjusting the manipulators and focusing the beams into the fiber optics cables. These adjustments ensured maximum power levels to the measurement volume. The power levels provided distinct and uniform fringe patterns in the

measurement volume. The measurement volume was established by adjustments to the optics probe mountings. The detailed procedure is discussed further in Appendix D.

Focusing Probes Mounting. The 2-D focusing probe was attached to the one degree of freedom mount on the traversing system. This mount allowed the probe to be rotated about an axis through the center of the mount and perpendicular with the floor. The angle from the test section (angle from the x-axis) was placed at a nominal 45°. The three degrees of freedom mount held the 1-D focusing probe. The angle from the negative x-axis was 45° to produce a 90° included angle between the laser probes. This included angle increased the accuracy of velocity measurements by reducing the size of the LDA measurement volume. This angle also provided a better vantage point for the receiving optics to detect the bursts more reliably.

The optic cables attached to the FiberFlow® transmitter by the fiber plugs (Figure 3-4). The fiber plugs were inserted into the manipulators for each respective laser pair. The three pairs (514.5 nm, 488.0 nm, and 476.5 nm) consisted of a shifted and unshifted beam. The return fiber cables directed the return signal to the color separator then into two photo-multiplier tubes from the 1-D probe and through a filter (for 476.5 nm light) to a photo-multiplier tube from the 2-D probe. The photo-multiplier was attached to each respective Burst Spectrum Analyzer (BSA).

Manipulator and Focusing Adjustments. The focusing rings and manipulator adjustments were adjusted as described in Appendix D until satisfactory power levels at the measurement volume were achieved. Information from Dantec stated the beam pairs needed to be within 20% (Wiseman, 1997) of each other. Since the violet laser beams (476.5 nm) were the weakest, they were optimized with the Bragg cell adjustments. Adjustments to the Bragg cell power and level equalized the beam output powers within this range. The other two beam pairs were balanced by defocusing the higher power beam into the fiber cable.

Initial losses through the fiber cables exceeded 75% and were even as high as 90% for one cable. Typical losses for this type of system are in the order of 50% (Wiseman, 1997). For this reason, the fiber optics needed to be returned to Dantec for cleaning and analysis. Dantec cleaned the fibers and the ends were polished reducing the power losses to near the expected 50%. Typical power levels for the three beam pairs are shown in Table 4-1. Thermal expansion and the sensitivity of the equipment required power maximization to be a daily activity.

Table 4-1: Typical power levels for laser beams

Laser Beam Wavelength (nm)	300 mWatt laser (mW)	Two Watt laser (mW)
514.5 (green)	19.0 - 21.0	120 - 150
488.0 (blue)	13.5 - 14.5	50 - 75
476.5 (violet)	3.00 - 3.80	30 - 50

4.2.4 Measurement Volume

The measurement volume was the intersection of the six individual beams from the optic probes. This intersection needed to be very precise in order to collect data using the back-scatter, off-axis technique employed for this investigation. The 2-D probe was fixed in position with the green pair (514.5 nm) in the x-y plane, putting the blue pair (488.0 nm) perpendicular to this plane. The 1-D probe emitting the violet (476.5 nm) beams was positioned in the x-y plane. The intersection of the beam pairs was initially determined visually.

To ensure the beams were intersecting, the BSA's needed to record Doppler bursts. The BSA's were turned on and the photo-multiplier tubes were powered. Seeding material was introduced to provide the flow visualization necessary. An oscilloscope attached to BSA #1 (green, 514.5 nm) monitored the Doppler output signal. As the 1-D probe position was moved through the small range, the oscilloscope displayed Doppler bursts when the beams formed a measurement volume. At the proper position of the 1-D probe, the Doppler bursts were easily distinguishable in the BSA

signal as periodic spikes. Position of the 1-D probe was further fine tuned until the Doppler signal reached an apparent maximum signal strength. The oscilloscope was then attached to BSA #3 (violet, 476.5 nm) to cross check and further optimize the measurement volume. With this being the weakest of the three pairs of lasers, it was the most critical to ensure proper alignment. Only small adjustments to the 1-D probe position were necessary at this point. The measurement volume adjustments were checked again with the output of the Burstware® software. The optimized intersection provided maximum data rates for the three BSA channels.

4.3 Software Acquisition Parameters

The software program, Burstware®, had many important parameters which controlled the entire data acquisition and reduction process. These parameters were established in the four main areas of the software; Configuration, Setup and Acquisition, Process, and Presentation. The configuration allowed the settings for a printer, the traverse system, and working directories. The setup and acquisition section of the software required the most understanding of the different parameters which controlled the LDA system. Important settings include the BSA settings, optic parameters, software filtering settings, traverse system control, and acquisition control.

Processing the data allowed for further software filtering of the data as well as coordinate transformations. These settings established specific criteria with which to reduce the velocity data from the BSA's further into meaningful wind tunnel values. The presentation ability of the software provided a good first look at the data to ensure proper shapes of the curves and low variability at each data point. Each BSA output at each data point could be viewed as well as the entire velocity profile for the data run. Since the data was often being compared with Blasius and other measured values, the data was exported to allow for graphical comparisons on the same chart. The velocity data was often exported in the optical coordinate system and converted to the wind tunnel

coordinate system. The Burstware® software provided the needed interface and control of the test equipment to perform this investigation. Each of the areas mentioned are discussed in detail in Appendix E.

4.4 Flow in the Wind Tunnel

The steady flow in the wind tunnel proved to be extremely important in the measurements made for this investigation. Added to being able to maintain steady flow, proper wind tunnel side wall adjustments were necessary to create a zero pressure gradient and the targeted adverse pressure gradients.

4.4.1 Steady flow

Maintaining steady flow in the wind tunnel was crucial to producing meaningful data. By monitoring the upstream pressure and back pressure from the wind tunnel, this task was accomplished adequately. Variations as low as 0.5 psig changes in the upstream pressure could be seen in the test data as slight changes in velocity profiles. The slight changes were apparent in the boundary layer velocity profiles over a flat plate and in the streamwise profiles taken in the freestream to determine pressure gradients. Proper adjustment of the air supply allowed the flow to reach a steady condition and could be maintained for long periods of time.

The pilot valve was opened until the back pressure gage showed approximately 28 kPa to begin the pressure flow to the wind tunnel. Adjustments to the vent valve allowed any water collected in the accumulator to drain off and helped regulate the upstream pressure. To ensure both compressors came on line and ran continuously, an overboard vent valve allowed the upstream pressure to be regulated between values of 552 kPa and 625 kPa. The wind tunnel and compressors took approximately five minutes to stabilize on a relatively steady pressure value. While the upstream pressure stabilized, the atomizer valve and pressure line valve to the seed box on top of

the stilling chamber were opened. Obtaining a specific velocity level in the wind tunnel required some adjustment to the pilot valve. By monitoring the LDA system readings in the freestream, a target velocity was achieved. Typical ranges for freestream velocities included 4.9 to 5.5 m/s for this investigation.

4.4.2 Zero Pressure Gradient

Establishing a pressure gradient was accomplished by taking freestream velocity measurements in the x-direction. Using the LDA and traverse system, a velocity profile in the streamwise direction was taken several times. For a zero pressure gradient, the freestream velocity needed to be constant for the entire test section. The near side wall (closest to the laser probes) was adjusted accordingly until a zero pressure gradient was established.

Since velocity characteristics in all three dimensions (streamwise, normal and spanwise) were important for the ribletted plate, pressure gradients in all three directions had to be addressed. The side walls were repositioned to produce a zero pressure gradient for the ribletted plate. The process of removing the influence of a spanwise pressure gradient proved to be important and was complicated by the sensitivity to slight variations in the transformation misalignment angles. The spanwise and normal velocity component values could be altered by several percent by adjusting these misalignment angles by only 0.5 degree. For this reason, being able to determine the transformation angles very accurately was important. The process of determining the angles and reducing these pressure gradients involved establishing expected velocity profiles for the spanwise and normal components of velocity.

Spanwise Velocity. Velocity measurements were made in the boundary layer after ensuring the pressure gradient in the streamwise direction was zero. These measurements indicated a significant spanwise (z-direction) and normal (y-direction) velocity component. These values were

approximately one to three percent of the freestream velocity. Initially, these values were not expected to affect the velocity profiles inside the boundary layer but proved to be sufficient to alter expected results. To reduce the pressure gradient in the z-direction, the wind tunnel had to be adjusted asymmetrically in the spanwise direction. The source of the spanwise velocity was most likely due to unbalanced boundary layer growth from top to bottom of the tunnel, flow variations from the stilling chamber, and asymmetric characteristics in the wind tunnel in the spanwise direction. For example, the optic glass in the slot protruded into the flow slightly on one edge more than on the other.

The tunnel was adjusted at each measurement location individually to reduce the spanwise flow component. To determine the necessary adjustments to the tunnel, boundary layer profiles were taken at each location. Based on past experimentation and research on ribletted plates, the flow characteristics above the riblet peaks will not have a significant spanwise component in a uniform flow field oriented along the riblets. Adjustments were made symmetrically at each streamwise location (i.e. for each top adjustment, the opposite adjustment was made on the same location at the bottom of the side wall) to maintain the pressure gradient in the streamwise direction. Boundary layer profiles above the peaks were taken between each adjustment to the tunnel. This process was repeated until the spanwise component was less than 0.2% of the freestream velocity. These small adjustments were not expected to affect the streamwise pressure gradient and was verified after all adjustments had been made to the side walls.

Normal Velocity. A zero pressure gradient in the streamwise direction also required a boundary layer to grow. A normal component of velocity was expected for this reason. Once the pressure gradient in the spanwise direction was removed, adjustments to the back wall were necessary to adjust the velocity component normal to the test plate. Initially, a negative normal velocity was

introduced at the leading edge of the plate to ensure the flow was attached. By having the flow turned too much, it tripped the flow to turbulent conditions closer to the leading edge. High turning angles at the leading edge also took a significant distance along the plate to dampen out of the flow.

For the zero pressure gradient case, the normal velocity component was compared to the Blasius values in the boundary layer and was expected to diminish in the freestream. Over a ribletted plate, previous investigations have shown the boundary layer grows more than for a flat plate. The normal velocity component would be expected to be slightly higher than the Blasius values in the zero pressure gradient boundary layer.

The back wall was adjusted to increase the tunnel velocity while trying to reduce any high turning angles at the leading edge. With a sharp leading edge and a significant wedge angle (30 degrees), the flow needed to be turned in front of the plate to produce smooth streamwise flow over the test section. By allowing more air to flow behind the plate, the air flow over the test section becomes more uniform and attached to the plate. Cotton tufts placed on the leading edge of the plate provided visualization of the turbulence in the boundary layer flow. As the opening on the back side of the plate was closed (far side wall moved toward the test plate), the flow becomes separated on the leading edge. Initially, the back wall of the test section was adjusted to minimize the freestream turbulence. The expansion angle of the wind tunnel near the leading edge was set to account for the wedge angle of the plate. By adjusting the back wall of the tunnel, laminar flow was possible for a significant portion of the ribletted plate. The zero pressure gradient case suggested the turbulence levels remained low until approximately $x = 300$ mm and delayed higher turbulence levels until after $x = 400$ mm.

To determine the necessary adjustments to the back wall, the investigator measured turbulence levels in the boundary layer at several testing locations along the plate. Adjustments to the tunnel were made until the expected velocity profiles were met. Small adjustments to the measured transformation misalignment angles were necessary as well. The reason for the adjustments were the small movement ($< \pm 0.5$ mm) of the test plate in the test section and the difficulty involved in measuring the angles within $\pm 0.5°$ accuracy. This method provided accurate values of the transformation angles with an expected error of less than ± 0.1 degree. During this process, the streamwise velocity was maintained at a constant value for the length of the test section and was verified after adjustments to the tunnel were completed.

4.4.3 Adverse Pressure Gradient

The adverse pressure gradients were established in the tunnel by adjusting the side wall above the test plate. Since both Falkner-Skan flows and equilibrium flows follow a power law distribution ($U(x) = Kx^m$), this model was used to determine the velocity distributions. With the leading edge of the plate in a laminar state, the specified Falkner-Skan pressure gradient variable (β) was used to characterize the velocity distribution requirements. The Clauser equilibrium parameter (β_c) was then calculated for the flow field in the tunnel. Values for β were set at -0.1 and -0.18. These represent a moderate pressure gradient and a strong pressure gradient. Since the adjustment process for the zero pressure gradient condition determined accurate transformation angles, the adjustments took considerably less time.

4.5 Data Reduction

Velocity data was taken in three distinct profiles; freestream velocity profiles in the streamwise direction, boundary layer profiles in the normal direction above the riblet peaks, and grid profiles between the riblet peaks. Each of these data sets were accomplished for the three tunnel pressure

gradient conditions. Repeating the profiles several times at the same locations and conditions provided a means to ensemble average the results and increased the confidence of the measured value. This method resulted in a time average profile for each of the data sets. Employing Chauvenet's criteria for rejecting anomalous data readings also increased the confidence of the measured values (King, 1997).

4.5.1 Freestream velocity sweeps

Velocity sweeps were taken five to seven times at the same locations and tunnel operating conditions. The velocity sweeps started at x = 80 mm and traversed to 480 mm in 50 mm increments. The Burstware® software provided a time weighted velocity average for each data point using Equation 4-1 where Δt is the dwell time for each seeding flow particle within the measurement volume. The time averaging balances the effect of the higher speed particles with the lower speed particles to provide an accurate measurement of the average velocity components.

$$\bar{u} = \frac{\sum u_i \Delta t_i}{\sum \Delta t_i} \tag{4-1}$$

The LDA system took 2000 Doppler burst readings at each data point and performed both hardware and software coincidence filtering on the raw data to remove inaccurate measurements. The filtered values were then transformed to the laboratory coordinate system using the transformation matrix of Appendix B.

4.5.2 Boundary Layer Profiles

The boundary layer profiles began at 0.3 mm from the surface of the plate (or peak of the riblet). Finding the surface relied on the amount of surface reflections the LDA system experienced. These reflections adversely affected the data and made it difficult to take accurate readings very close to the surface. The LDA system took 1000 Doppler burst readings at each of the traverse locations. To

ensure highly confident data, each boundary layer profile was repeated from five to ten times and ensemble averaged. The highly sensitive data measurements for turbulence profiles required several samples to increase reliability and confidence level. This data was treated in the same manner as the freestream velocity sweeps by the LDA system. The transformation matrix of Appendix B converted the measured velocities to laboratory coordinates.

4.5.3 Grid Profiles

The grid profiles were positioned to take readings between the riblet peaks and into the valley. The profile consisted of 117 data points. Each profile was repeated three to five times at each location taking 1000 Doppler bursts at each data point. The LDA traverse system program moved the measurement volume from point to point. The spacing was 0.3 mm between each grid point. The profile provided a symmetric grid pattern in the riblet valley. The velocity measurements in the grid profile were expected to be symmetric. Preliminary data showed this to be the case for all flow conditions where surface roughness was not a major factor. The effects of asymmetric surface roughness in a riblet valley is discussed in Chapter 5. The grid profile can be seen in Figure 4-3.

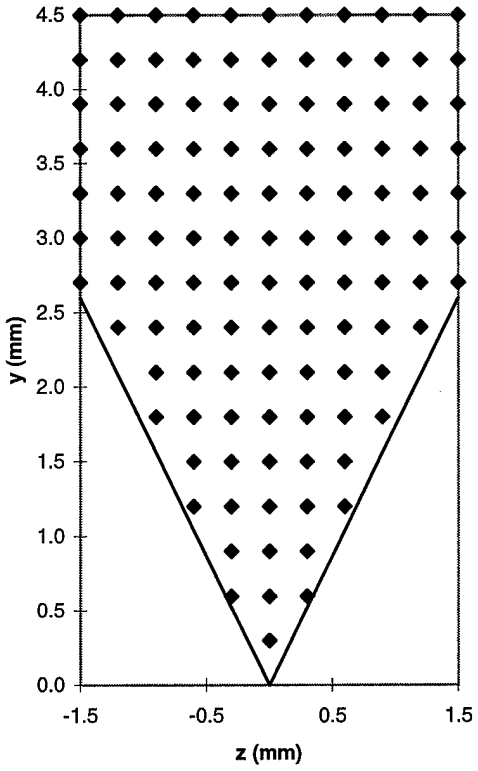

Figure 4-2: Traverse grid pattern for LDA measurements

The starting point for the LDA traverse system was the point above the peak at z = -1.5 mm in Figure 4-3. Due to the sensitivity of the traverse system being only 0.05 mm, some small misalignment errors were experienced.

4.5.4 Chauvenet's Criterion and Confidence Interval

Chauvenet's criterion provided a method to eliminate highly spurious data readings that did not characterize the flow properties properly. The criterion suggests the data values should not be so far away from the mean that measuring twice as many samples would be required to justify its retention. The average value and the standard deviation determine the range of valid data. For each of the data sets, the appropriate criteria apply at each point. This criteria was defined as a multiple of the standard deviation from the mean. Table 4-2 provides the multiples used for this investigation.

Table 4-2: Chauvenet criterion statistics

Samples	Multiple (K)
3	1.38
5	1.65
7	1.80
10	1.96

From the measured samples for the velocity information, a statistic was calculated and compared to the values in Table 4-2. Equation 4-2 shows the calculation of the statistic (X).

$$X = \frac{\left(x_i - \bar{x}\right)}{s} \tag{4-2}$$

The confidence interval for the data was set at 95%. From the confidence interval, error bars provided a range for the average values using a statistical Student t-distribution (Kiemele et al., 1990).

$$\bar{x} \pm t\left(1 - \alpha/2, n-1\right)\frac{s}{\sqrt{n}} \tag{4-3}$$

Equation 4-3 provided the tool to calculate the 95% confidence interval for the boundary layer velocity profiles, the freestream velocity sweeps, and calculated turbulence levels.

4.6 Chapter Summary

This chapter addressed the major steps in this investigation's construction and execution. The wind tunnel construction and air supply provided the necessary components for controlling and developing the flow over the test plates. The Laser Doppler Anemometry system measured the velocity information in the flow without disturbing the flow field itself. The setup and fine tuning of this system proved to be critical to the accurate and timely data acquisition process. Software control and processing parameters were established at the appropriate values to make measurements in the ranges for this wind tunnel set up and to produce accurate values.

Once the equipment was in place and operating properly, the wind tunnel was adjusted to the desired flow conditions. Measurements with the LDA system were used to indicate which direction to adjust the sides of the wind tunnel test section for each flow condition. Once the measurements were taken for each test condition, the data were transformed to the wind tunnel coordinate system and scrutinized to ensure confidence in the results.

5. Results and Discussion

To satisfy the objectives for this investigation, data were taken at several locations along the test plate to include laminar, transitional, and turbulent flow fields for each targeted pressure gradient flow condition (β = 0.0, -0.1, and -0.18). The first objective required the determination of the flow field over the flat plate for the specified pressure gradients (β = 0.0, -0.1, and -0.18). This testing allowed the investigator to compare similar flow field conditions (laminar, transitional, or turbulent) at different pressure gradients. To accomplish the second objective, measurements were made in the riblet valley and in boundary layer profiles above the flat plate. These measurements were used to investigate the velocities, turbulence, skewness, flatness, and Reynolds stress in the riblet valley and near the riblet surfaces. The investigator also used this data to model the boundary layer above the plate. Another important factor to this research project was the results addressed by the third objective, comparing local skin friction with predicted flat plate values. This comparison was carried out using an average local skin friction coefficient as calculated at a specific streamwise location on the test plate.

Before satisfying the objectives stated above, several key requirements were accomplished first. Smooth plate flow needed to be investigated to ensure the testing procedures and equipment could produce and measure a known flow condition. These procedures and equipment could then be applied to the unknown flow conditions of the ribletted plate with some confidence. Another requirement included establishing specified flow conditions in the wind tunnel. Each pressure gradient condition needed to be determined and established before boundary layer measurements were taken. This required adjusting the tunnel to produce expected velocity profiles in the

freestream for each pressure gradient condition. In order to compare the measured boundary layer profiles at different conditions and locations along the plate, determination of the virtual origin was also important.

5.1 Smooth, Flat Plate Flow

The author used the measured velocities over the smooth, flat plate to validate the wind tunnel and testing procedures for the LDA system. To validate the wind tunnel, the goal was to show the tunnel could produce a specified flow condition and the flow parameter measuring system (LDA) could produce accurate information. The wind tunnel flow condition was adjusted to a zero pressure gradient to be able to compare the results to a known analytical solution, the Blasius boundary layer. Using local peak turbulence values, the flow conditions over the flat plate were determined to be laminar over the range of $0 < x < 400 \pm 50$ mm base on turbulence intensity and boundary layer profile. The maximum local freestream Reynolds number over this range was less than 155,000. For a smooth, flat plate, laminar flow is expected for local Reynolds numbers below 500,000 (White, 1991). For this reason, the velocity profiles could be compared to the Blasius boundary layer solution; smooth, flat plate flow under a zero pressure gradient condition.

5.1.1 Velocity Profiles for a Smooth, Flat Plate

When plotted using the similarity variable (η), these profiles followed the Blasius profile. Normal and spanwise velocity components conformed to the expected values as well. Figure 5-1 shows the measured values at streamwise locations of 200 and 400 mm.

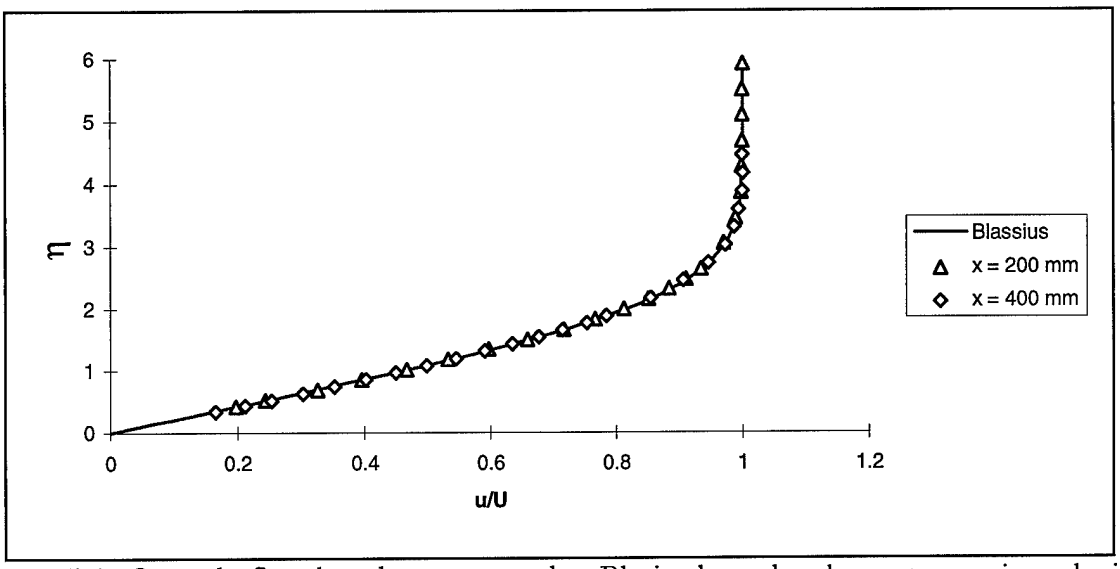

Figure 5-1: Smooth, flat plate data compared to Blasius boundary layer streamwise velocity component

The normal velocity component (v) followed the calculated Blasius values as well (Figure 5-2). At such small values as seen in Figure 5-2, the turbulence in the freestream causes higher levels of variations. Since the velocity profiles matched the Blasius boundary layer profiles, confidence in the transformation angles was also increased.

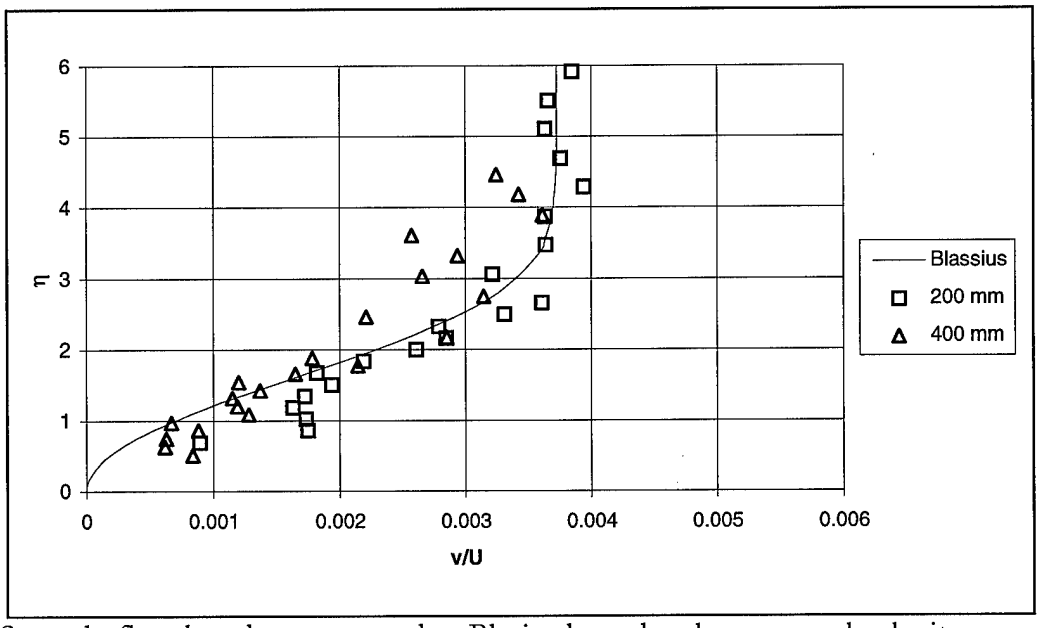

5-2: Smooth, flat plate data compared to Blasius boundary layer normal velocity component

5.1.2 Freestream Turbulence Intensity

For the smooth plate, turbulence intensity variations were also addressed to establish wind tunnel characteristics. Initial freestream turbulence levels were measured from 2.0 to 2.5 %. By adjusting the side wall behind the test plate, these values were minimized to approximately 1.8% in the freestream as seen in Figure 5-3 for 200 mm from the leading edge. This figure shows the turbulence intensity levels were fairly constant up to the surface. At approximately three millimeters from the surface, the turbulence levels increased to approximately 2%.

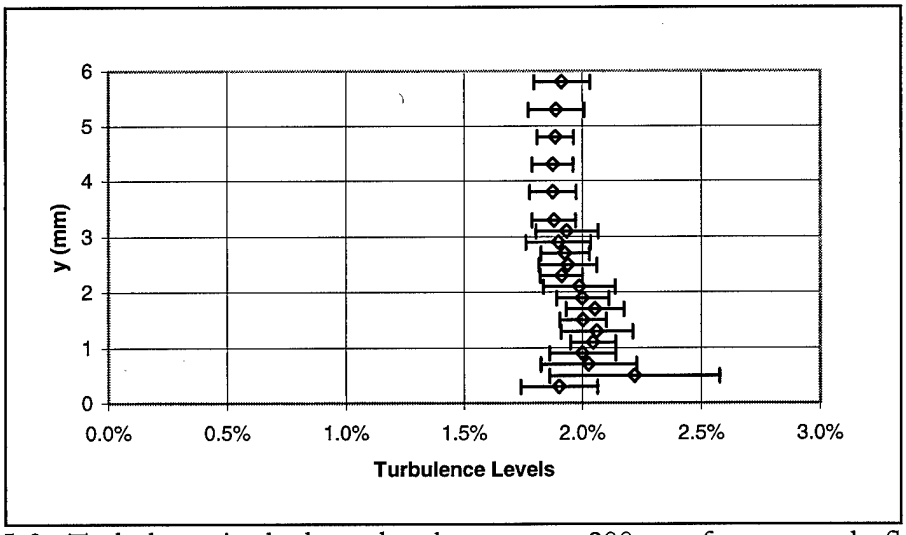

Figure 5-3: Turbulence in the boundary layer at x = 200 mm for a smooth, flat plate

This freestream turbulence was most likely generated from inside the stilling chamber and from the air supply system. Turbulence levels in the boundary layer were observed to be a little more pronounced at 400 mm from the plate leading edge (Figure 5-4). The freestream turbulence levels were the same as those at 200 mm. With an expected thicker boundary layer at 400 mm, the increase to 2% near the surface would be expected to occur farther from the surface than for the 200 mm case. This is shown in Figure 5-4 with the increase occurring near four millimeters from the surface and reading a maximum of 2.55%. Another interesting characteristic of this figure is the

increased variability of the turbulence intensity very near the surface, at less than one millimeter height. The variability indicates the flow field is moving from a laminar to a more transitional state.

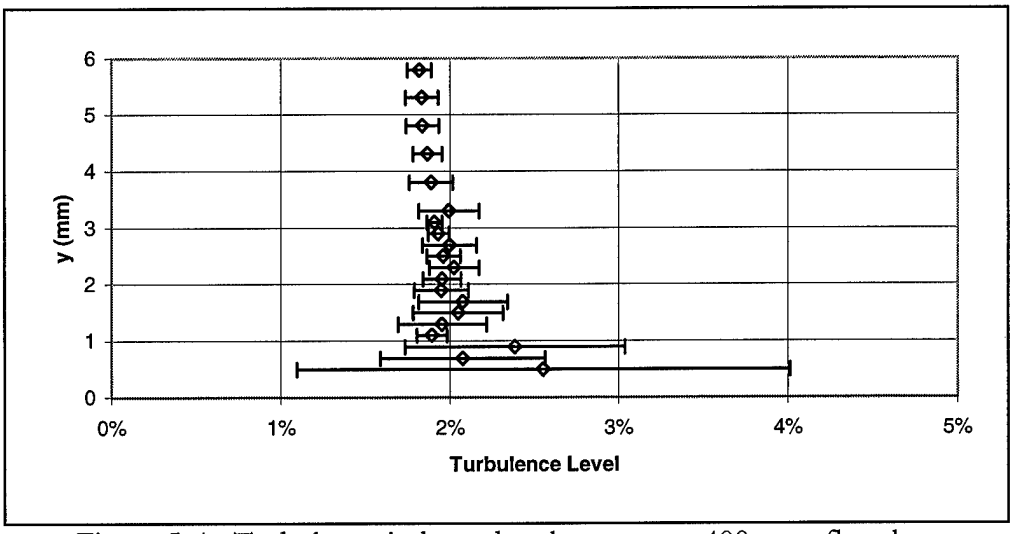

Figure 5-4: Turbulence in boundary layer at x = 400 mm, flat plate

5.2 Ribletted Plate Pressure Gradient and Virtual Origin

To establish the three pressure gradient conditions, streamwise velocity profiles were measured in the freestream at 30 mm from the plate. Normal boundary layer profiles and grid profiles were taken at each of the streamwise locations being investigated. A virtual origin (Section 2.2.2) was also needed to compare the boundary layer profiles. The grid measurements provided streamwise velocity, normal-spanwise velocity vector distribution, skewness, flatness and turbulence intensities. This data also provided a means to calculate an average, local skin friction coefficient for the ribletted plate. Table 5-1 provides the locations and local Reynolds numbers for each of the locations on the ribletted plate tested.

Table 5-1: Streamwise Reynolds number

x (mm)	$\beta = 0.00$	$\beta = -0.10$	$\beta = -0.18$
80	25377	25143	27733
200	61360	63536	65820
300		94216	
400	122682	123627	123880
440		132501	
468	152427		

5.2.1 Measurement of Pressure Gradient

To establish each of the pressure gradient conditions in the wind tunnel, the freestream velocity was measured along the streamwise direction. Adjustments were made to the tunnel after each measurement to attain the desired velocity profile for the specified pressure gradients. The pressure gradient was described by the Falkner-Skan pressure gradient variable, β. The targeted pressure gradients for this investigation included $\beta = 0.0$, -0.1 and -0.18. For these modest pressure gradients, flow will remain attached to the plate for the entire length of the test section. The Falkner-Skan power law velocity distribution necessary to achieve the specified pressure gradients also produced equilibrium flow for the turbulent flow conditions. For equilibrium flow of a turbulent boundary layer, the Clauser equilibrium parameter (β_c) is constant. Values of β_c were calculated at the various locations along the tunnel. The values achieved included $\beta_c = 0.0$, 0.20 ± 0.04, and 0.33 ± 0.01 for each of the respective pressure gradient conditions ($\beta = 0.0$, -0.1, and -0.18).

Zero Pressure Gradient. Figure 5-5 shows the velocity distribution in the streamwise direction 30 mm in the normal direction from the test plate (riblet peak) for the first targeted pressure gradient, $\beta = 0.0$. This figure shows very small variations from a constant velocity which indicates the pressure was nearly constant for the length of the test section. The slight variations from the linear profile

(0.26% maximum) resulted largely from the traverse movements in the streamwise direction and the slight angle variations between each measurement point in the optic glass installed in the side of the wind tunnel. During the traverse movements over the long distances (50 mm) between measurement points, the vibrations caused very small alignment changes in the measurement volume. The vibrations were measured with an accelerometer and damped out quickly. These vibrations still introduces some uncertainty. Also, slight angle differences in the optic glass bend the laser beams slightly different from location to location. These variations (traverse vibrations and optic glass angle differences) did not affect measurements taken for the boundary layer or grid profiles. These profiles required smaller traverse distances at a slower traverse speed (much lower vibration as seen with the accelerometer and damp out nearly instantaneously). Also, these profiles were taken where there were no changes in the optic glass angles.

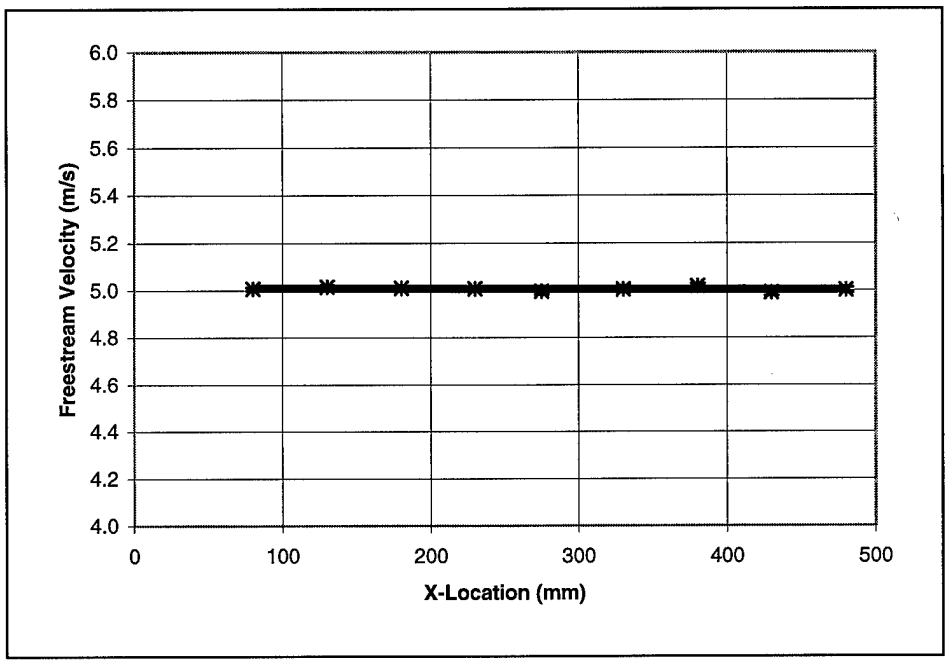

Figure 5-5: Freestream, streamwise velocity (U), $\beta = 0.0$

The variations in the freestream velocity profiles were more pronounced in the normal (v) and spanwise (w) velocity components due to the much smaller values. Figure 5-6 shows the variations

in these velocity components. The most significant effect causing these velocities to vary from point to point were the slight angle changes in the optic glass. These angles would affect the transformation angles used to convert the measured data to the laboratory coordinates. The angle variations were on the order of 0.1 deg.

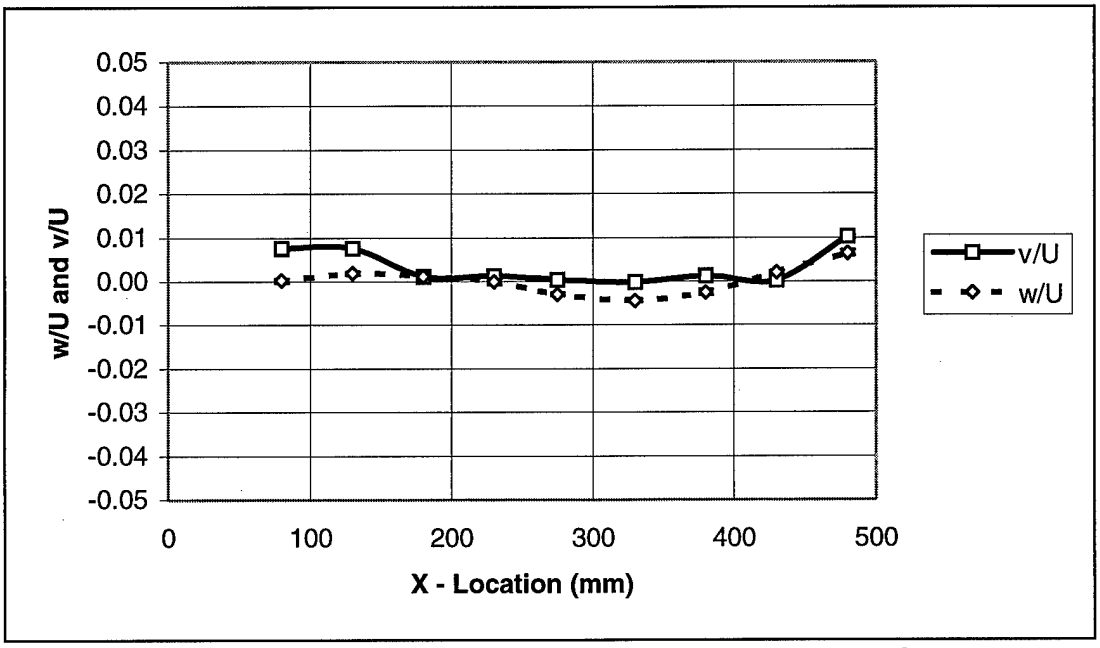

Figure 5-6: Freestream, spanwise (w) and normal (v) velocity, $\beta = 0.0$

Adverse Pressure Gradient, β = -0.1 and -0.18. For the first adverse pressure gradient (β = -0.1), Figures 5-7 and 5-8 show the velocity distributions for the three components. The velocity followed the power law velocity distribution for the streamwise component. The spanwise velocity (w/U) was 0 ± 0.005 for the entire test section of the tunnel. The normal component was slightly greater than zero for this case. For an adverse pressure gradient, the wind tunnel walls diverge. This divergence caused the stream tubes to expand along the length of the tunnel. This positive normal velocity component was necessary in the freestream to ensure continuity. The profiles for the second adverse pressure gradient followed the same patterns as the first pressure gradient (Figures 5-9 and 5-10).

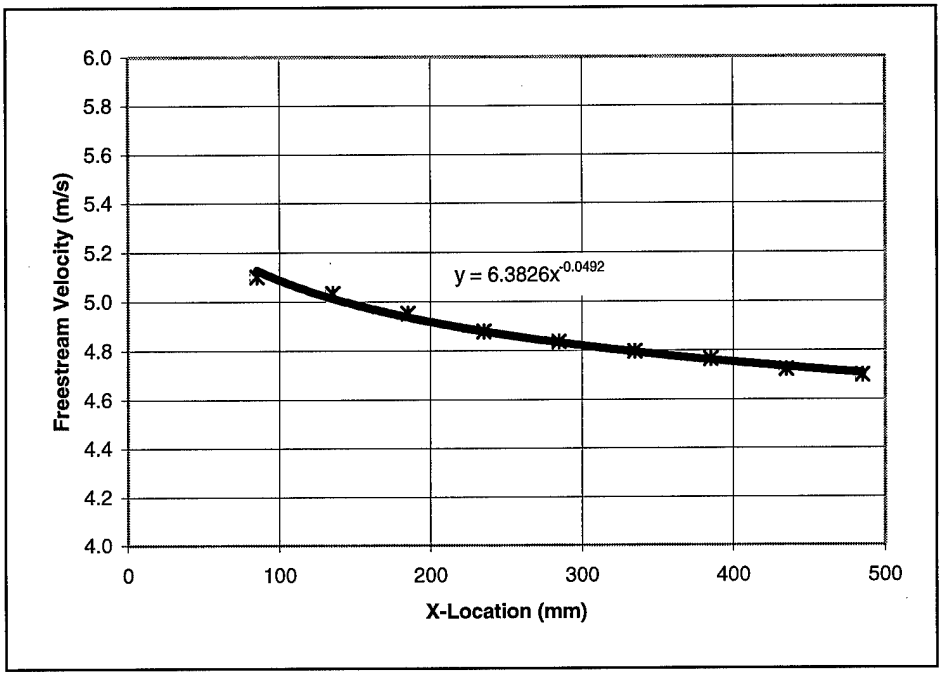

Figure 5-7: Freestream, streamwise velocity (U), β = -0.1, y = 30 mm

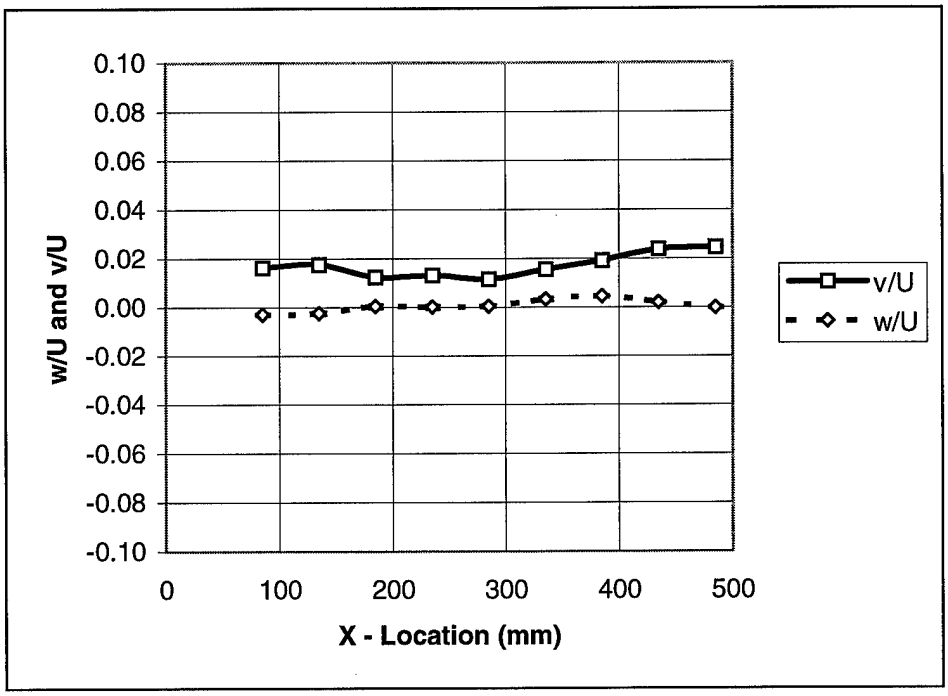

Figure 5-8: Freestream, spanwise (w) and normal (v) velocity, β = -0.1, y = 30 mm

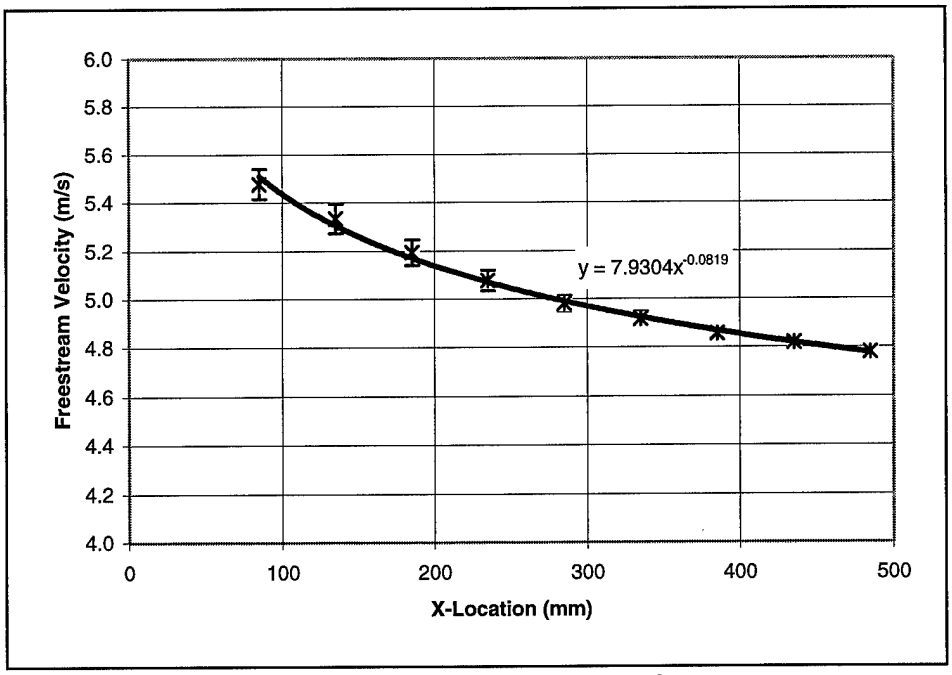

Figure 5-9: Freestream, streamwise velocity (U), β = -0.18, y = 30 mm

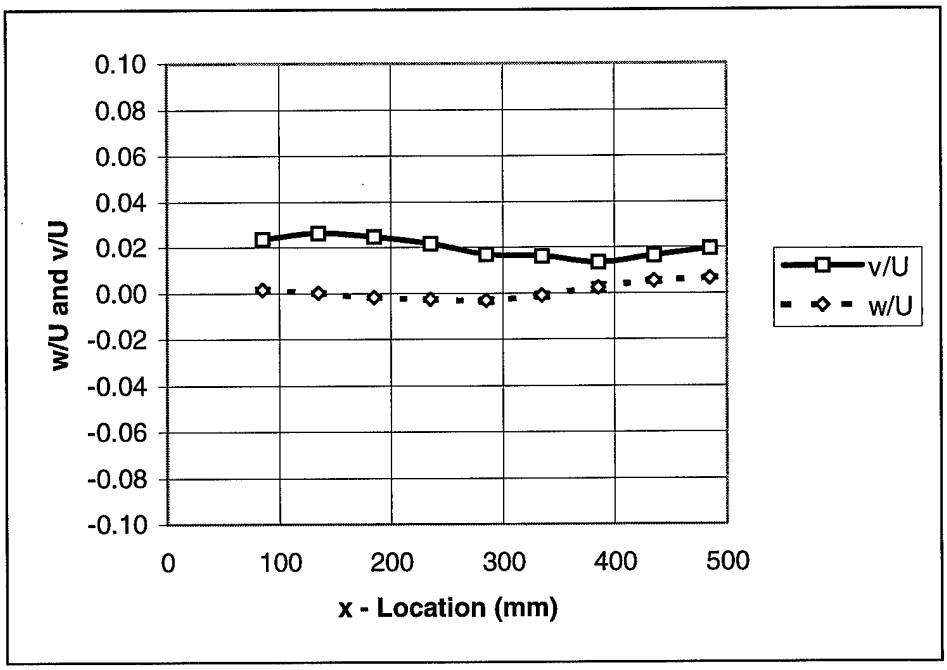

Figure 5-10: Freestream, spanwise (w) and normal (v) velocity, β = -0.18, y = 30 mm

Although difficult to see in some of the Figures 5-5 through 5-10, confidence error bars are present in the figures for each data point. The confidence level was established at 95% and

calculated as discussed in Section 4.6.4. Maximum confidence levels never exceeded 1.1% of the freestream velocity (occurred for β = -0.18, u/U). Most levels were less than 0.5% of the freestream velocity value.

5.2.2 Determination Of The Virtual Origin For Each Boundary Layer Profile

The normal velocity profiles were grouped into categories based on whether the flow field was laminar, transitional or turbulent. Turbulence intensity levels and boundary layer profiles were used to define these flow field conditions. The boundary layer profiles were compared by first shifting each curve to a specific virtual origin. Laminar and transitional flows were plotted and compared using the Falkner-Skan similarity variable, η (Equation 2-7). Turbulent and transitional flows were investigated using both edge and wall variables.

A virtual origin (y_o) as discussed in Section 2.2.2 provided a means to compare the velocity profiles obtained at different locations and flow conditions. The virtual origin was determined with either of two distinct methods, linear fit or location of maximum turbulence (Equation 2-21). The first method provided reliable values for laminar and transitional flows, while the maximum turbulence method applied to turbulent flow fields. Table 5-2 shows the values determined for each boundary layer profile in laboratory coordinates (y = 0, bottom of the riblet valley). These virtual origins were used to shift the normal coordinate to a zero condition.

Table 5-2: Virtual origin (mm), y_o

x (mm)	β = 0.00	β = -0.10	β = -0.18
80	1.65	2.30	1.65
200	1.52	2.20	2.10
300	--	2.00	--
400	2.50	2.11	1.65[1]
440	--	1.70[1]	--
468	1.60[1]	--	--

1. Using Equation 2-21

The velocity profiles were expected to be independent of spanwise location (peak or valley) at measurement locations above the ribletted plate. Near the plate, some variations were expected due to the influence of the riblets machined into the surface. For the laminar case, the velocity profiles showed the these variations very close to the riblet surfaces. As seen in Figure 5-11, the streamwise velocity profiles did differ near the surface but converge just above the plate.

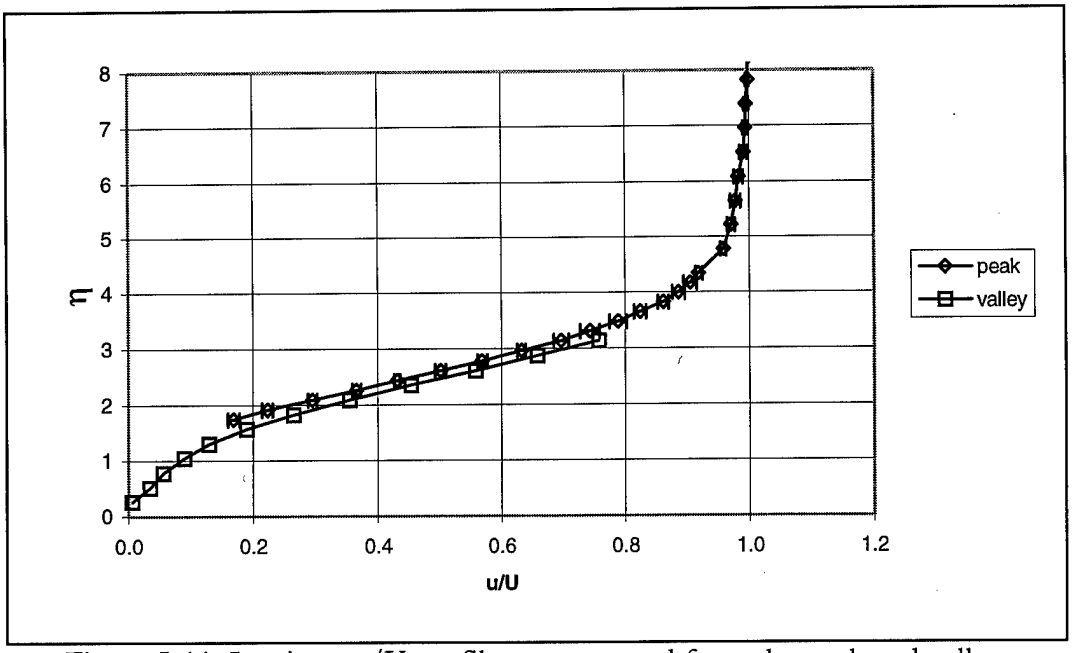

Figure 5-11: Laminar, u/U profiles as measured from the peak and valley, x = 200 mm, β = -0.1

The slight variation between the velocity measurements between values measured above the valley and above the peak arose from position error introduced by the traverse system tolerances and positioning of the measurement volume near the surface. Figure 5-11 was in laboratory coordinates with the origin being at the base of the riblet valley.

For turbulent flow, boundary layer profiles converged as well. Figure 5-12 shows a turbulent profile with both peak and valley streamwise velocity profiles. This figure shows the influence of the riblets on the velocity profile to extend higher into the freestream than for the laminar case (Figure 5-11), but they do converge.

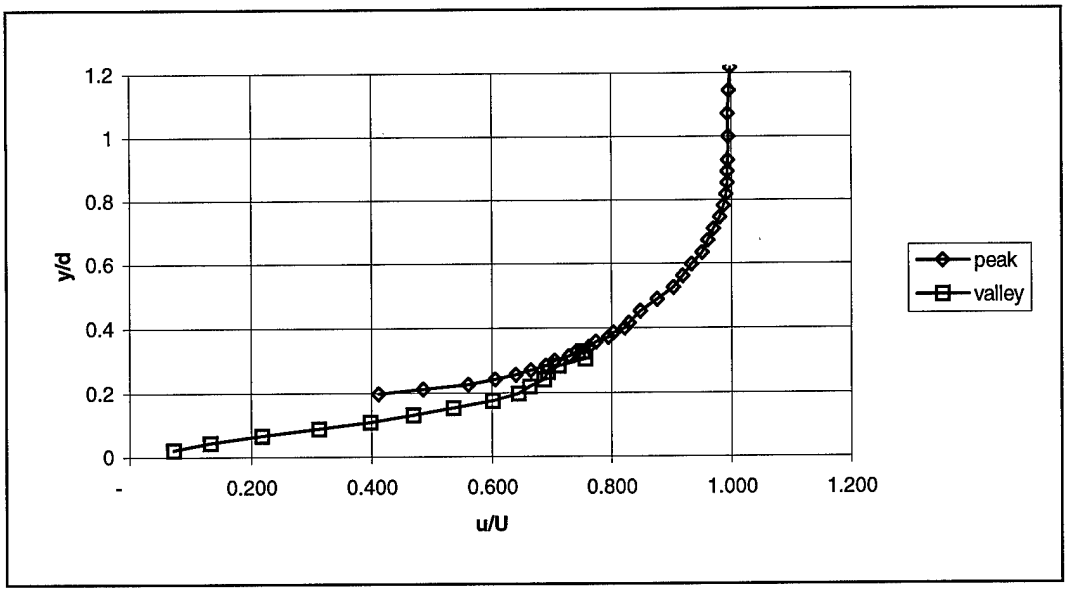

Figure 5-12: Turbulent, u/U profiles measured above peak and valley, x = 468 mm, $\beta = 0.0$

5.3 Flow Field Determination

To determine the flow field states, the turbulence intensity and boundary layer profiles were used. Initially, Equation 2-5 was used to determine the flow field state based on the turbulence intensity criteria. Flows with peak turbulence levels in the boundary layer below 3% of the freestream velocity were considered laminar. Above 9% turbulence intensity, flow was considered turbulent and flow fields with values between 3% and 9% were transitional. Table 5-3 provides a quick summary of the determination made based on these criterion.

Table 5-3: Flow field condition based on turbulence intensity

x (mm)	$\beta = 0.0$	$\beta = -0.1$	$\beta = -0.18$
80	Laminar	Laminar	Laminar
200	Laminar	Laminar	Transitional
300		Transitional	
400	Transitional	Transitional	Turbulent
440		Turbulent	
468	Turbulent		

The velocity profiles were used to provide further evidence of the flow field state at each streamwise location and flow condition. Using a modified Falkner-Skan similarity variable (Equation 5-1), laminar flow conditions provided velocity profiles which collapsed to the same curve. Turbulent flow boundary layer profiles collapsed to the same curve at a specified pressure gradient when plotted in edge variables. All laminar and transitional profiles were plotted in Figure 5-13 (transitional flow fields indicated in bold) in the similarity variables measured from the virtual origin (Equation 5-1). All turbulent and transitional profiles are plotted in Figure 5-14 (transitional flow fields indicated in bold) using edge variables starting at the virtual origin (Equation 5-2).

$$\eta_o = (y - y_o)\sqrt{\frac{(m+1)U(x)}{2\nu x}} \tag{5-1}$$

$$\left(\frac{y}{\delta}\right)_o = \frac{y - y_o}{\delta - y_o} \tag{5-2}$$

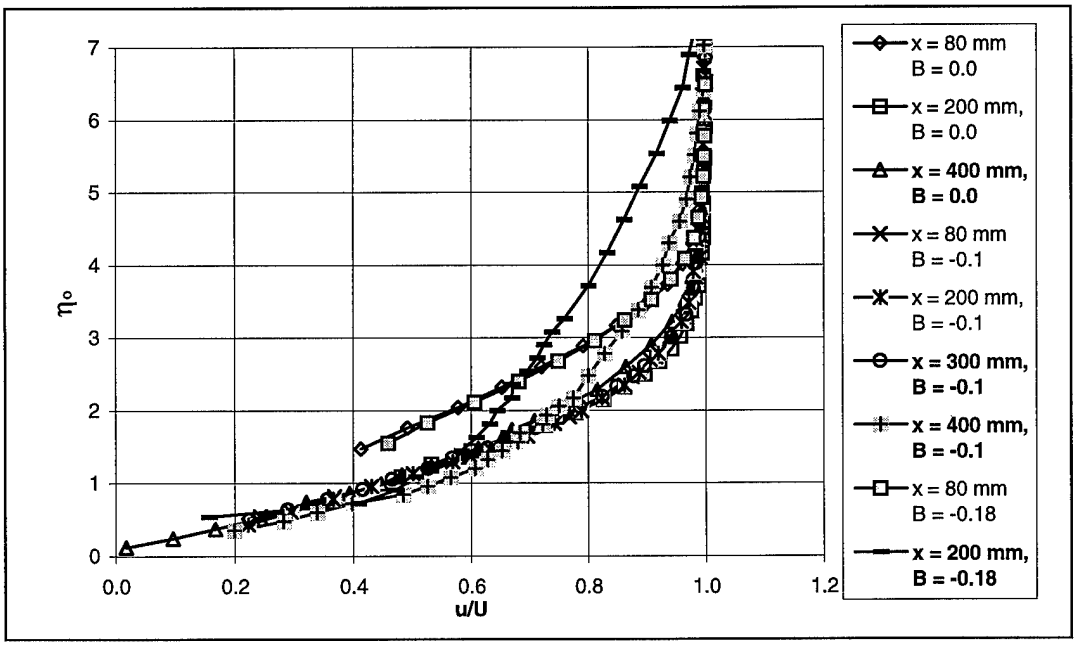

Figure 5-13: Laminar and transitional velocity profiles in η_o, transitional flow fields identified by bold text

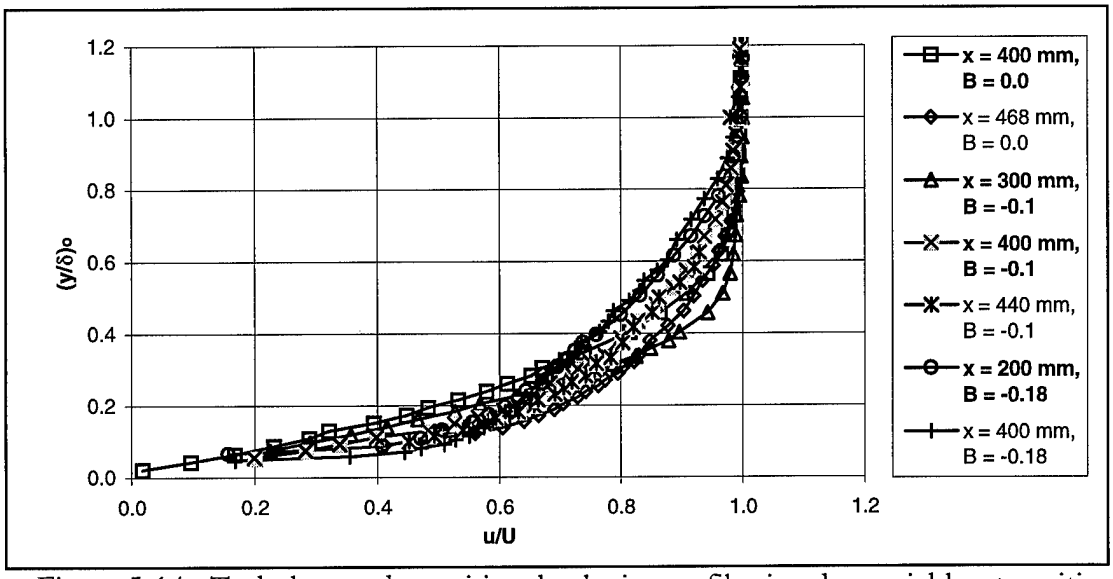

Figure 5-14: Turbulent and transitional velocity profiles in edge variables, transitional flow fields identified by bold text

From these velocity profiles, two changes were made to the determinations in Table 5-3. Table 5-4 contains the flow field character based on the boundary layer shape. Although the turbulence intensity for x = 300 mm, β = -0.1 exceeds 4%, the boundary layer conforms to the laminar profiles (Figure 5-13). Also, Figure 5-14 shows x = 200, β = -0.18 collapsing with the boundary layer profile for x = 400 mm, β = -0.18, defining it as turbulent.

Table 5-4: Flow field conditions

x (mm)	β = 0.0	β = -0.1	β = -0.18
80	Laminar	Laminar	Laminar
200	Laminar	Laminar	Turbulent[1]
300		Laminar[1]	
400	Transitional	Transitional	Turbulent
440		Turbulent	
468	Turbulent		

1. Identified as transitional flow by turbulence intensity criteria

The flow states in Table 5-4 were used as the final determination of the flow conditions for the tested locations along the ribletted plate. Based on these flow states, approximate ranges for each of

the flow conditions were determined. Table 5-5 provides predicted ranges for the flow fields for each pressure gradient.

Table 5-5: Flow field condition ranges

Condition	$\beta = 0.0$	$\beta = -0.1$	$\beta = -0.18$
Laminar	0 - 350±50 mm	0 - 350±25 mm	0 - 100±50 mm
Transitional	350±50 - 425±25 mm	350±25 - 420±20 mm	100±50 - 200±25 mm
Turbulent	425+ mm	420+ mm	200+ mm

5.4 Development of Streamwise Velocity in the Riblet Valley

The streamwise velocity in the riblet valley showed the extent to which the higher momentum flow penetrated into the riblet valley. The deeper into the valley this higher momentum flow appeared indicated a higher level of kinetic energy dissipation near the riblet walls and higher expected drag.

Figures 5-15 through 5-18 show the u/U contour map in the riblet valley for a zero pressure gradient. For Figure 5-15, the boundary layer thickness was slightly less than the riblet spacing as discussed in Section 5.2.2. The boundary layer was formed in the riblet valley instead of over the flat plate. Figure 5-15 exhibits this by the boundary layer thickness being at a higher coordinate above the peak than the valley as seen by the $u/U = 0.9$ contour. Higher momentum flow penetrates deep into the valley for this case. With the boundary layer thickness increasing in the streamwise direction, Figures 5-16 through 5-18 exhibit contours for a boundary layer developed over the plate. At the mid-plane ($y = 1.3$), Figure 5-16 showed relatively low velocity levels suggesting little penetration of higher momentum flow in this area. As the flow turbulence intensities increased, the average velocities in the riblet valley increased (Figure 5-17). The velocity levels below the mid-plane showed little change between the transitional (Figure 5-17) and turbulent (Figure 5-18) cases.

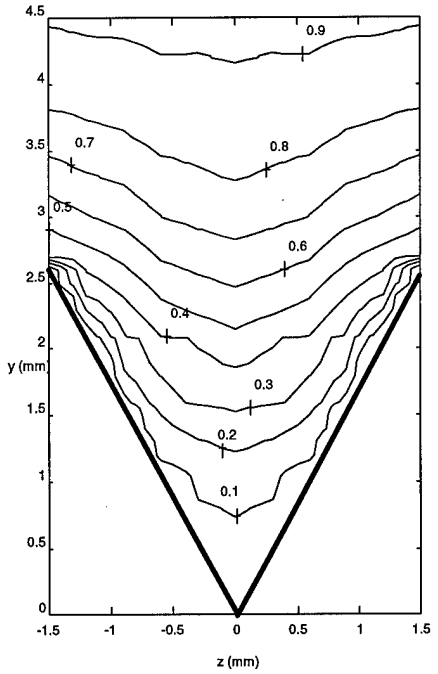

Figure 5-15: Laminar, u/U, x = 80 mm, $\beta = 0.0$

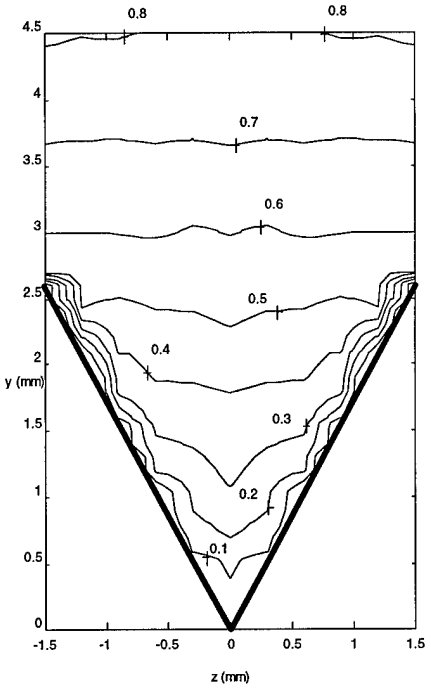

Figure 5-17: Transitional, u/U, x = 400 mm, $\beta = 0.0$

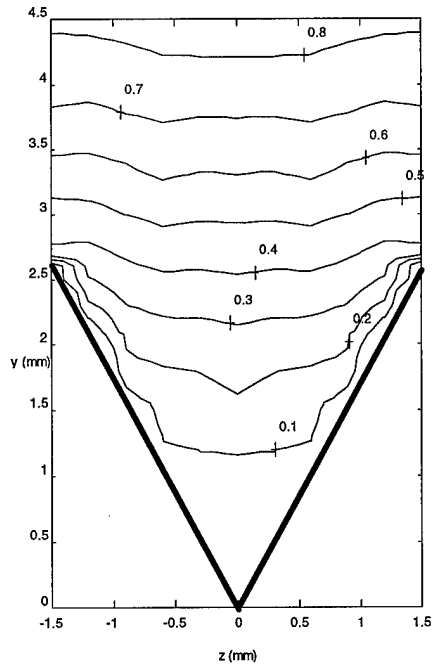

Figure 5-16: Laminar, u/U, x = 200 mm, $\beta = 0.0$

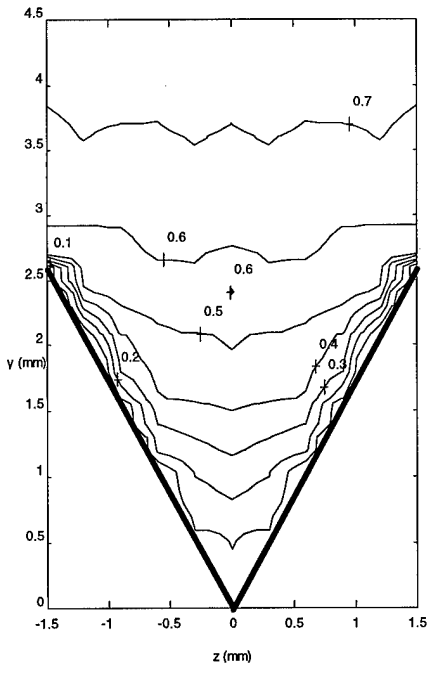

Figure 5-18: Turbulent, u/U, x = 468 mm, $\beta = 0.0$

For the adverse pressure gradient condition $\beta = -0.1$, the velocity profiles showed similar results. For x = 80 with a boundary layer thickness nearly the same size as the riblet spacing (Figure 5-19), the higher momentum flow penetrated deep into the valley. The boundary layer was developing over the flat plate but still caused a large velocity gradient to exist in the riblet valley for this flow condition. The laminar conditions with thicker boundary layers, x = 200 mm (Figure 5-20) and 300 mm (Figure 5-21), showed relatively smaller velocity magnitudes in the valley with values at the mid-plane at u/U = 0.1. The boundary layer had fully developed above the plate instead of in the riblet valley. The transitional flow field at x = 400 mm (Figure 5-22) showed considerably higher velocity levels deep in the riblet valley. Between the top of the riblet peaks (y = 2.6 mm), the profiles showed the velocity to be greater than u/U = 0.5. Higher velocities penetrated the valley less for the turbulent case at x = 440 mm (Figure 5-23) than for the transitional case, x = 400 mm. Also below the mid-plane and at the riblet peaks (y = 2.6 mm), velocity levels were lower, indicating a thicker boundary layer for the turbulent case.

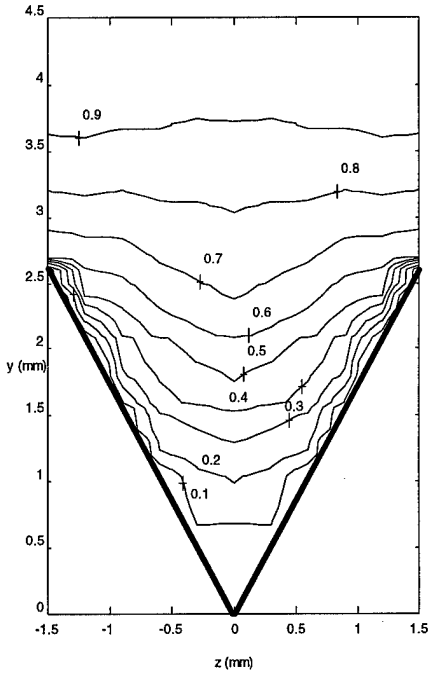

Figure 5-19: Laminar, u/U, x = 80 mm, β = -0.1

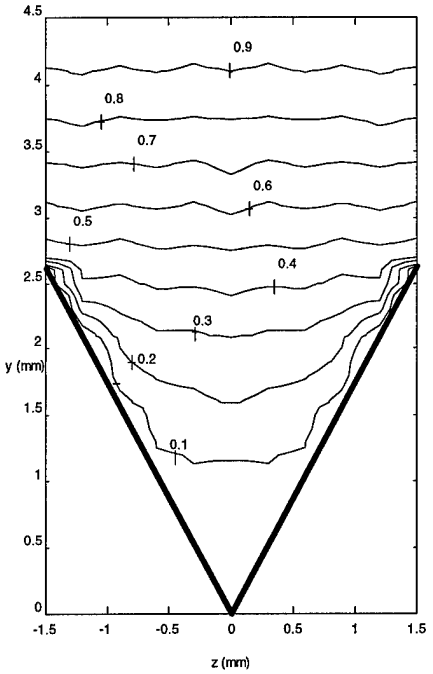

Figure 5-21: Laminar, u/U, x = 300 mm, β = -0.1

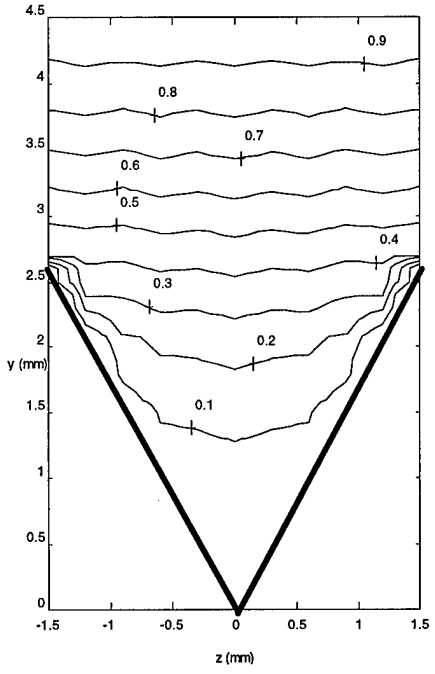

Figure 5-20: Laminar, u/U, x = 200 mm, β = -0.1

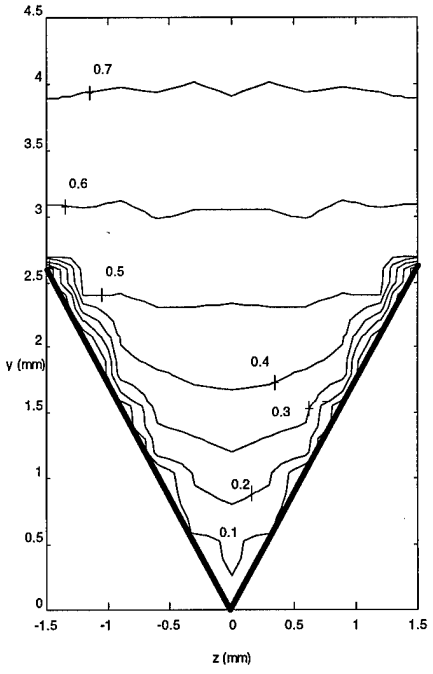

Figure 5-22: Transitional, u/U, x = 400 mm, β = -0.1

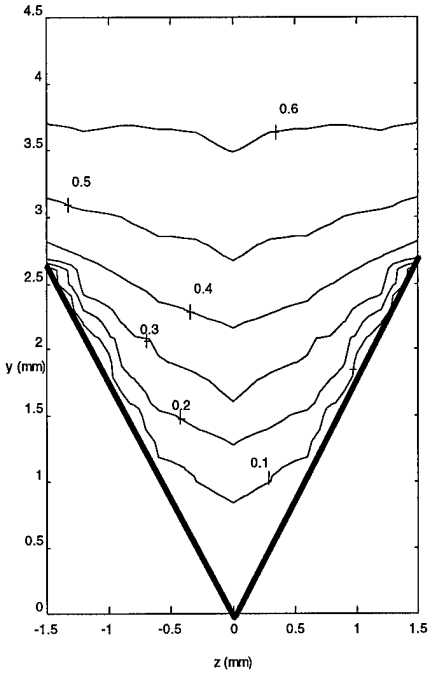

Figure 5-23: Turbulent, u/U, x = 440 mm, β = -0.1

Measurements made under an adverse pressure gradient of β = -0.18 showed the thinner laminar boundary layer (x = 80, Figure 5-24) penetrating the riblet valley as for the β = 0.0 flow conditions at this streamwise coordinate. The higher momentum flow reached into the riblet valley but not as far as the lesser pressure gradient cases. Below the mid-plane, velocity values were less than for the values seen at the same streamwise location (x = 80 mm) at the lower pressure gradients. The flow under this pressure gradient was fully turbulent at an early streamwise location. Figure 5-25, x = 200 mm, exhibits a turbulent flow field with higher momentum flow penetrating below the mid-plane as seen for transitional flow fields for other pressure gradient conditions. As the flow further developed into the turbulent regime at x = 400 mm (Figure 5-26), velocity below the mid-plane showed little change. Near the peaks, Figure 5-25 shows higher velocity levels than Figure 5-26. This corresponds to the thicker boundary layer at x = 400 mm.

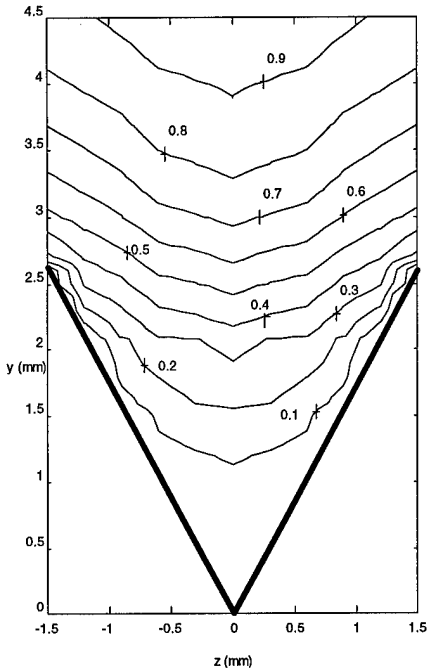

Figure 5-24: Laminar, u/U, x = 80 mm, β = -0.18

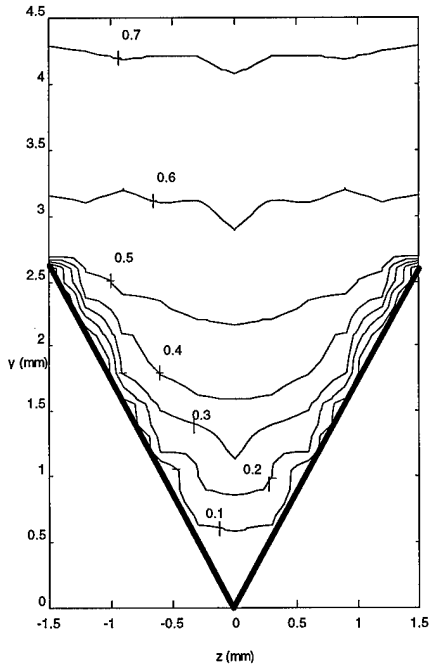

Figure 5-25: Turbulent, u/U, x = 200 mm, β = -0.18

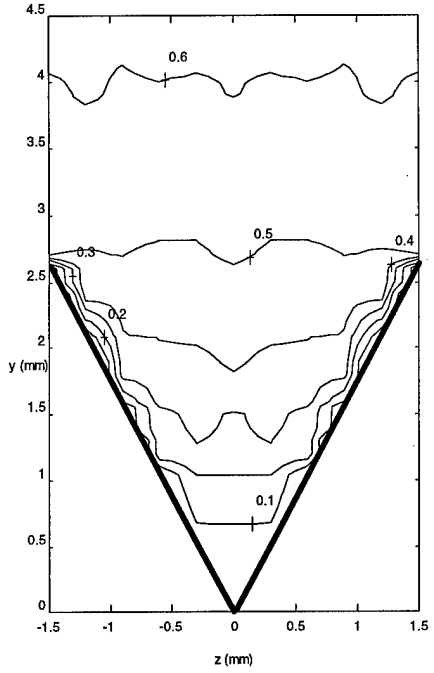

Figure 5-26: Turbulent, u/U, x = 400 mm, β = -0.18

Considering the laminar flow conditions at x = 200 for β = 0.0 (Figure 5-16) and -0.1 (Figure 5-20), the streamwise velocity appears to reduce in magnitude deeper in the valley as the adverse pressure gradient increased. With the Reynolds number for β = -0.1 (Table 5-1) at this streamwise location slightly higher than the value for β = 0.0, the boundary layer thickness would be expected to be less by Equation 5-3 (White, 1990). The boundary layer growth due to the increased adverse pressure gradient would then be the cause for the increased boundary layer thickness and the higher momentum fluid not penetrating into the valley as far as for the zero pressure gradient case.

$$\frac{\delta}{x} \propto \frac{1}{\sqrt{\mathrm{Re}_x}} \tag{5-3}$$

The transitional flow conditions (Figures 5-17 and 5-22) showed higher momentum flow penetrating deep into the riblet valley. Below the mid-plane, the velocity levels were higher than those for the fully turbulent flow fields at the same pressure gradient. Higher turbulence levels indicate more randomly occurring vortex motion being generated in the riblets. The vortex motion generated from the riblet surfaces would circulate higher energy flow deeper into the valley. Near the peak, velocity levels were higher than for the turbulent flow fields at the same pressure gradient in line with the thicker boundary layers at the fully turbulent locations (x = 468 mm, β = 0.0 and x = 440 mm, β = -0.1)

The flow over the ribletted plate showed little changes to the transitional flow condition with only the mild adverse pressure gradient. At zero pressure gradient and β = -0.1, the flow fields remained relatively laminar for a large portion of the ribletted plate (greater than 350 mm from the leading edge). Fully turbulent flow appeared at nearly the same locations in the streamwise direction on the ribletted plate. As the adverse pressure gradient increased

to β = -0.18, the flow field changes over the plate seemed to shift toward the leading edge. While laminar flow was still evident at x = 80 mm, the flow was fully turbulent at the x = 200 mm location.

5.5 Development of Turbulence Intensity in the Valley and Above Peaks

Turbulence levels indicate increases in the energy dissipation in the flow field and therefore increases in skin friction. Thus, changes in the flow field turbulence levels were of major concern. The boundary layer velocity measurements provided peak turbulence levels in the boundary layer for each flow condition. Figure 5-27 shows the laminar flow condition turbulence levels. The turbulence intensities appear to peak near $(y/\delta)_o = 0.2$. The peak values for transitional flow field conditions in Figure 5-28 are near the same location but have a significantly higher turbulence intensity throughout the entire boundary layer thickness and return to freestream turbulence levels just above the boundary layer. The turbulent flow field curves in Figure 5-29 suggest the maximum values for turbulence intensity occurred below $(y/\delta)_o = 0.2$. These curves also exhibited higher levels of turbulence for the entire boundary layer as well.

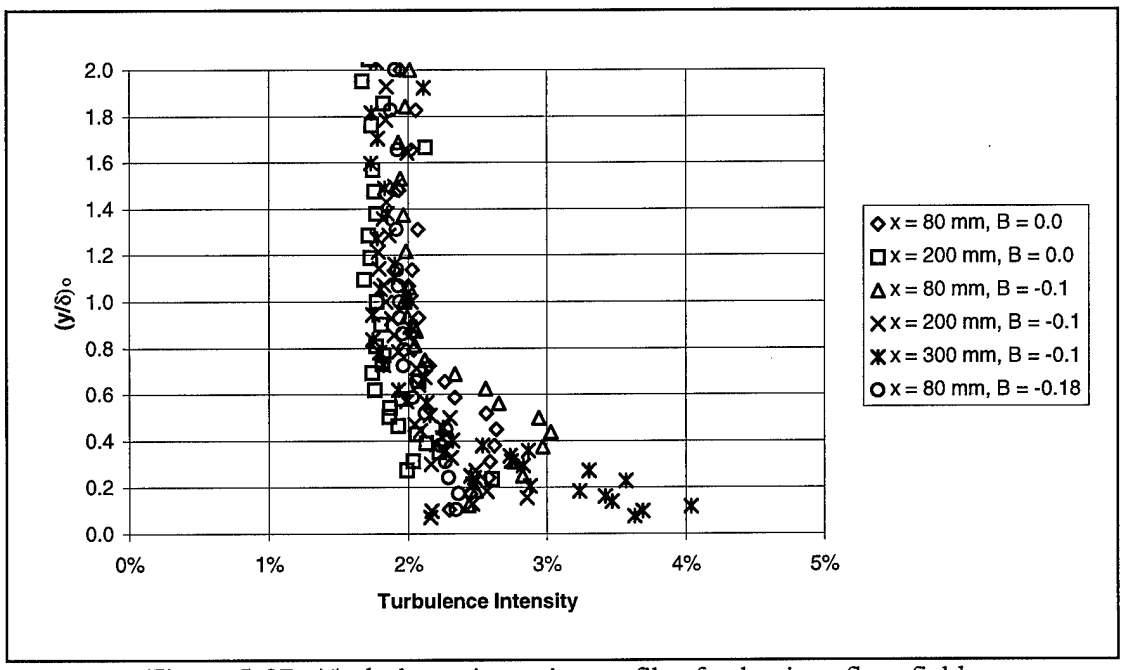

Figure 5-27: Turbulence intensity profiles for laminar flow fields

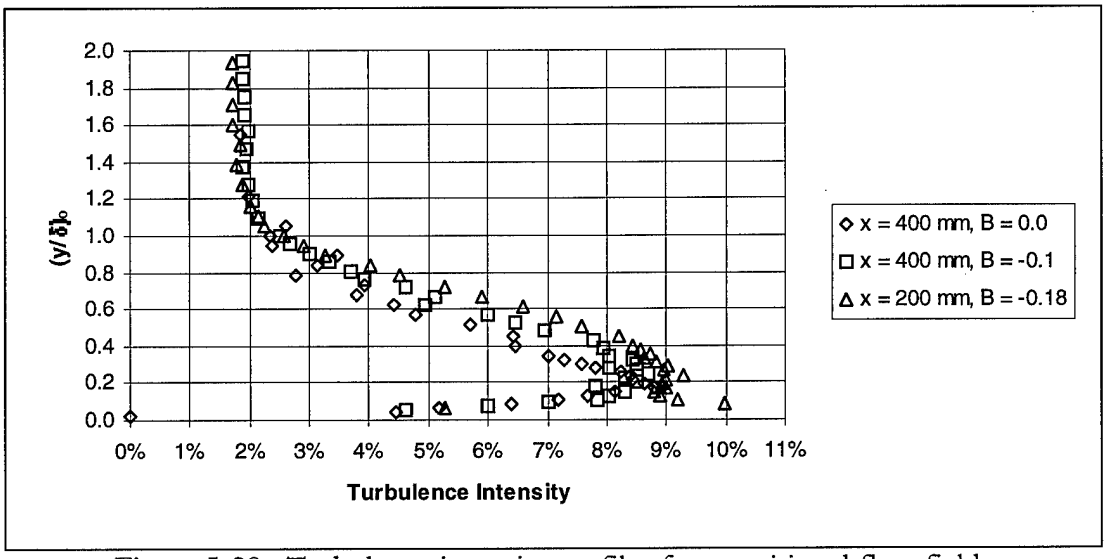

Figure 5-28: Turbulence intensity profiles for transitional flow fields

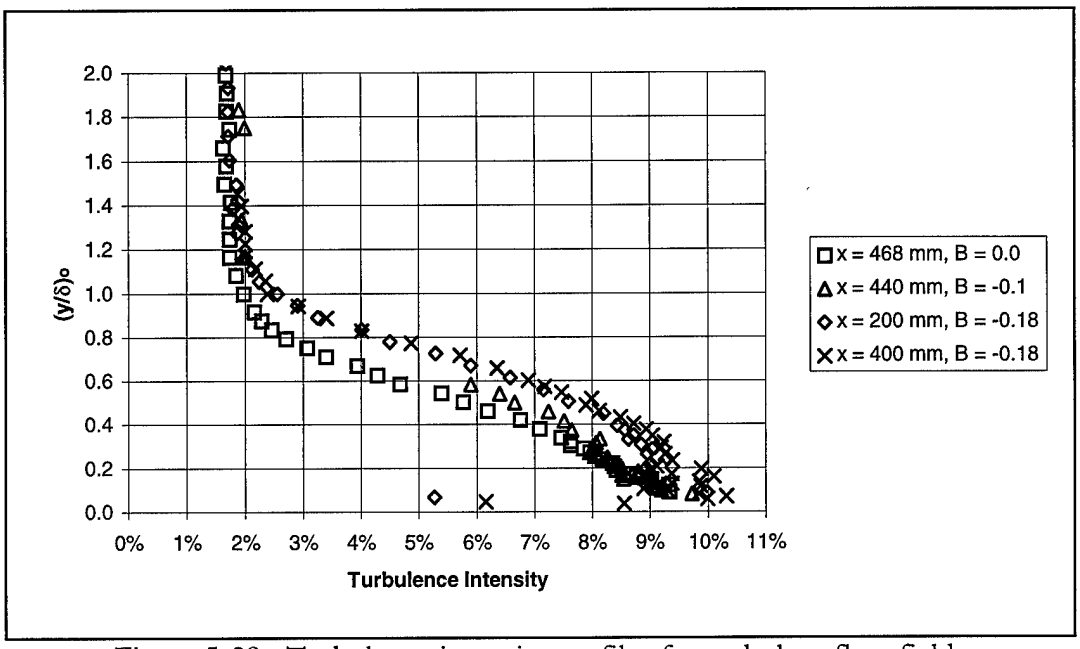

Figure 5-29: Turbulence intensity profiles for turbulent flow fields

All three flow conditions (Figures 5-27 through 5-29) showed the turbulence intensities returning to nominal freestream values slightly below 2%. The peak turbulence levels in the boundary layer were used to help determine the flow field conditions. Table 5-6 provides a summary of peak turbulence intensity values.

Table 5-6: Turbulence intensity (%)

x (mm)	$\beta = 0.0$	$\beta = -0.1$	$\beta = -0.18$
80	2.63	2.94	2.36
200	2.60	2.86	9.00
300		4.04	
400	8.81	8.84	10.32
440		9.72	
468	9.32		

Contour plots of the turbulence intensities in the riblet valley provided further information in the investigation of the turbulence distribution between the riblet peaks. These contours provided accurate values for most of the flow conditions except where large gradients were expected (near a riblet surfaces). The contours near the surfaces exhibit some

variation. This variation was attributed to four main factors; a relatively course measurement grid (0.3 mm spacing), contour lines determined by a linear approximation between points, surface reflections affecting the measured data by the LDA system, and small position errors of the measurement locations (±0.1 mm). The grid spacing was only one order of magnitude less than the riblet spacing (0.3 mm as compared to 3.0 mm). The grid measurements produced good data for points away from the surface but were not as reliable in the higher velocity gradients very near the walls. The linear approximations in these higher gradients will provide appropriate values for the various measured data but will cause the contours near the wall to appear to be shifted into the riblet wall. For data measurements taken very close to the wall (< 0.3 mm), some uncertainty will be introduced due to surface reflections of the laser beams as well. Surface reflections introduce variability in the measured data for the LDA system. Another uncertainty for the measurements taken near the walls included traverse system gear tolerances and slight misalignment when locating the plate surface (±0.1 mm). While these contours appear to intersect the surface, actual values would conform to the wall surface contour.

The flow developed over the riblet plate at a zero pressure gradient began with relatively uniform turbulence intensity between the riblets at x = 80 (Figure 5-30) and 200 mm (Figure 5-31). These laminar flow conditions reflect the slight turbulence increase just above the riblet peaks in the flow and decreased turbulence levels near the surfaces. As the flow became more turbulent along the streamwise direction, the turbulence intensity contours exhibit a uniformly decreasing gradient into the riblet valley. Peak values were still above the peaks for the transitional case (Figure 5-32) but were very close to the peaks for the turbulent flow field (Figure 5-33).

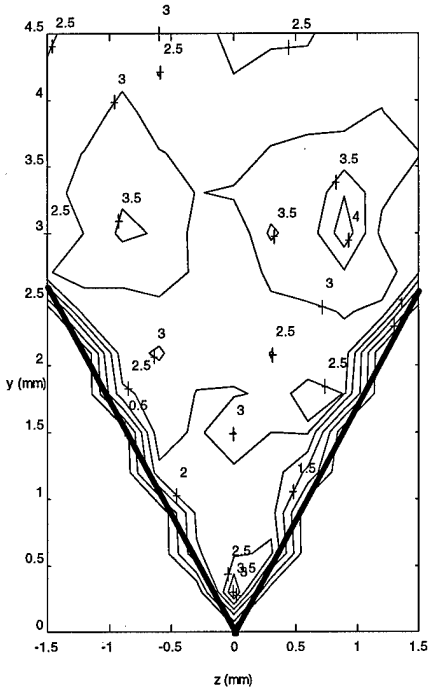

Figure 5-30: Laminar, turbulence intensity (%), x = 80 mm, β = 0.0

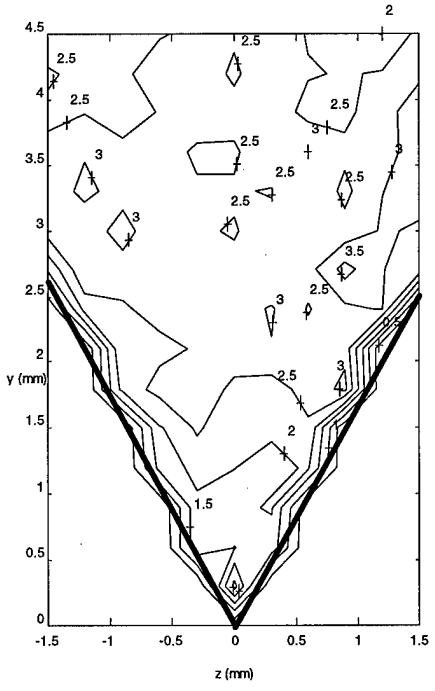

Figure 5-31: Laminar, turbulence intensity (%), x = 200 mm, β = 0.0

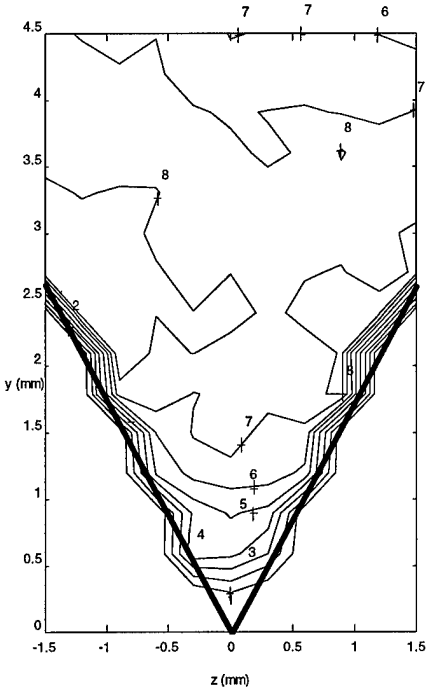

Figure 5-32: Transitional, turbulence intensity (%), x = 400mm, β = 0.0

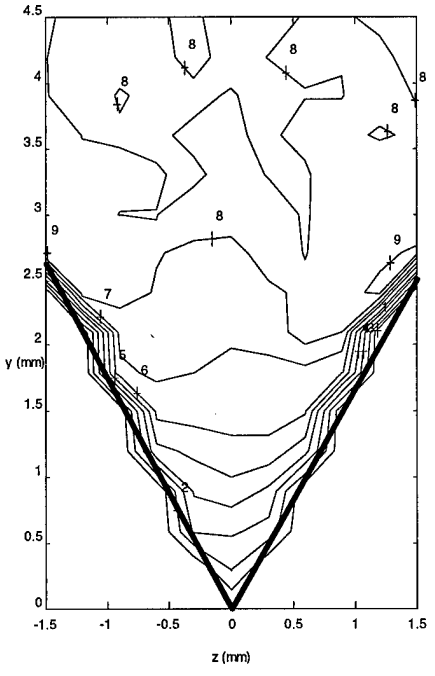

Figure 5-33: Turbulent, turbulence intensity (%), x = 468mm, β = 0.0

The turbulence intensity under the adverse pressure gradient $\beta = -0.1$ showed distributions closer to the leading edge of the test plate to be unchanging throughout the flow field with slight increases just above the riblet peaks. As the turbulence intensity levels increased in the streamwise direction, a more pronounced maximum above the riblet peaks was evident (Figure 5-36). For x = 300 mm and x = 440 mm, the local maximum location moved closer to the riblet peak. Like the zero pressure gradient, more uniform turbulence intensity gradients developed between the riblets with the increase in turbulence. The transitional flow field (Figure 5-37) showed higher levels of turbulence intensity at the riblet peaks (y = 2.6 mm) than for the fully turbulent case (Figure 5-38). With the higher levels of turbulence within the riblet valley, the kinetic energy dissipation would be expected to be higher, thus producing a higher skin friction drag coefficient.

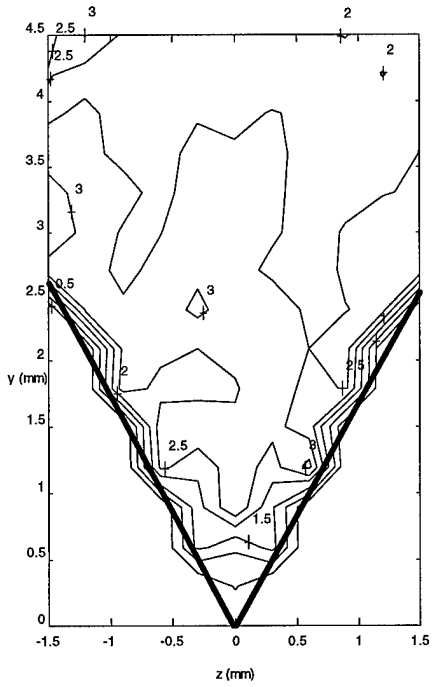

Figure 5-34: Laminar, turbulence intensity (%) x = 80 mm, $\beta = -0.1$

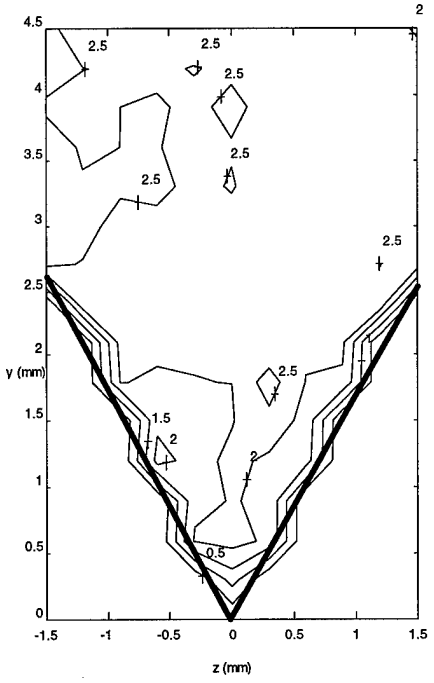

Figure 5-35: Laminar, turbulence intensity (%)x = 200mm, $\beta = -0.1$

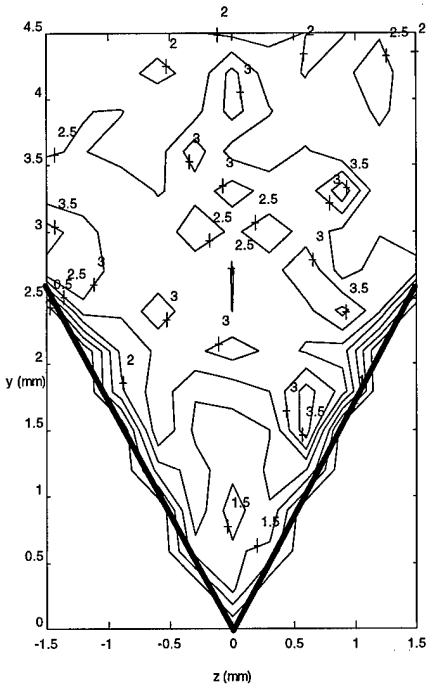

Figure 5-36: Laminar, turbulence intensity (%)x = 300mm, β = -0.1

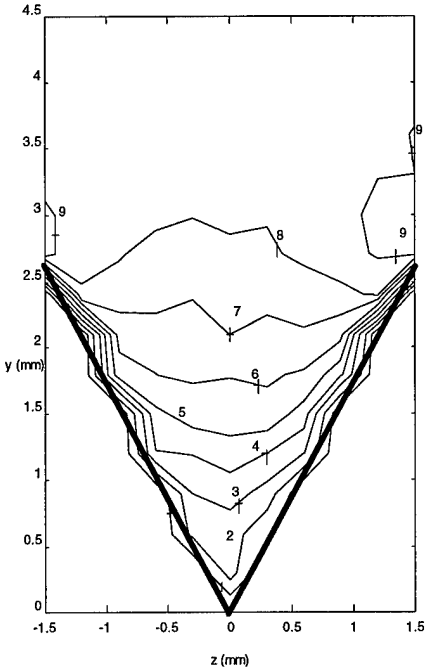

Figure 5-38: Turbulent, turbulence intensity (%), x = 440mm, β = -0.1

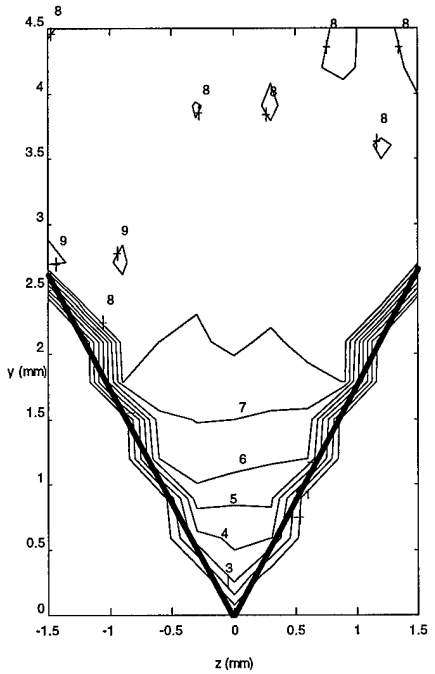

Figure 5-37: Transitional, turbulence intensity (%)x = 400mm, β = -0.1

As the adverse pressure gradient increased to β = -0.18, the turbulence intensity distribution increased in variability as well. The turbulence intensity levels still reduced near the riblet walls. At x = 80 mm (Figure 5-39), turbulence intensities show a peak value just above the riblet peaks. As the turbulence intensity increased under this pressure gradient, variability increased as well. The increased variability results from the randomly occurring vortex motion being formed on the riblet surfaces. These vortex formations have a time varying character. For x = 400, β = -0.18 (Figure 5-41) the maximum turbulence intensity appears to be slightly inside the valley between the riblet peaks. With the higher levels of turbulence inside the riblet valley, the skin friction would be higher for this case.

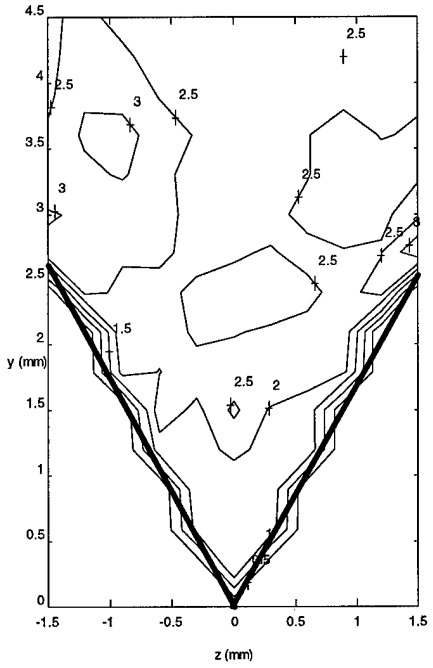

Figure 5-39: Laminar, turbulence intensity (%) x = 80mm, β = -0.18

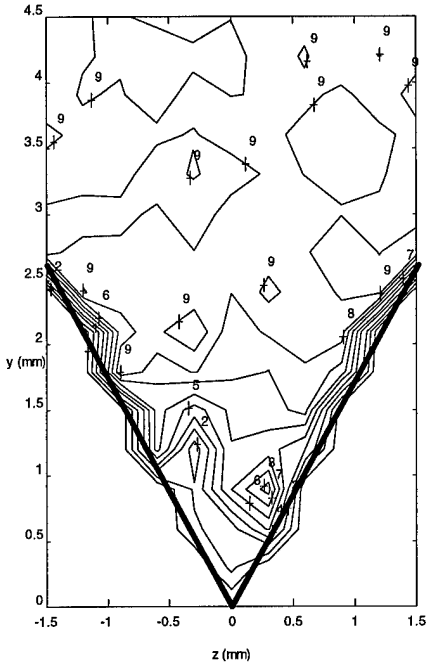

Figure 5-40: Turbulent, turbulence intensity (%)x = 200mm, β = -0.18

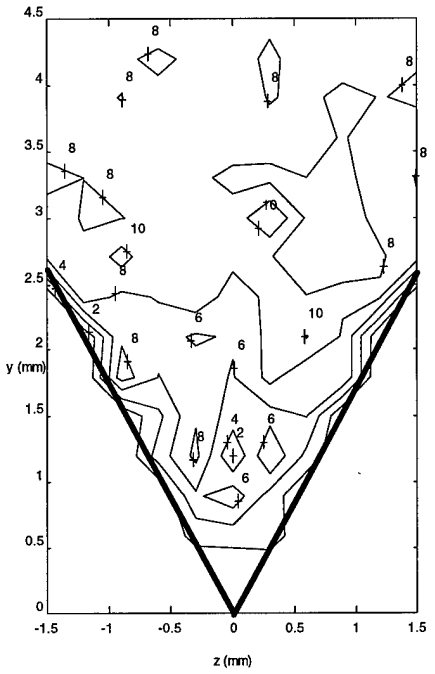

Figure 5-41: Turbulent, turbulence intensity (%) x = 400mm, β = -0.18

5.6 Development of the Reynolds Stress in the Riblet Valley

The Reynolds stress was a measure of the turbulence shearing (White, 1990). Shift in the Reynolds stresses, primarily u'v', indicate shifts in the average production of turbulent kinetic energy which affect energy production and dissipation rates.

With the flow field being oriented along the riblets, the most significant velocities are the streamwise (u) and normal (v) components. Variations and changes in these velocities are directly related to the Reynolds stress characterized by the u'v' component. This component provides an indication of the most significant amount of kinetic energy being dissipated in the flow characterized by the Reynolds stress. Figures 5-42 through 5-53 provide contour maps of this flow parameter plotted as average values normalized by the freestream velocity (<u'v'> indicates average values). This statistic typically provides a negative value to indicate an increase in skin friction. Increases in the Reynolds stress were considered increases in

magnitude. The effect of the Reynolds stress on skin friction drag can be seen in the two dimensional boundary layer relationship in Equation 5-4 (White, 1991). A more negative Reynolds stress would indicate an increase in skin friction drag.

$$\tau = \mu \frac{du}{dy} - \rho \overline{u'v'} \tag{5-4}$$

The contours near the surfaces exhibit variations similar to those seen in the turbulence intensity contour plots. For this reason, the explanation for the variations is being repeated here. This variation was attributed to four main factors; a relatively course measurement grid (0.3 mm spacing), contour lines determined by a linear approximation between points, surface reflections affecting the measured data, and small position errors of the measurement locations (±0.1 mm). The grid spacing was only one order of magnitude less than the riblet spacing (0.3 mm as compared to 3.0 mm) The grid measurements produced good data for points away from the surface but were not as reliable in the higher velocity gradients near the walls. The linear approximations in these higher gradients will provide appropriate values for the various measured data but will cause the contour near the wall to be shifted into the riblet wall. For data measurements taken very close to the wall (< 0.3 mm), some uncertainty will be introduced due to surface reflections of the laser beams as well. Added to this, the established position of the measurement point included uncertainty due to the traverse system gear tolerances and slight positioning misalignment (±0.1 mm).

The flow conditions for a zero pressure gradient increased values of Reynolds stress ($<u'v'>/U^2$) from -2.0E-5 at x = 80 mm to -3.0E-3 at x = 468 mm. For the laminar flow case at x = 80 mm (Figure 5-42), the Reynolds stress values show considerable variability over a small range of values. For a fully laminar flow condition, the Reynolds stress would

be zero. The flow conditions for this investigation, though, were not completely laminar. These flow fields contained some level of random fluid motion but were relatively uniform. At x = 200 mm (Figure 5-43), the same variability is exhibited but at a range slightly higher than at x = 80 mm. The transitional flow field (Figure 5-44) showed a slightly different pattern. Local maximum values occurred just above the peaks of the riblets. The values decreased deeper into the valley. For the fully turbulent flow field (Figure 5-45), the same trends were evident but more pronounced. Along the ribletted plate, values for the Reynolds stress increased with increasing turbulence. Also, local maximums developed above the riblet peaks and a decreasing gradient into the riblet valley and toward the riblet surfaces evolved.

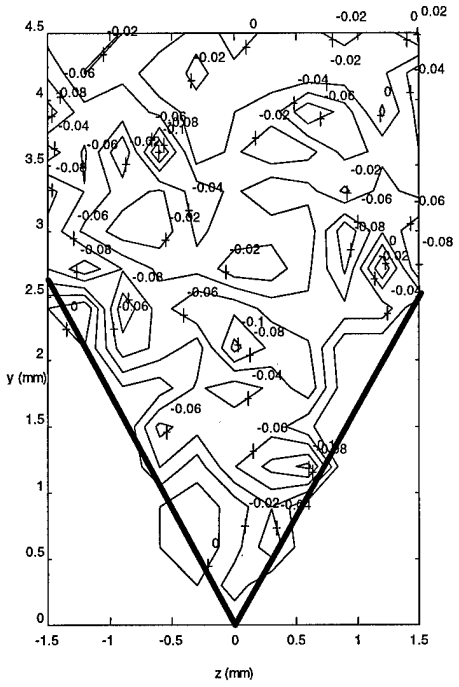

Figure 5-42: Laminar, $\langle u'v' \rangle / U^2 x 10^3$, x = 80 mm, β = 0.0

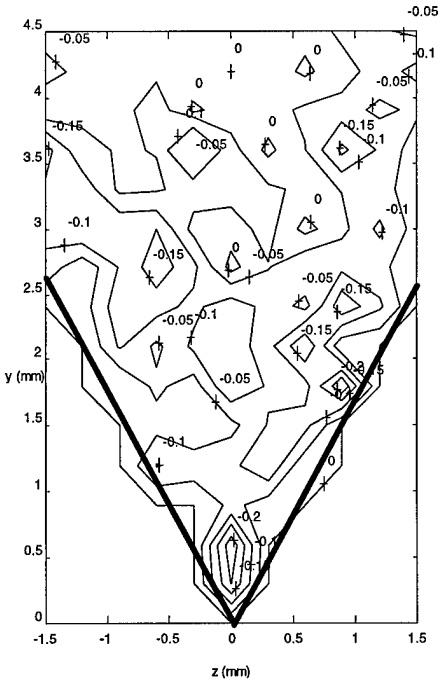

Figure 5-43: Laminar, $\langle u'v' \rangle / U^2 x 10^3$, x = 200 mm, β = 0.0

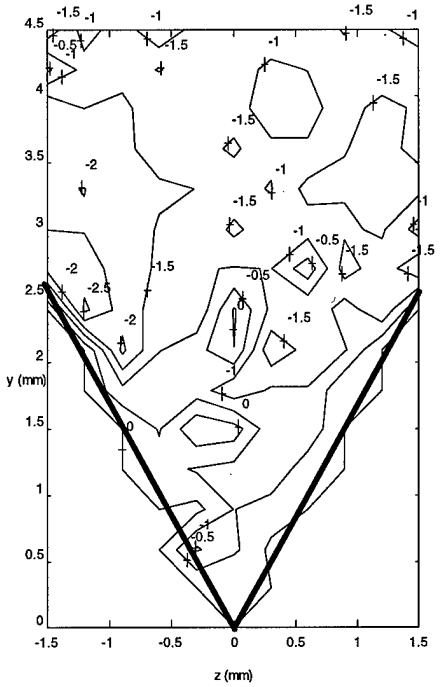

Figure 5-44: Transitional, $\langle u'v' \rangle / U^2 x 10^3$, x = 400 mm, β = 0.0

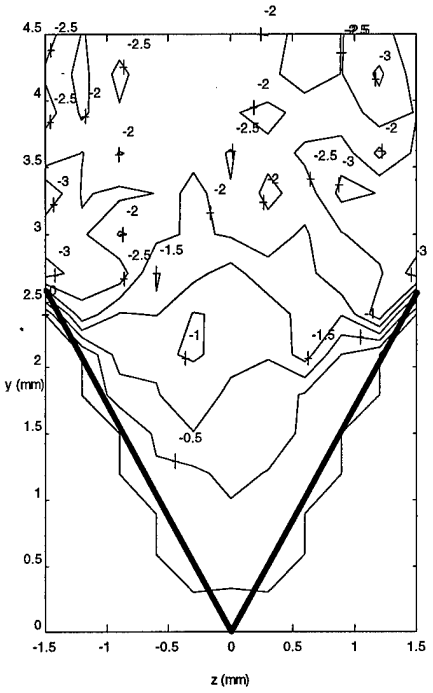

Figure 5-45: Turbulent, $\langle u'v' \rangle / U^2 x 10^3$, x = 468 mm, β = 0.0

For the adverse pressure gradient β = -0.1, similar results were present. The laminar flow fields (Figures 5-46 through 5-48) showed significant randomness over a small range for a relatively low value of the Reynolds stress. With an increasing streamwise location (and turbulence intensity) the magnitude of these Reynolds stresses increased. As the flow fields became more turbulent (transitional and turbulent states), the local maximum near the riblet peaks was evident as well as a decreasing gradient into the valley (Figures 5-49 and 5-50). Again, higher turbulence levels also indicated higher Reynolds stress values. The stress values and patterns appear to be affected very little by the pressure gradient difference for this case.

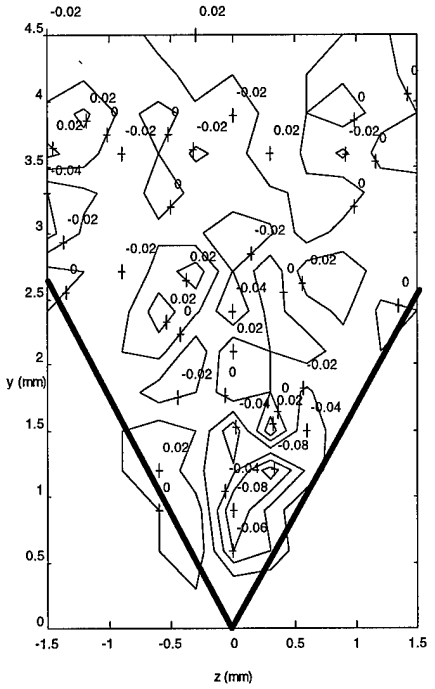

Figure 5-46: Laminar, $\langle u'v' \rangle / U^2 x 10^3$, x = 80 mm, β = -0.1

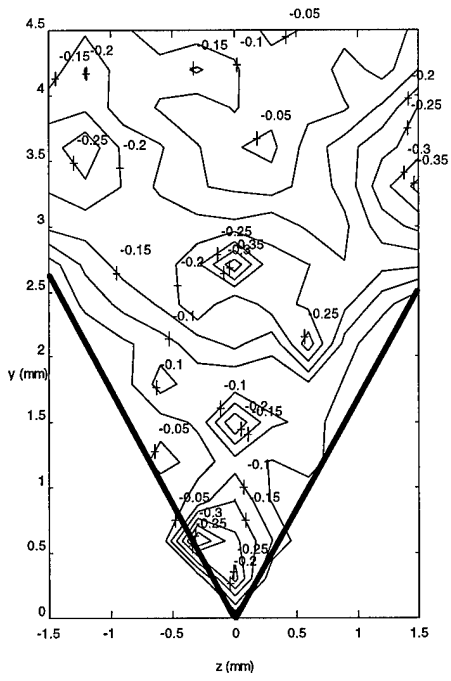

Figure 5-47: Laminar, $\langle u'v' \rangle / U^2 x 10^3$, x = 200 mm, β = -0.1

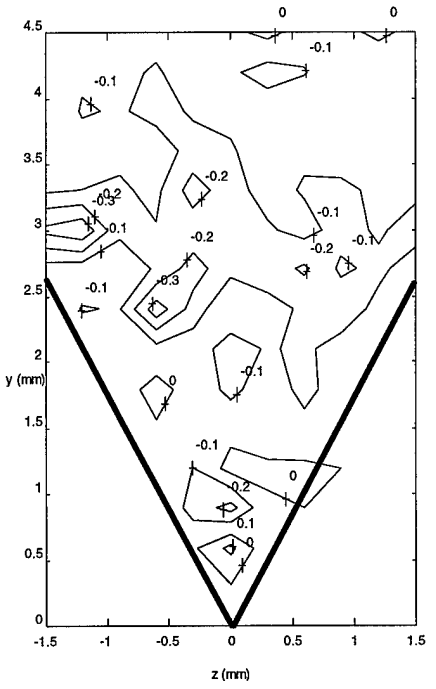

Figure 5-48: Laminar, $\langle u'v' \rangle / U^2 x 10^3$, x = 300 mm, β = -0.1

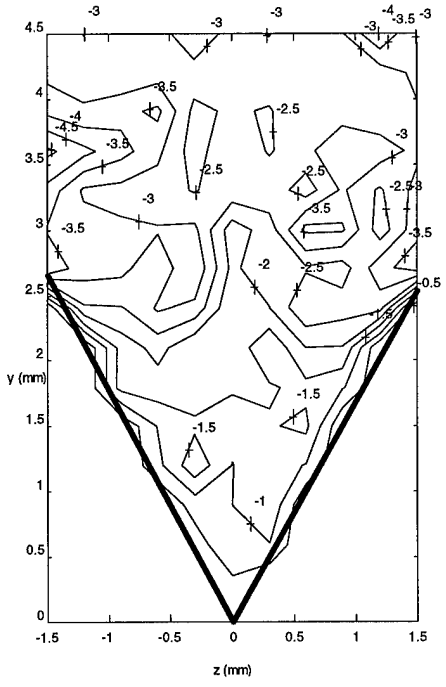

Figure 5-49: Transitional, $\langle u'v' \rangle / U^2 x 10^3$, x = 400 mm, β = -0.1

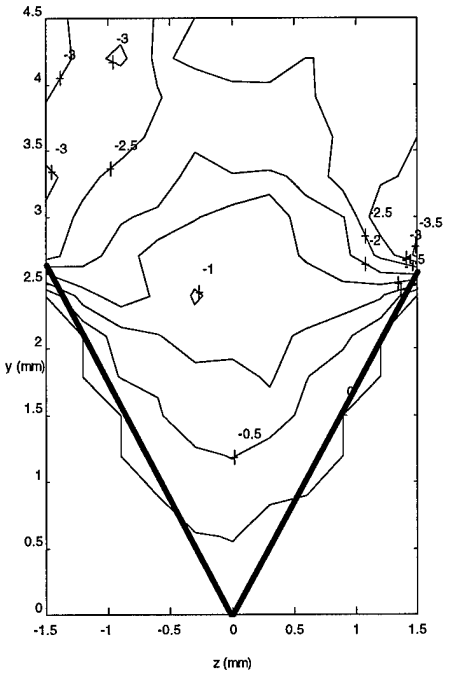

Figure 5-50: Turbulent, $\langle u'v' \rangle / U^2 x 10^3$,
x = 440 mm, β = -0.1

Increasing the pressure gradient to β = -0.18 produced significant differences in the Reynolds stress. The laminar flow field appeared fairly random but at higher Reynolds stress levels than for lower pressure gradient conditions and there was evidence of local maximum values near the riblet peaks (Figure 5-51). At x = 200 mm (Figure 5-52), the Reynolds stress was significantly higher than at x = 80 with maximum values occurring at the riblet peaks. As the turbulence level increased at this pressure gradient, the Reynolds stress appeared more random with increases near the riblet peaks (Figure 5-53). A local maximum also appeared just above the mid-plane in the valley near z = 0. This location for the maximum Reynolds stress suggests increased skin friction drag in the valley of the riblets for this pressure gradient. With the local maximum above the mid-plane, energy dissipation deep in the valley would be lower.

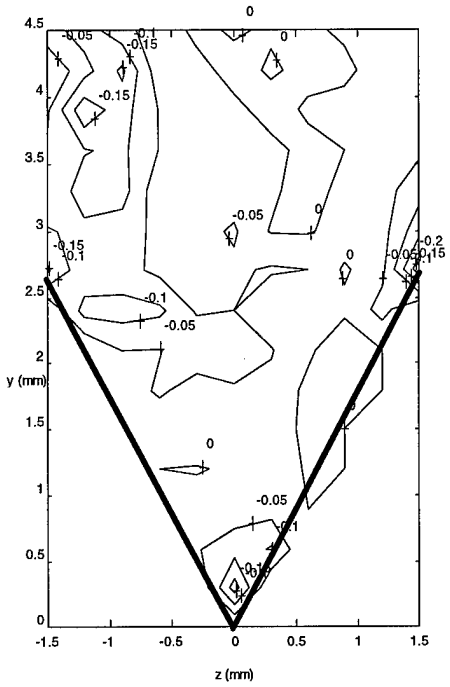

Figure 5-51: Laminar, $\langle u'v' \rangle / U^2 x 10^3$, x = 80 mm, β = -0.18

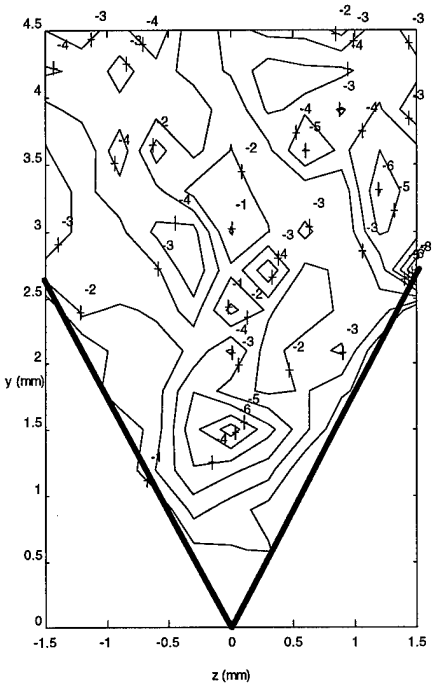

Figure 5-53: Turbulent, $\langle u'v' \rangle / U^2 x 10^3$, x = 400mm, β = -0.18

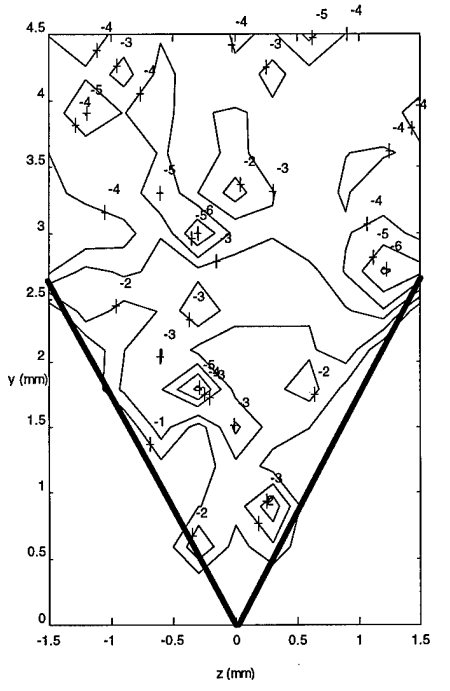

Figure 5-52: Turbulent, $\langle u'v' \rangle / U^2 x 10^3$, x = 200mm, β = -0.18

As the pressure gradient increased, the Reynolds stress values increased slightly as well. The development of the Reynolds stress along the streamwise direction changed with the large change in adverse pressure gradient as seen in the figures for β = -0.18. For zero pressure gradient and β = -0.1, the stress developed from a low, random distribution (laminar) to a pattern with increases near the riblet peaks and a decreasing gradient into the riblet valley. At β = -0.18, the pattern at the higher turbulence levels showed higher levels of randomness with an increasing gradient into the valley.

With the transitional and turbulent (high level of turbulence intensity) flow fields exhibiting increased values near the riblet peaks, the stress levels at the peaks would be higher than at other locations along the riblet surface. The decreasing gradient in the valley suggests for zero and mild adverse gradients, the energy dissipation in the valley was less.

5.7 Development of the Skewness in the Riblet Valley

Skewness (third moment of velocity) provided further information about the flow characteristics over the ribletted surface. Skewness is a measure of variations from the mean local velocity value. The contour maps are for the streamwise component and have been normalized by the freestream velocity. The skewness along with flatness in the next section provided information on the dissipation and production of kinetic energy. Higher values of skewness indicate the local velocity has values below the average value for much of the time with excursions to values high above the mean velocity. This information about the time varying character of the flow field indicated the magnitude of the higher momentum fluctuations seen at a location in the flow. When considering skewness alone, large values indicate areas of locally increased dissipation of energy and an increase in drag.

The contours near the surfaces exhibit variations similar to those seen in the turbulence intensity contour plots. Once again, the explanation for the variations is being repeated here. This variation was attributed to four main factors; a relatively course measurement grid (0.3 mm spacing), contour lines determined by a linear approximation between points, surface reflections affecting the measured data, and position uncertainty (±0.1 mm). The grid spacing was one order of magnitude smaller than the size of the riblets (0.3 mm as compared to 3.0 mm). These grid measurements produced good data for points away from the surface but were not as reliable in the higher velocity gradients near the walls. The linear approximations in these high gradient regions provided approximate values for the various measured data but caused the contour near the wall to appear to be shifted into the riblet wall. For data measurements taken very close to the wall (< 0.3 mm), some uncertainty will be introduced due to surface reflections of the laser beams as well. Added to this, the position of the measurement point for the LDA system included error due to the traverse system gear tolerances and slight position misalignment (±0.1 mm).

Skewness trends were seen for both increases in flow turbulence intensity and increases in adverse pressure gradient. As the flow turbulence intensity increased (flow fields from laminar to transitional to turbulent), skewness maximums moved from locations above the mid-plane to slightly below the mid-plane. The fact that the maximum skewness was below the mid-plane for turbulent flow fields suggests the instantaneous velocity remained less than the local, mean value with spikes to higher values. As the pressure gradient increased, the magnitude of the skewness for turbulent flow fields showed little change suggesting the riblets maintain drag reducing capability under an adverse pressure gradient.

The flow developing over the ribletted plate for a zero pressure gradient (Figures 5-54 through 5-57) showed three major trends; increased skewness in the valleys for all flow conditions, increasing gradient near the riblet surfaces with increasing turbulence intensity, and maximum values moving from above to below the mid-plane of the riblets (y = 1.3 mm). The laminar flow condition at x = 80 mm (Figure 5-54) showed a very random pattern with only slight increases in the valley. As the flow developed in the laminar regime, (x = 200 mm), the increase in the valley was more significant (Figure 5-55) with largest values occurring slightly above the mid-plane. As the turbulence intensity increased along the streamwise direction, an increasing skewness gradient was present. The transitional flow condition (Figure 5-56) showed the increasing skewness gradient into the riblet valley with maximums just below the mid-plane of the riblets. These maximums appeared further below the mid-plane for the turbulent flow condition (Figure 5-57).

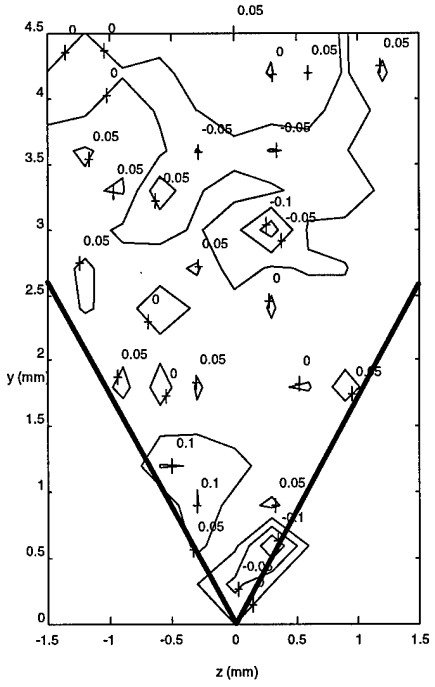

Figure 5-54: Laminar, Skewness/U, x = 80 mm, β = 0.0

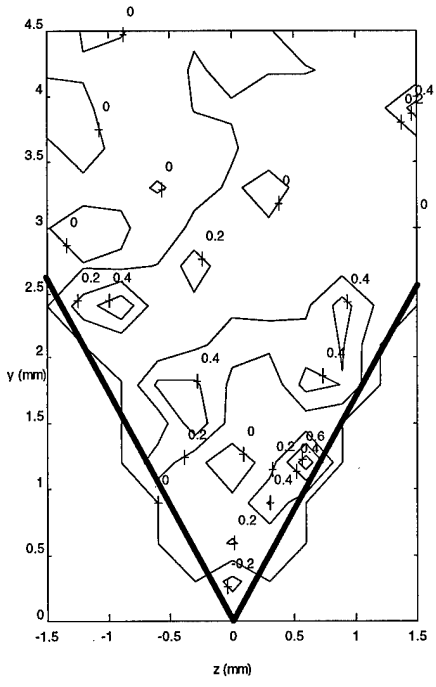

Figure 5-55: Laminar, Skewness/U, x = 200 mm,β = 0.0

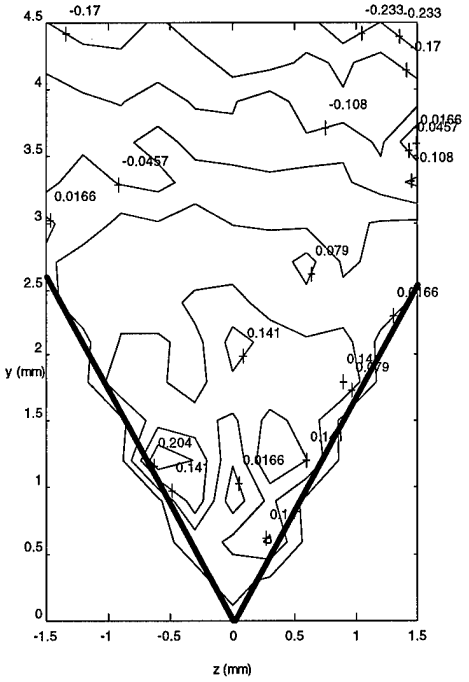

Figure 5-56: Transitional, Skewness/U, x = 400 mm, β = 0.0

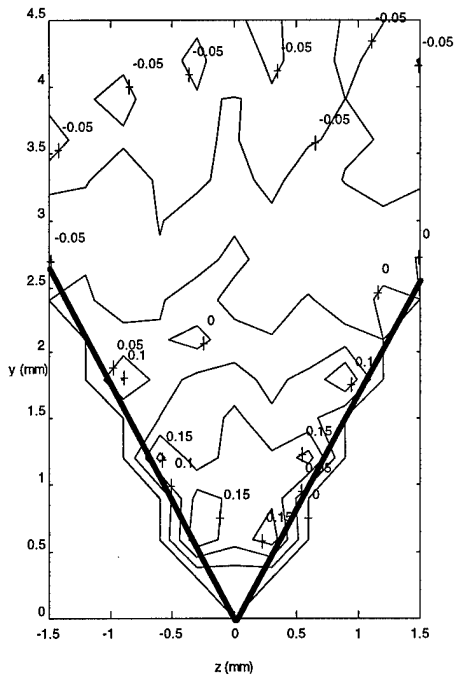

Figure 5-57: Turbulent, Skewness/U, x = 468 mm, β = 0.0

The trends seen for the zero pressure gradient were still present when the adverse pressure gradient was increased to β = -0.1. The laminar flow fields (Figures 5-58 through 5-60) showed the increasing skewness into the riblet valley with higher values at and above the riblet mid-plane. Figure 5-58 (x = 80 mm) shows very pronounced maximum values occurring near the surface just above the mid-plane. At x = 300 mm and 400 mm, the skewness values appear to have more gradual gradients with higher values deeper into the valley (Figures 5-60 and 5-61). As the flow becomes more turbulent (Figure 5-62), maximum skewness appears just below the mid-plane.

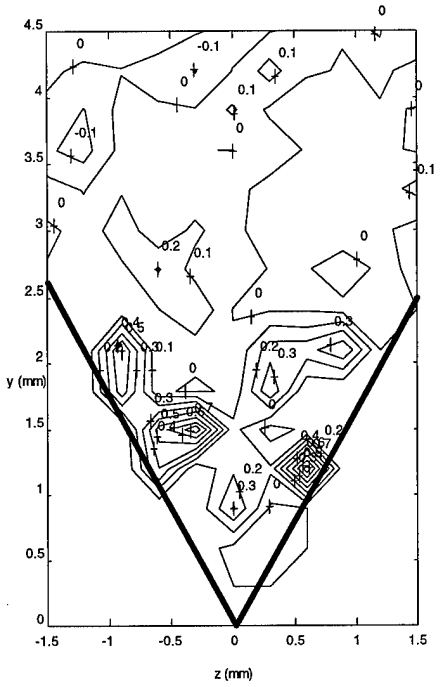

Figure 5-58: Laminar, Skewness/U, x = 80 mm, β = -0.1

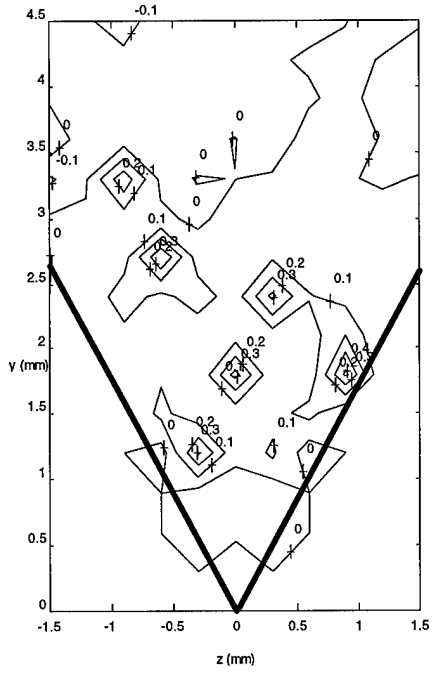

Figure 5-59: Laminar, Skewness/U, x = 200 mm, β = -0.1

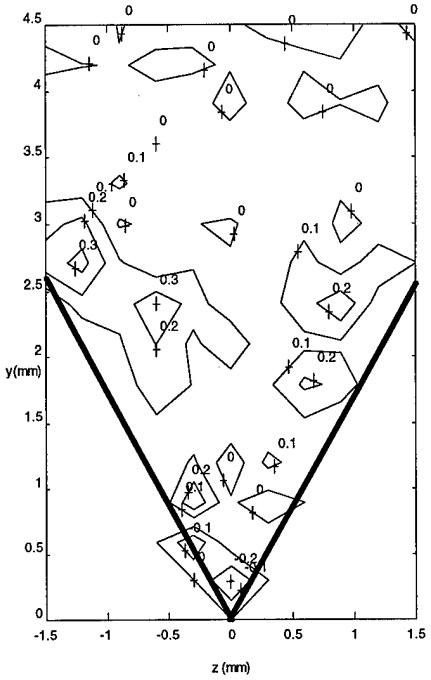

Figure 5-60: Laminar, Skewness/U, x = 300 mm, b = -0.1

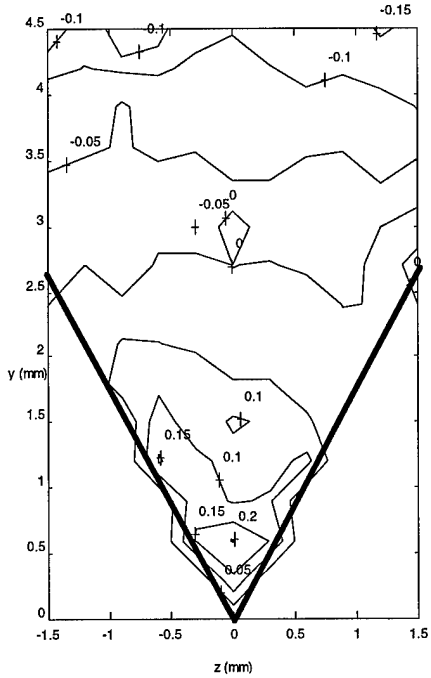

Figure 5-61: Transitional, Skewness/U, x = 400 mm, β = -0.1

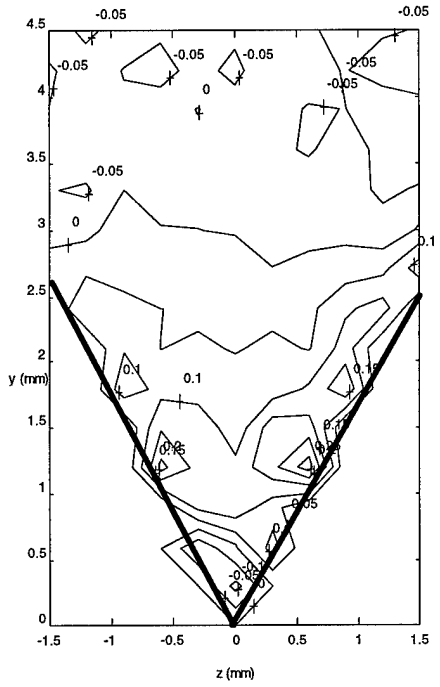

Figure 5-62: Turbulent, Skewness/U, x = 440 mm, β = -0.1

The local maximums for the laminar flow case appeared above the mid-plane and along the surface for the adverse pressure gradient of β = -0.18 as well (Figure 5-63). The skewness gradients were the highest near the walls with only a slight increase in the valley everywhere else. The transition to turbulent flow (Figure 5-64) produced a much higher gradient of the skewness into the valley. The maximum values appeared at and below the mid-plane. For the highly turbulent case (Figure 5-65), the flow field exhibited skewness contours with uniform values throughout the area between the peaks. This suggested the flow field was well developed with infrequent variations to large values above the local, average velocity and relatively constant energy dissipation throughout the flow field.

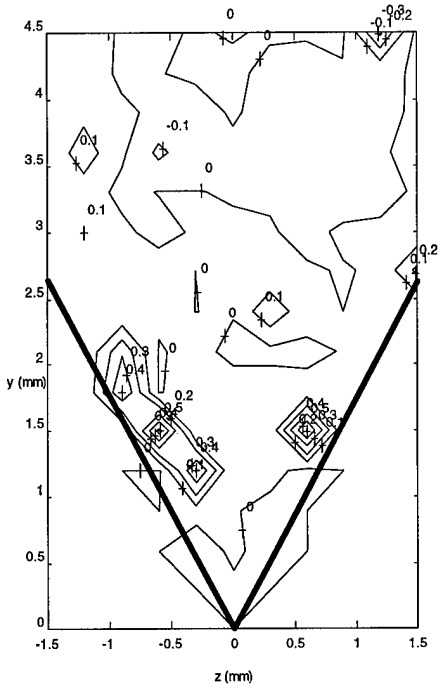

Figure 5-63: Laminar, Skewness/U, x = 80 mm, β = -0.18

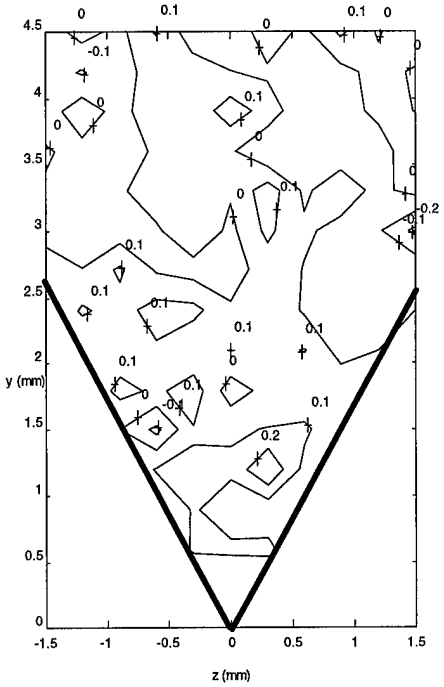

Figure 5-65: Turbulent, Skewness/U, x = 400 mm, β = -0.18

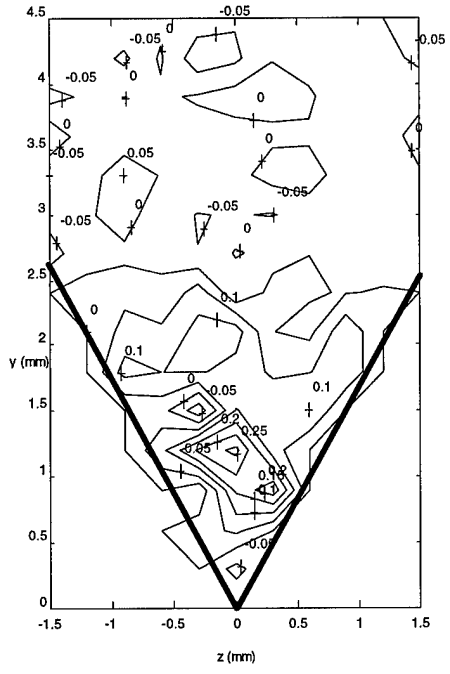

Figure 5-64: Turbulent, Skewness/U, x = 200 mm, β = -0.18

The skewness factors for the laminar flow conditions were higher in magnitude for the turbulent flow conditions at each pressure gradient condition. The higher values indicated the higher level of kinetic energy dissipation for the laminar flow fields over the riblets. The contours at the same streamwise location (x = 80, Figures 5-54, 5-58, 5-63), the largest skewness values near the riblet surfaces were above the mid-plane of the riblet height. As the adverse pressure gradient increased, the maximum values appeared to remain about the same location (x = 80 mm, β = -0.1 and x = 80 mm, β = -0.18).

The transitional flow fields showed similar results with only slight variations; increasing skewness near the riblet surfaces and increased skewness near the riblet mid-plane. These transitional flow fields had the increased values of skewness appearing near the mid-plane (Figures 5-56 and 5-61), lower in the riblet valley than for the laminar cases.

Skewness parameters in the turbulent flow fields showed a significant trend; increased values closer to the riblet surfaces and near the mid-plane in the valley. The highest values appeared near or slightly below the mid-plane close to the wall (Figures 5-57, 5-61 and 5-65). The magnitude for the skewness values appeared to be unaffected by the increased pressure gradient for turbulent flow, suggesting the same level of energy dissipation in the turbulent flow fields with increased pressure gradient.

5.8 Development of the Flatness in the Riblet Valley

Flatness (fourth moment of velocity) provided further information about the flow characteristics over the ribletted surface. Flatness provides information about the frequency of large variations of velocity from the local, mean value. These streamwise flatness contours were normalized by the freestream velocity. The flatness properties provided insight into the dissipation and production of kinetic energy in the boundary layer. Large

values of flatness indicated locally increased dissipation of kinetic energy and an increased skin friction.

The contours for flatness near the surfaces exhibit the same variations seen in the turbulence intensity, Reynolds stress and skewness contour plots. This variation was attributed to four main factors; a relatively course measurement grid (0.3 mm spacing), contour lines determined by a linear approximation between points, surface reflections affecting the measured LDA data, and small position uncertainties of the measurement locations (±0.1 mm). The grid spacing was one order of magnitude smaller than the riblet spacing (0.3 mm as compared to 3.0 mm). These measurements produced good data for points away from the surface but were not as reliable in the higher velocity gradients near the walls. The linear approximations in the higher gradients provided appropriate values for the various measured data but caused the contour near the wall to appear to be shifted into the riblet wall. For data measurements taken very close to the wall (< 0.3 mm), some uncertainty will be introduced due to surface reflections of the laser beams as well. Added to this, the position of the measurement point included uncertainty due to the traverse system gear tolerances and slight misalignment when locating the plate surface (±0.1 mm).

The trend seen for the laminar flow fields (Figures 5-66 and 5-67) at zero pressure gradient included a large gradient near the riblet surfaces. As the turbulence intensity increased (in the streamwise direction), the flatness increased for transitional flow but was slightly less in the fully turbulent case. Figure 5-69 suggests the flow in the fully turbulent flow field contains less time dependency. The turbulent flow state also shows a slight increase in flatness values below the mid-plane of the riblet height.

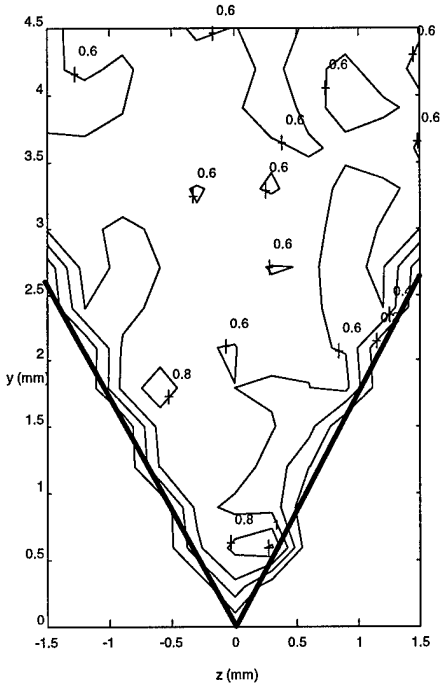

Figure 5-66: Laminar, Flatness/U, x = 80 mm, $\beta = 0.0$

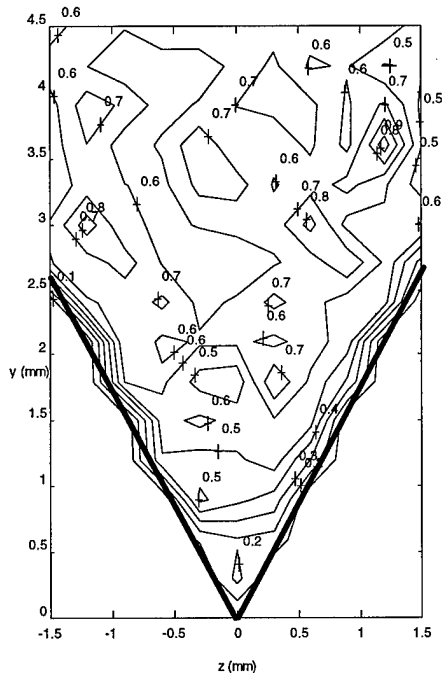

Figure 5-67: Laminar, Flatness/U, x = 200 mm, $\beta = 0.0$

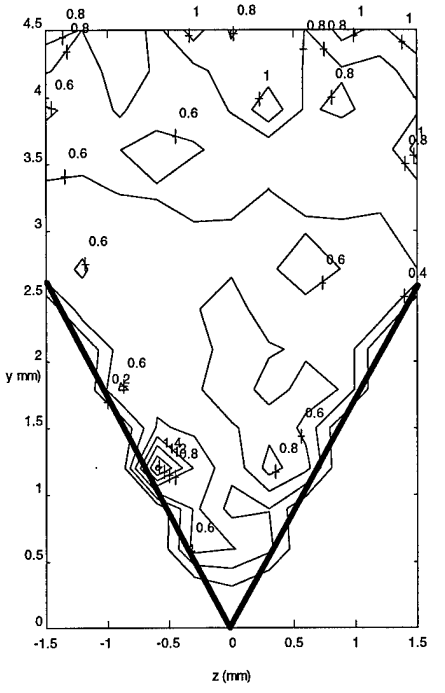

Figure 5-68: Transitional, Flatness/U, x = 400 mm, $\beta = 0.0$

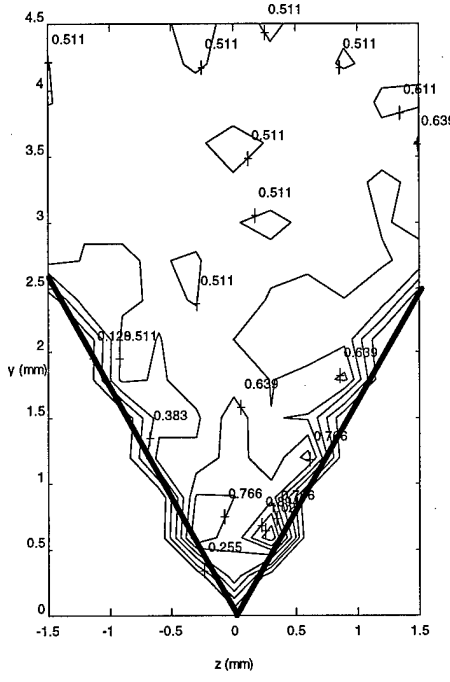

Figure 5-69: Turbulent, Flatness/U, x = 468 mm, $\beta = 0.0$

For the adverse pressure gradient flow condition established for β = -0.1 conditions, the laminar flow fields show fairly uniform flatness factors above the riblets (Figures 5-71 and 5-72). At x = 80 mm (Figure 5-70), the flow above the riblets shows some increased flatness. These flow conditions show the largest values to be above the mid-plane of the riblet height and near the walls. The transitional flow field (Figure 5-73) for this pressure gradient exhibits large gradients near the surface with a slight increase below the mid-plane. Elsewhere in the flow, the value tends to be relatively uniform suggesting less time dependence on the variations from the local, mean velocity. The turbulent flow field (Figure 5-74) exhibited similar results with a local maximum occurring near the mid-plane.

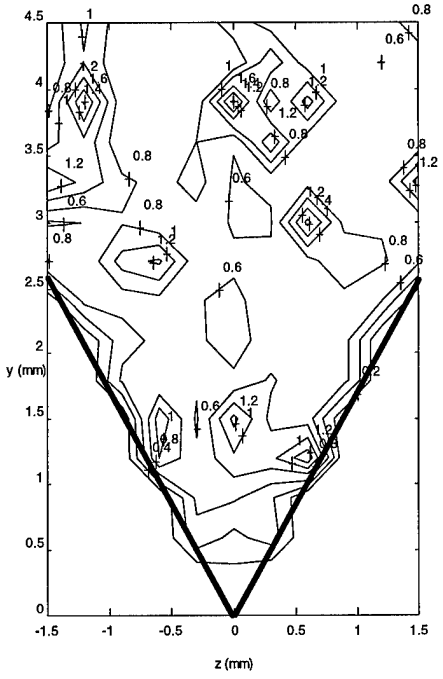

Figure 5-70: Laminar, Flatness/U, x = 80 mm, β = -0.1

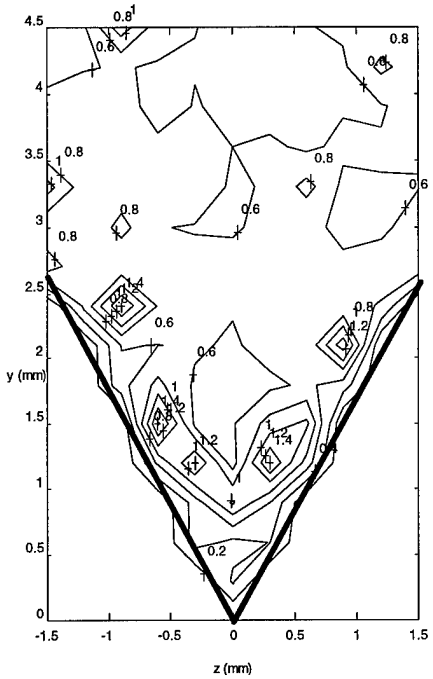

Figure 5-71: Laminar, Flatness/U, x = 200 mm, β = -0.1

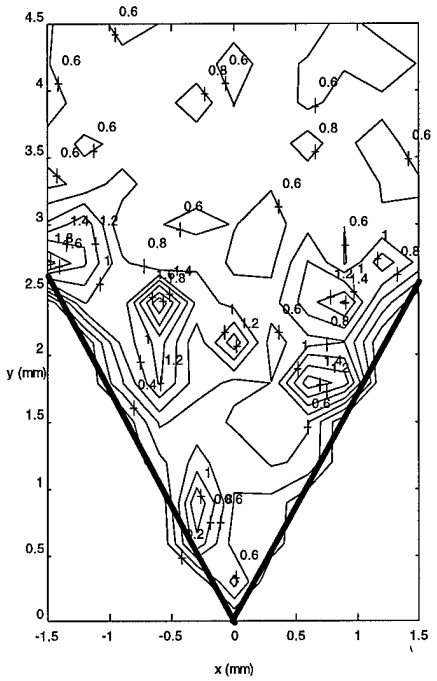

Figure 5-72: Laminar, Flatness/U, x = 300 mm, β = -0.1

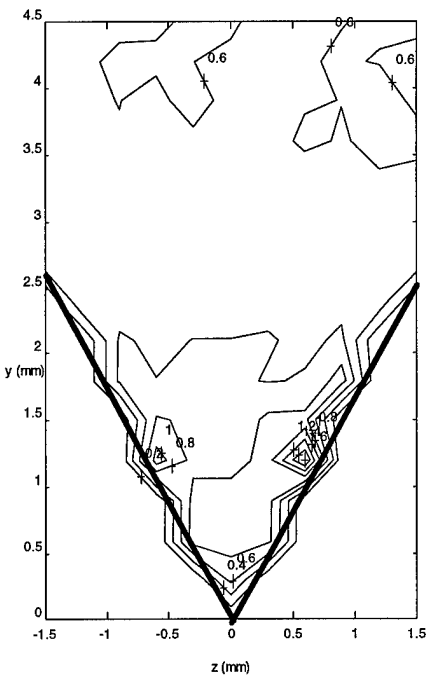

Figure 5-74: Turbulent, Flatness/U, x = 440 mm, β = -0.1

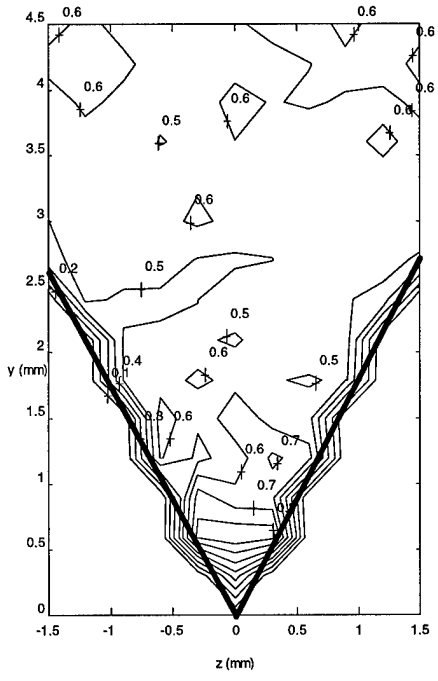

Figure 5-73: Transitional, Flatness/U, x = 400 mm, β = -0.1

The most severe pressure gradient (β = -0.18) showed uniform values for the flatness factor in the laminar flow regime (Figure 5-75). A flatness gradient along the surfaces was present for the length of the test section. At x = 200 mm (Figure 5-76), the gradient also occurred below the mid-plane. Figure 5-77 showed the same gradient pattern for the flatness factor. Largest values of flatness for this pressure gradient condition appeared very near the surfaces of the riblets.

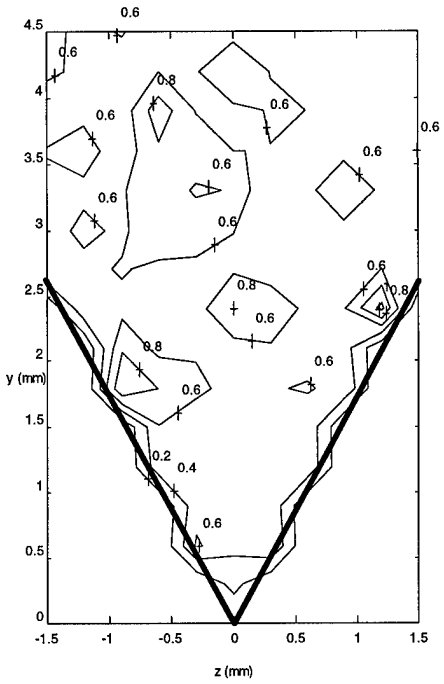

Figure 5-75: Laminar, Flatness/U, x = 80 mm, β = -0.18

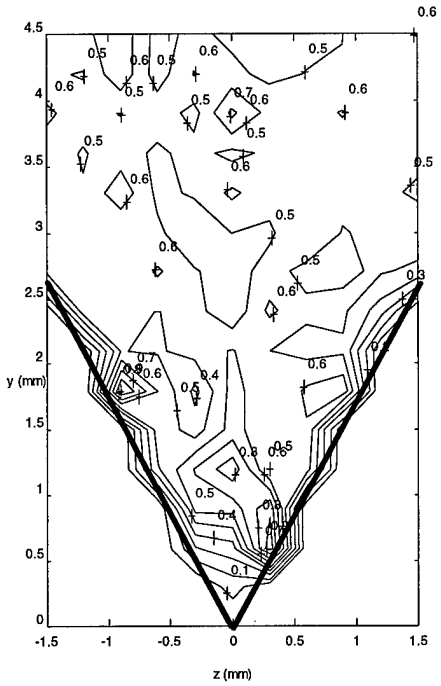

Figure 5-76: Turbulent, Flatness/U, x = 200mm, β =-0.18

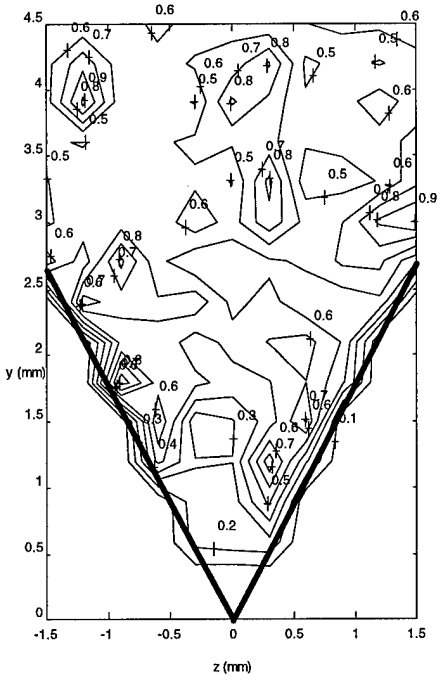

Figure 5-77: Turbulent, Flatness/U, x = 400 mm, β = -0.18

The flatness maximums appeared to be just above the mid-plane for laminar flow and at the mid-plane for both the transitional and turbulent flow conditions. The magnitude of the flatness factors did not seem to be affected by the increase in the adverse pressure gradient. The small changes in magnitude to the flatness factor as the adverse pressure gradient increased suggests the ribletted plate retains the drag reducing ability under an adverse pressure gradient.

5.9 Development of the Vorticity in the Riblet Valley

Suzuki and Kasagi (1994) showed the existence of secondary flow structures over a ribletted plate. Of particular interest is the pair of vortices between the riblet peaks as characterized by the velocity vector composed of the normal (v) and spanwise (w) velocity components. The vortex motion between the peaks caused the higher momentum fluid to penetrate deeper into the riblet valley. By forcing the higher momentum flow closer to the

riblet surface, more energy would be dissipated by skin friction and the ribletted plate would be causing a drag augmenting condition over similar flow conditions for a flat plate.

For a zero pressure gradient, the flow was considered laminar until 350 mm from the leading edge. The largest velocity component for this flow state (Figures 5-78 and 5-79) was the normal velocity component. The flow was expected to be uniform for the laminar case with only slight spanwise velocity due to the low level of turbulence intensity experienced for this investigation. With increasing turbulence intensity, the flow field became more random (Figure 5-80). In this flow state, time dependent vortices were being shed from the riblet surfaces at a random interval. Figure 5-80 exhibits this by the low magnitude v-w vectors. This figure was plotted as an ensemble average of the local velocity values for each measurement point. The averaging removed any time dependence characteristics and reduced the velocity values toward zero. As the flow continued developing into the fully turbulent regime (Figure 5-81), the vortices shedding from the riblet surfaces produced a time-averaged flow structure resembling a pair of counter-rotating vortices between the riblet peaks. Figure 5-81 shows these vortices to be centered near $y = 2.7 \pm 0.2$mm and 0.7 ± 0.2 from the center of the riblet valley ($z = 0.0$) in the spanwise direction. Maximum velocity vector magnitudes for the flow structures were slightly above 0.02U. These vortices cause a downward bulk motion of higher momentum fluid flow in the center of the riblet valley. The motion of this higher momentum fluid suggests increased levels of energy dissipation near the surfaces being possible. Even with the flow pattern showing a downward fluid flow, there is little indication of the flow moving below the riblet mid-plane.

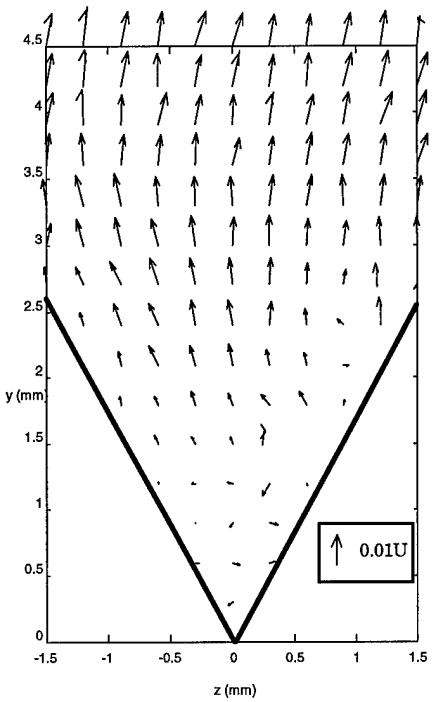

Figure 5-78: Laminar, v-w vector/U, x = 80 mm, $\beta = 0.0$

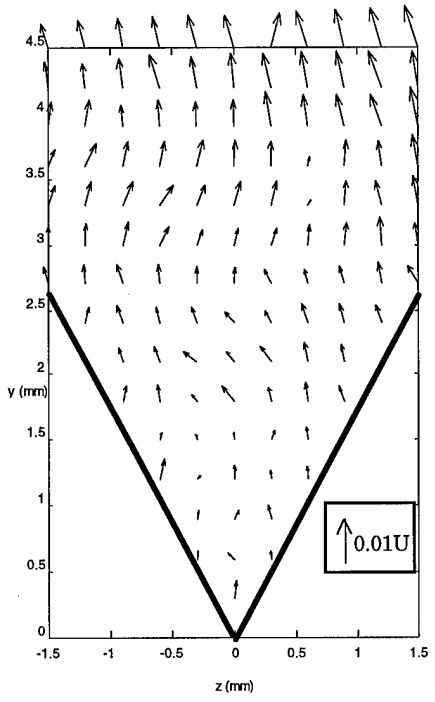

Figure 5-79: Laminar, v-w vector/U, x = 200 mm, $\beta = 0.0$

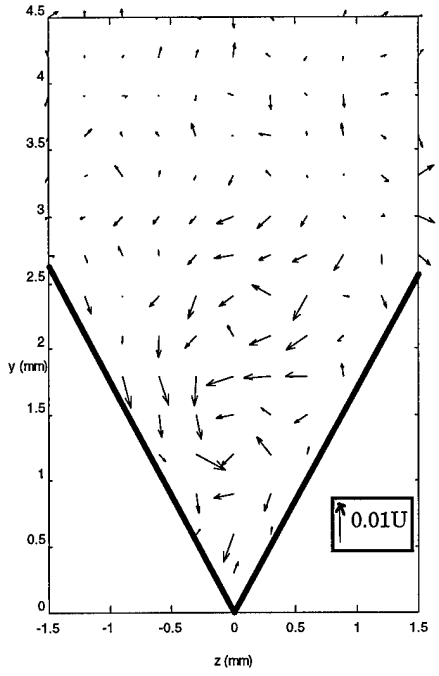

Figure 5-80: Transitional, v-w vector/U, x = 400 mm, $\beta = 0.0$

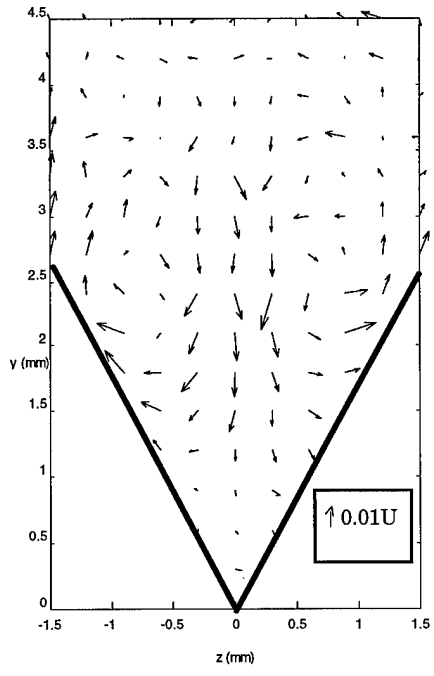

Figure 5-81: Turbulent, v-w vector/U, x = 468 mm, $\beta = 0.0$

For β = -0.1 as the turbulence intensity increased, the v-w vector showed increased randomness in the flow structures. At x = 300 mm (Figure 5-84), the flow shows an attempt to maintain a laminar characteristic as seen in Figures 5-82 and 5-83, but exhibits considerable randomness especially inside the riblet valley. The transitional flow state in Figure 5-85 showed an increase in the randomness of the v-w velocity vector similar to transitional for β = 0.0. In this figure, the v-w vectors exhibit slight bulk fluid motion resembling the formation of the vortices seen in the fully turbulent case. The turbulent flow field (Figure 5-86) has the vortex structures present in the v-w vector map. These vortices were centered at y = 2.9±0.2 mm near 0.7±0.2 mm from z = 0.0. The peak vector magnitudes for these velocities was less than 0.015U. These trends suggest the bulk fluid motion of the paired vortices formed earlier on the ribletted plate but moved relatively less higher momentum fluid into the riblet valley for the higher adverse pressure gradient.

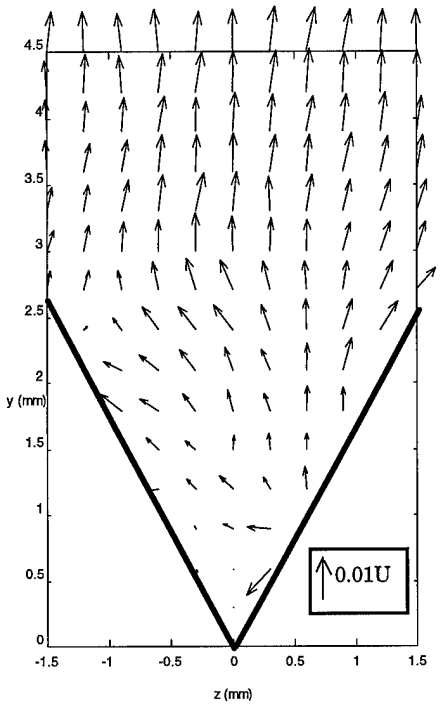

Figure 5-82: Laminar, vorticity/U , x = 80 mm, β = -0.1

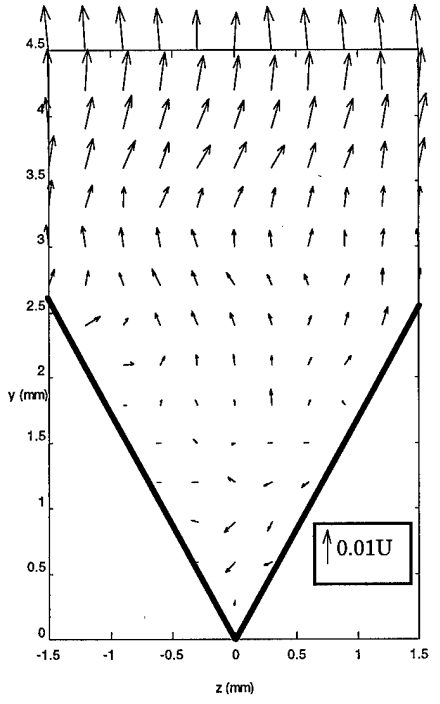

Figure 5-83: Laminar, vorticity/U , x = 200 mm, β = -0.1

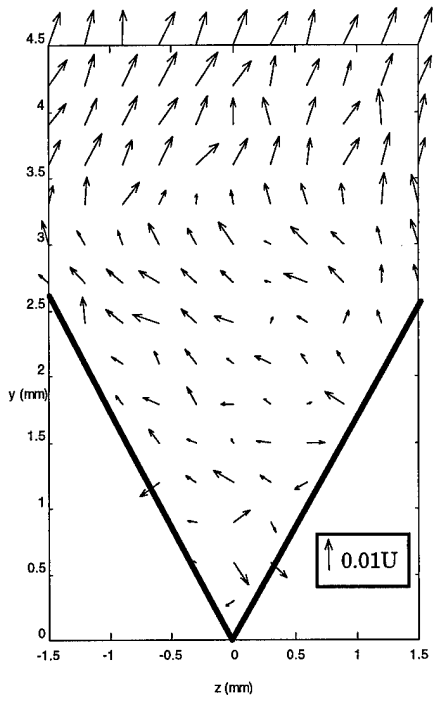

Figure 5-84: Laminar, vorticity/U , x = 300mm, β = -0.1

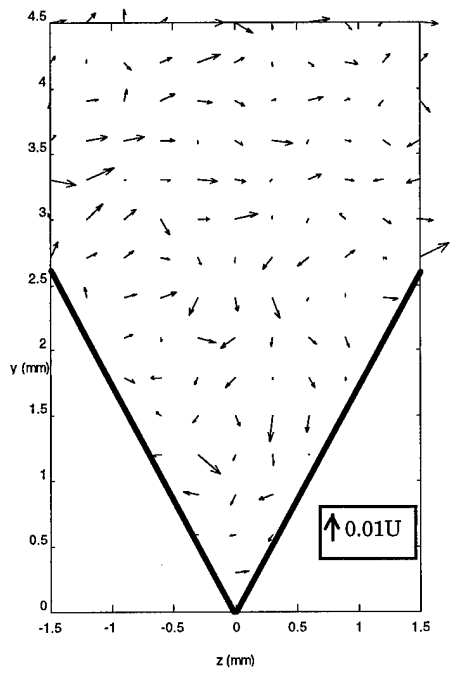

Figure 5-85: Transitional, vorticity/U, x = 400 mm, β = -0.1

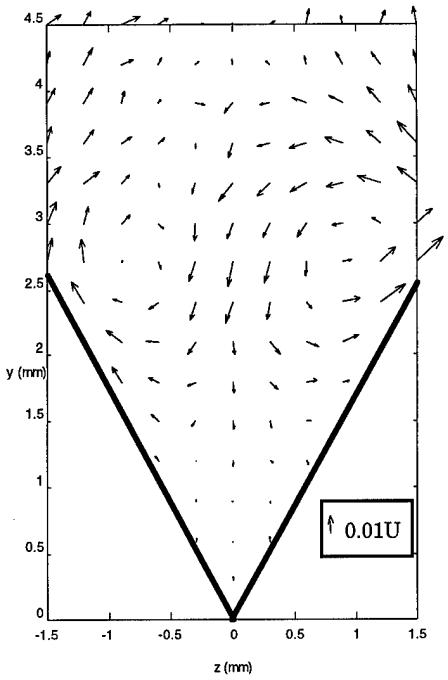

Figure 5-86: Turbulent, vorticity/U , x = 440 mm, β = -0.1

At β = -0.18, the flow field over the ribletted plate exhibited fully turbulent flow closer to the leading edge than for the previous pressure gradient conditions. The laminar flow state (Figure 5-87) shows the same uniform motion characterizing the laminar boundary layer growth. As determined in Section 5.3, turbulent flow was expected starting at x = 200 mm. Figures 5-88 and 5-89 present the flow characteristics of the v-w vector for the turbulent flow field under this pressure gradient. These vectors exhibited random motion suggesting the presence of the time dependent vortices shedding from the riblets. The evidence of bulk vortex motion between the riblets was not evident. The fact the counter-rotating vortices did not develop for this pressure gradient suggests less movement of higher momentum flow into the riblet valley. The riblet plate flow would retain drag reducing capability in turbulent flow as the adverse pressure gradient increased.

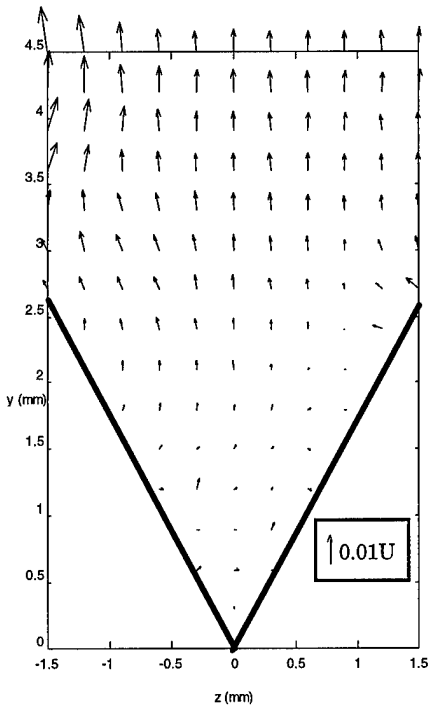

Figure 5-87: Laminar, vorticity/U , x = 80mm, β = -0.18

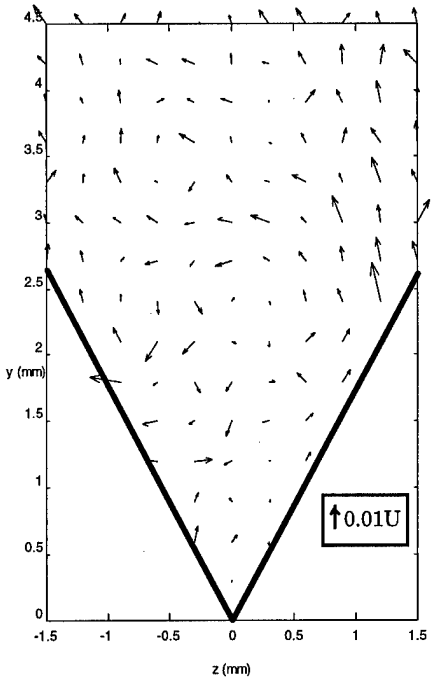

Figure 5-89: Turbulent, vorticity/U , x = 400mm, β = -0.18

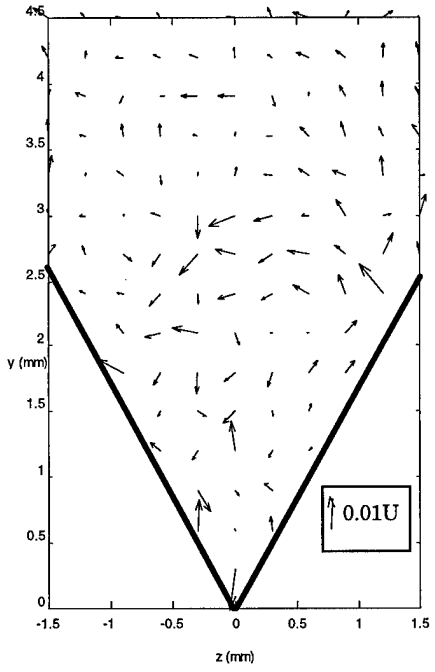

Figure 5-88: Turbulent, vorticity/U , x = 200mm, β = -0.18

5.10 Boundary Layer Profiles Above the Ribletted Plate

The boundary layers above the ribletted plate were grouped according to the flow states determined in section 5.3. The laminar boundary layer profiles were cast in the similarity variables. The transitional flow fields were plotted using wall variables. The turbulent profiles were plotted in wall variables and edge variables to fully investigate the characteristics of this flow.

5.10.1 Laminar Velocity Profiles

Figure 5-13 provides the boundary layer profiles for all of the laminar and transitional flow fields. This figure suggests two different velocity profiles for laminar flows over riblets. One profile occurred for x = 80 mm for β = 0.0 and -0.18 as a shifted profile above the other laminar boundary layers. Both profiles indicated the laminar flow field over the riblets conformed to a specific profile using the Falkner-Skan similarity variable shifted to the virtual origin (Equation 5-1). Figure 5-90 shows only the laminar profiles.

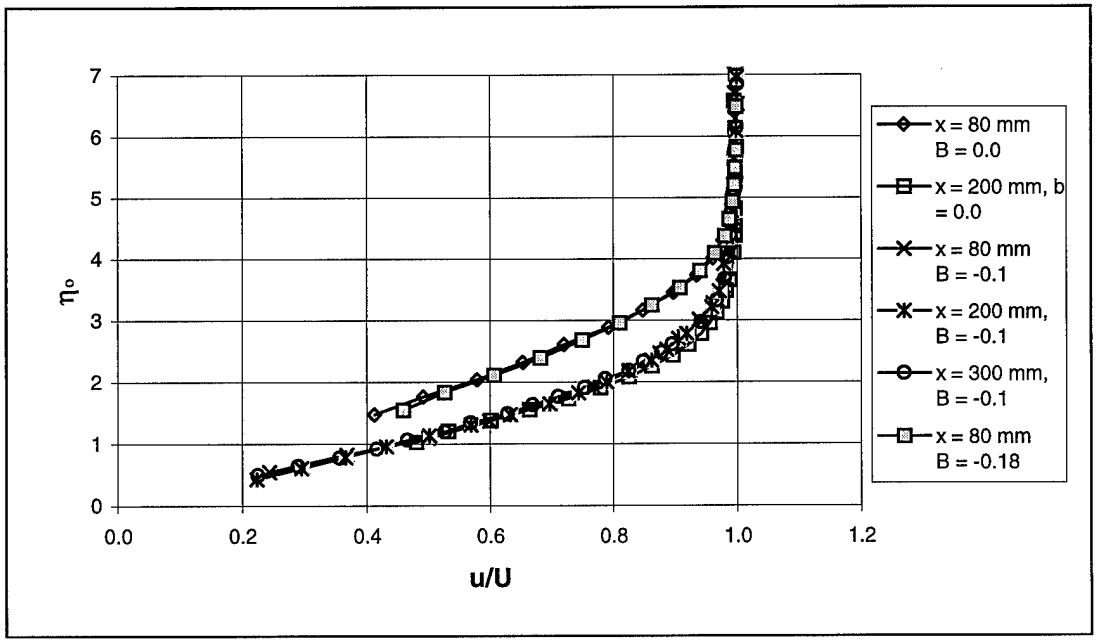

Figure 5-90: Laminar boundary layer profiles in η_o

The lower laminar profiles in η_o of Figure 5-90 characterized the boundary layer profiles with thickness above the riblets greater than the riblet height and spacing. By taking into account the pressure gradient and virtual origin in Equation 5-1, the curves collapsed along a single curve. This suggests a similarity solution for the laminar boundary layer profile using a virtual origin exists.

The profiles for x = 80 mm, β = 0.0 and -0.18 showed a shift from the other profiles due to their boundary layer thickness being less than the riblet spacing. Considering the streamwise velocity contours for these two flow conditions (Figures 5-15 and 5-24), the boundary layer thickness above the riblet peaks appears to be at a higher laboratory coordinate (y) than above the riblet valley when considering the u/U = 0.9 contour. From the boundary layer profile measurements taken above the riblet peak, the boundary layer thickness was 2.6±0.1 mm from the riblet peak. This value was nearly the same amount as the height of the riblet (2.7±0.1) and less than the riblet spacing distance (3.0±0.1 mm). For β = -0.1 at the same streamwise location (x = 80 mm), the boundary layer thickness was 2.9±0.1 mm, more than the riblet height and nearly the same value as the riblet spacing. The boundary layer thickness for this flow condition suggested the boundary layer formed over the riblet surfaces instead of from the ribletted plate surfaces as exhibited for β = 0.0 and -0.18 (x = 80 mm). The boundary layer development on the flat plate at locations where the boundary layer thickness was less than the riblet spacing, higher velocities were seen closer to the surfaces and deeper into the riblet valley (Figures 5-15, 5-19, and 5-24).

The measured streamwise Reynolds number (Table 5-1) supported the boundary layer thickness effects as well. With the boundary layer profiles conforming to a similarity

solution like a flat plate, the boundary layer thickness would have a similar relationship to the Reynolds number (Equation 5-3).

$$\frac{\delta}{x} \propto \frac{1}{\sqrt{\mathrm{Re}_x}} \tag{5-3}$$

As the Reynolds number increases, the boundary layer thickness decreases for this relationship. For the three boundary layer profiles measured at x = 80 mm, the Reynolds number (Table 5-1) for β = -0.1 would suggest a thicker boundary layer following this proportional relationship and was as measured from the velocity profiles.

The boundary layer profile shifted upward in η_o in Figure 5-90 for β = 0.0 and -0.18 (x = 80 mm) due to the linear characteristics of the velocity profile near the riblet peak. The shape of this boundary layer profile caused the virtual origin (Table 5-2) to be determined at a value relatively less than for the profiles for the thicker laminar boundary layers. Equation 5-1 shows the relationship which caused the shift in η_o with the differences in the virtual origin.

When looking at the laminar boundary layer velocities, the spanwise (w) and normal (v) velocity components needed to be addressed as well. The expected values for the spanwise velocity in the boundary layer above the peak was zero and conformed to this expected value within only small variations as can be seen in Figures 5-91 through 5-96. These figures also show how the normal (v) velocity component characterizes the increasing adverse pressure gradient and expected increasing boundary layer growth. As the pressure gradient increased, this velocity component increased in the boundary layer as well.

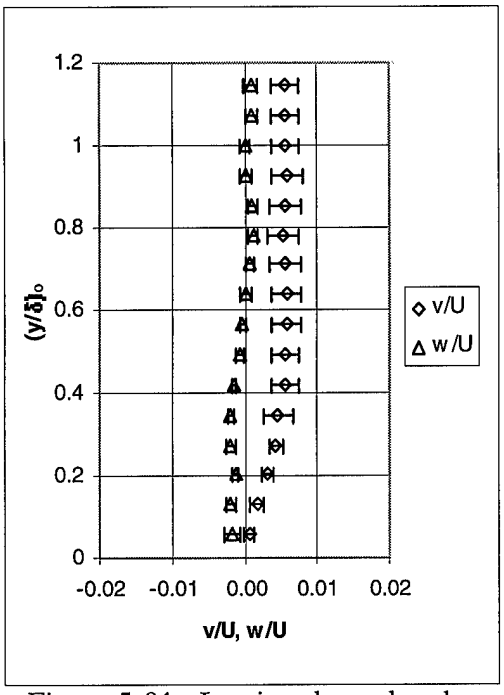

Figure 5-91: Laminar boundary layer profile, x = 80 mm, β = 0.0

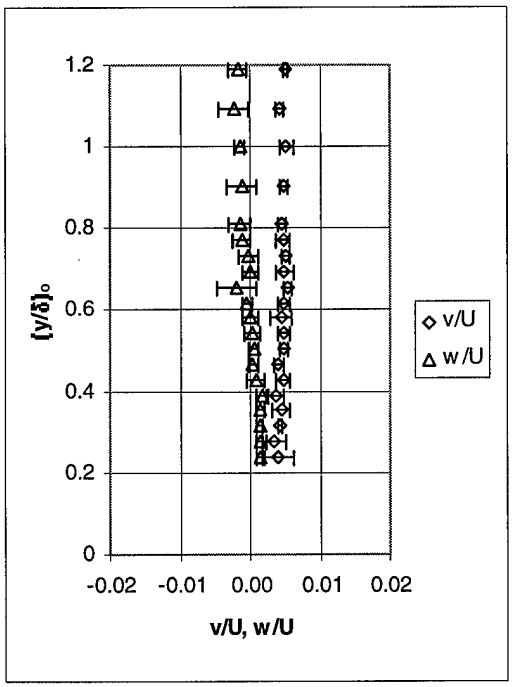

Figure 5-92: Laminar boundary layer profile, x = 200 mm, β = 0.0

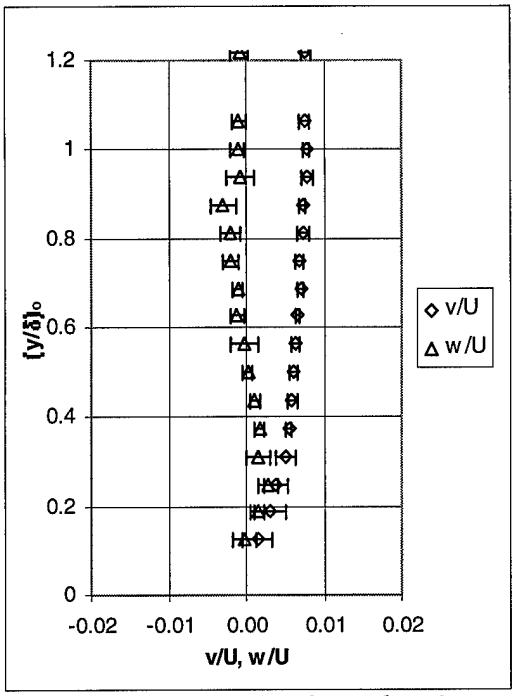

Figure 5-93: Laminar boundary layer profile, x = 80 mm, β = -0.1

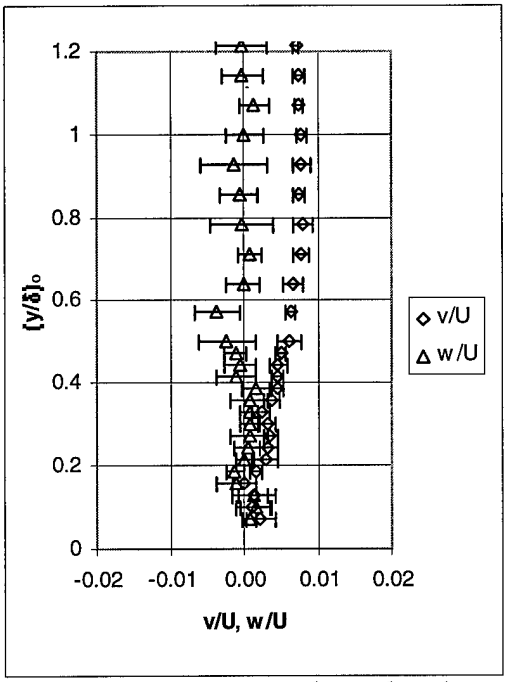

Figure 5-94: Laminar boundary layer profile, x = 200 mm, β = -0.1

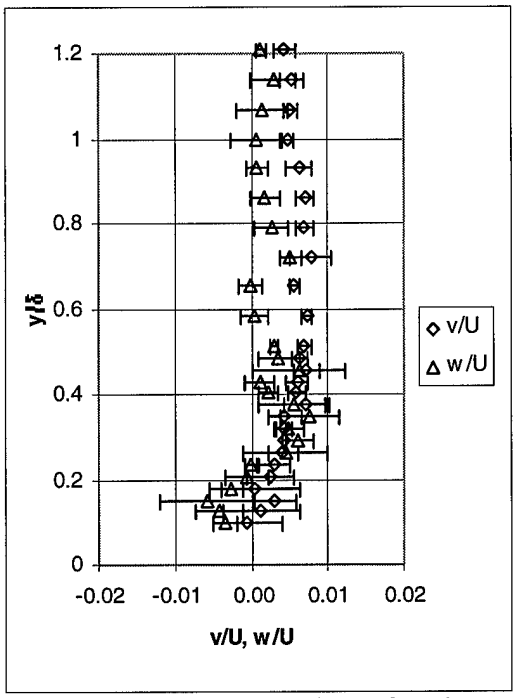

Figure 5-95: Laminar boundary layer profiles, x = 300 mm, β = -0.1

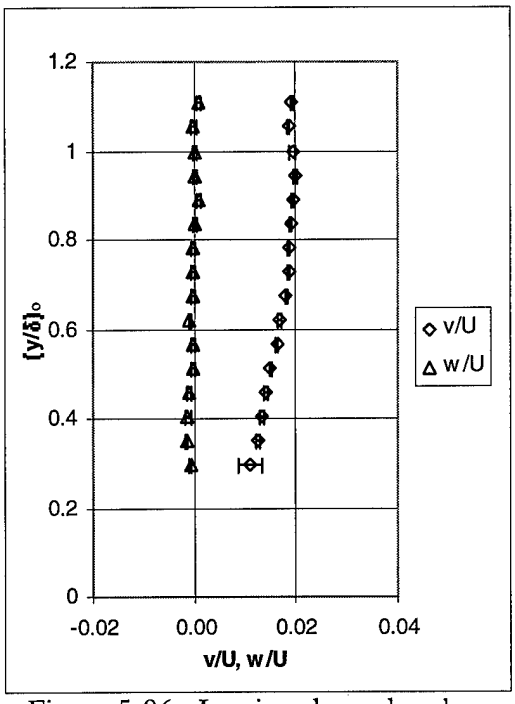

Figure 5-96: Laminar boundary layer profile, x = 80 mm, β = -0.18

5.10.2 Transitional Velocity Profiles

The boundary layer profiles for a transitional flow field condition did not correspond to any specific boundary layer profile. The transitional flow field was a laminar flow with embedded turbulence characteristics. These boundary layer profiles exhibited both turbulent and laminar characteristics. Specifically, the profile shape for x = 400 mm, β = 0.0 was similar to the laminar velocity profiles as seen in Figure 5-13 but did not conform exactly. The turbulence intensity levels for this profile peaked at 8.81% in the boundary layer. The high level of turbulence fell in the range where the velocity profile would have more turbulent boundary layer profile qualities than laminar boundary layer profile qualities. The most useful means to examine the velocity profiles for transitional flow was by using the inner variables (Figure 5-97).

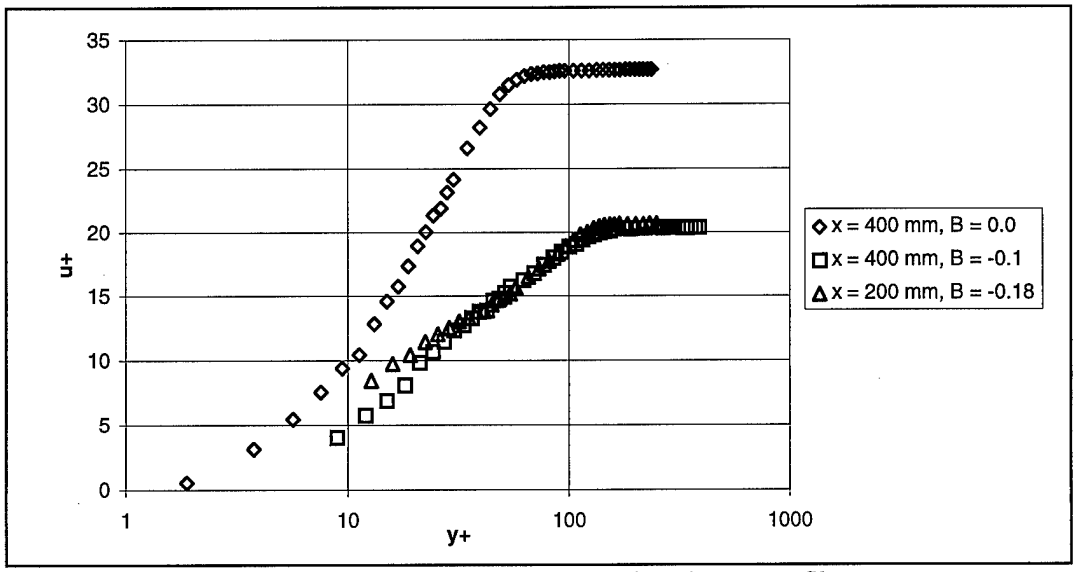

Figure 5-97: Transitional boundary layer profiles

Using the Law of the Wall and Law of the Wake equations (Equations 2-16 and 2-20, respectively), the determination of the equation constants (B, F and Π) relied heavily on accurately determined virtual origins (Table 5-2) as well as skin friction velocity (u_τ, Equation 2-19). While the velocity profile for x = 200 mm, β = -0.18 was determined to be fully turbulent, it was included here to show the effect of the pressure gradient on transitional flow. Figure 5-97 shows a shift in the boundary layer profile in the direction of reduced u^+ with an increase in adverse pressure gradient. This shift also corresponds to the changes in the momentum thickness Reynolds number (Table 5-7). The curve for β = 0.0 and x = 400 mm, β = -0.1 and x = 200 mm, β = -0.18 have a similar momentum thickness Reynolds number (375 and 372, respectively) and converged for most of the boundary layer profile. The suspected cause of the slight shift closer to the surface was the adverse pressure gradient and turbulence intensity level differences. The peak turbulence intensity for x = 400, β = -0.1 was 8.8% while for x = 200 mm, β = -0.18 the turbulence intensity was 9.0%. This small difference did not suggest a significant cause for the shift. The primary reason for the

velocity profile differences for x = 400 mm, β = -0.1 and x = 200 mm, β = -0.18 was then concluded to be the adverse pressure gradient.

Table 5-7: Momentum thickness Reynolds number

x (mm)	β = 0.00	β = -0.10	β = -0.18
80	117	112	117
200	136	207	372
300		227	
400	295	375	702
440		353	
468	337		

Table 5-8 provides a summary of the constants used for the Law of the Wall (Equation 2-16) and Law of the Wake (Equation 2-20) representations for the measured data. The value for K was constant at 0.41 as well as B for the Law of the Wake at 5.0.

Table 5-8: Equation constants for transitional profiles

	Law of the Wall	Law of the Wake	
Profile	B	Π	F
x = 400 mm, β = 0.0	17.5	5.535	4
x = 400 mm, β = -0.1	15	2.255	4
x = 200 mm, β = -0.18	8.5	2.050	-1

The roughness factor (F) of Equation 5-20 for the Law of the Wall provided an indication of the drag reducing or drag augmenting flow condition. According to Choi et al. (1993), positive values for the roughness factor suggested a reduction in skin friction drag when compared to similar flow conditions for a flat plate. Based on this criterion, the first two profiles in Table 5-8 would have less drag than a flat plate under similar flow conditions.

Considering the normal (v) and spanwise (w) velocity components for the boundary layer as well provides further indication to the flow structures near the surface of the ribletted plate. Figures 5-98 and 5-99 show increased randomness in both velocity profiles.

The spanwise velocity tended to be near a zero value as expected, but the confidence interval suggests the velocity values to have a time dependent fluctuation from the mean value present. The normal component eventually conforms to expected values to exhibit the boundary layer growth at some distance from the riblet peak but show the same variability near the surface. The velocity component confidence intervals suggest the flow was experiencing a transient state. The randomly changing vortices being generated by the riblets were considered the cause of the large confidence intervals in the normal and spanwise velocity components. Section 5.9 showed the random motion present near the riblet plates for the transitional flow fields. The random velocity measurements would produce reduced mean values when ensemble average but increased confidence interval.

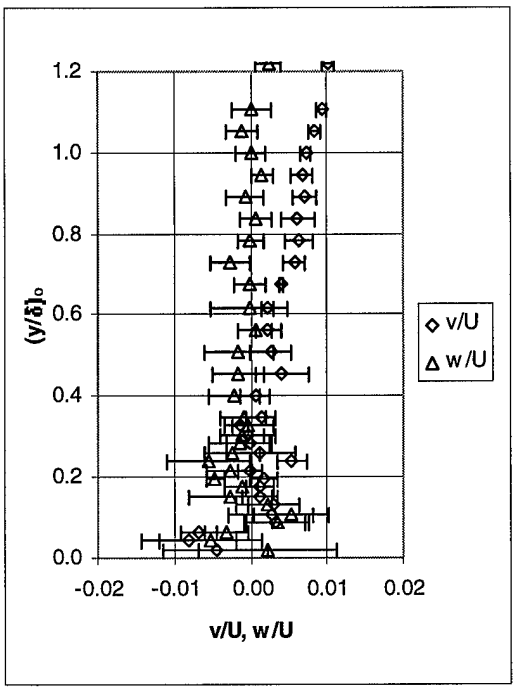

Figure 5-98: Transitional boundary layer profile, x = 400 mm, β = 0.0

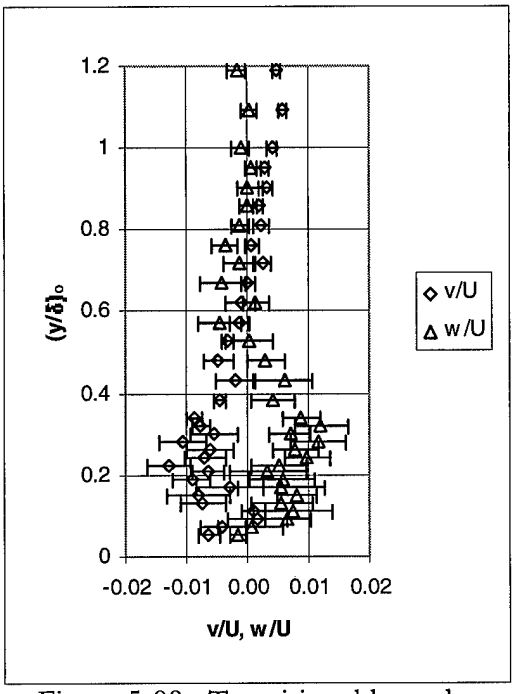

Figure 5-99: Transitional boundary layer profiles, x = 400 mm, β = -0.1

5.10.3 Turbulent Velocity Profiles

Both edge and wall variables were employed to investigate the effects of adverse pressure gradient for these flow conditions. Figure 5-100 shows the turbulent boundary layer profiles for this investigation.

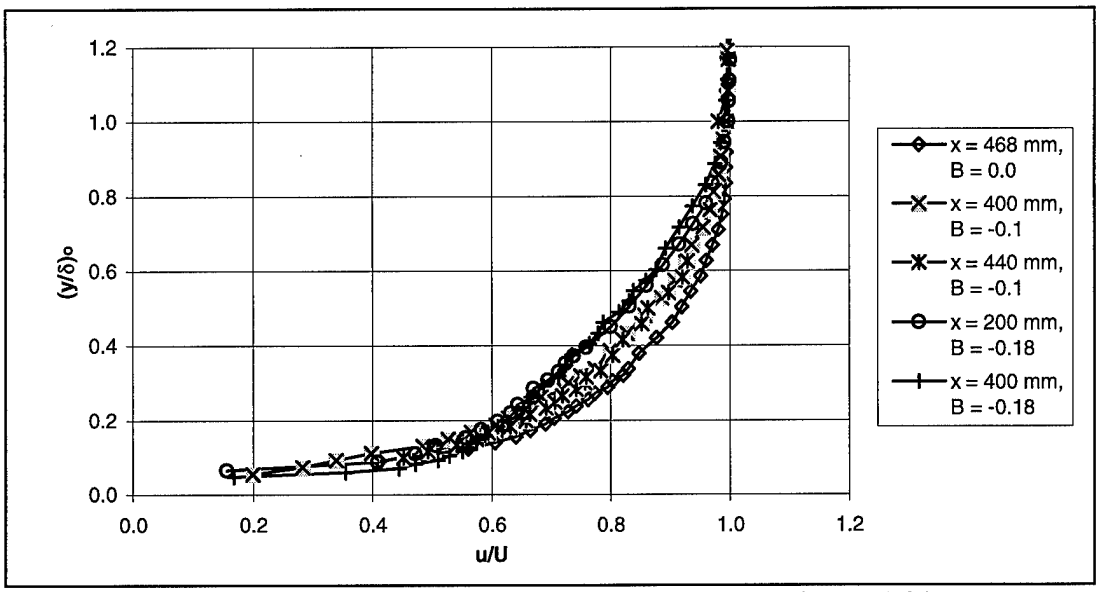

Figure 5-100: Turbulent boundary layer profiles, edge variables

As the adverse pressure gradient increased, the boundary layer profile shapes changed slightly. The data fell near a common curve below $(y/\delta)_o = 0.2$ as would be expected for the viscous sublayer. As the adverse pressure gradient increased, the velocity gradient across the boundary layer was more gradual. Figure 5-100 exhibits this behavior as a downward shift in $(y/\delta)_o$ of the boundary layer curve. This also suggests the boundary layer would be thicker. Table 5-9 confirms this suggestion.

Table 5-9: Boundary layer thickness (mm) in laboratory coordinates

x (mm)	$\beta = 0.00$	$\beta = -0.10$	$\beta = -0.18$
80	5.30	5.50	5.30
200	6.70	9.20	11.20
300		11.20	
400	11.70	12.70	19.30
440		13.70	
468	13.70		

At the highest adverse pressure gradient ($\beta = -0.18$), the boundary layer thickness increased faster for similar streamwise locations and flow field conditions. Nevertheless, locations on the ribletted plate with comparable boundary layer thickness and differing pressure gradient still showed boundary layer shape differences ($x = 468$ mm, $\beta = 0.0$ and $x = 440$ mm, $\beta = -0.1$ boundary layer thickness were both 13.70 ± 0.2 mm). Regardless of the boundary layer thickness, boundary layer profiles for the same pressure gradient corresponded to the same curve when plotted in edge variables (Figure 5-100).

The values in Table 5-7 showed an increase in the momentum thickness Reynolds number indicating a shift in the boundary layer profiles plotted in wall variables (y^+, u^+). Figure 5-101 shows the reliance of the boundary layer profile on the momentum thickness. The curves for $x = 400$ mm, $\beta = -0.1$ ($Re_\theta = 375$, transitional flow field) and $x = 200$, $\beta = -0.18$ ($Re_\theta = 372$, turbulent flow field) followed the same profile. The shift in the other boundary layer profiles resulted primarily from the differences in the momentum thickness.

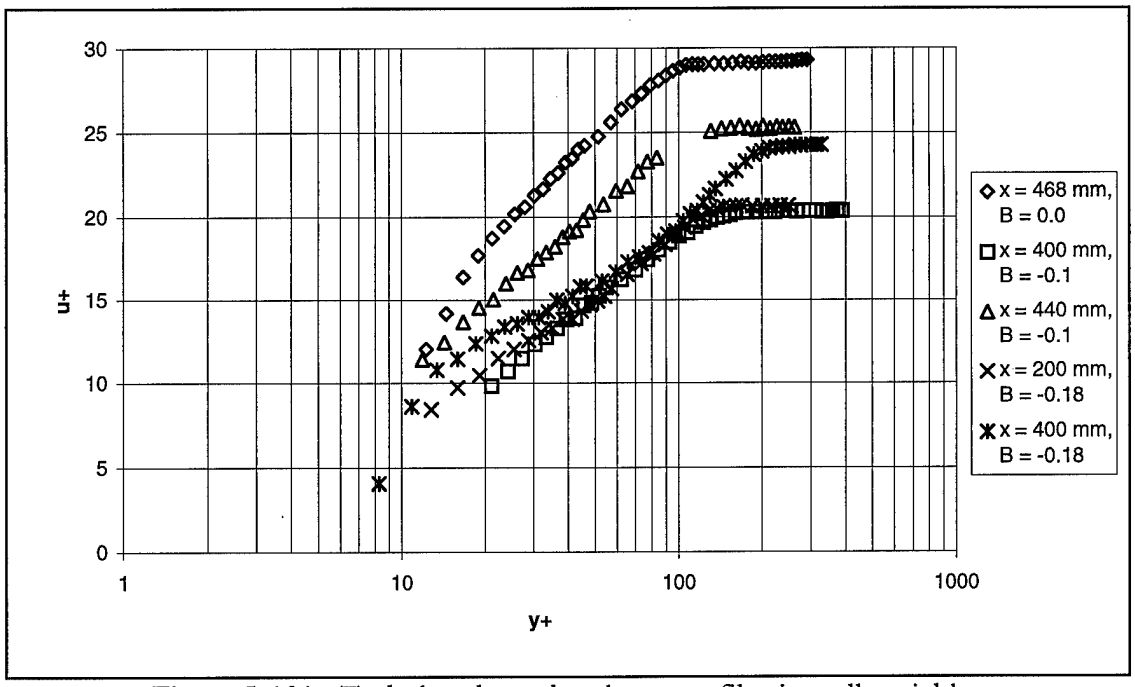

Figure 5-101: Turbulent boundary layer profiles in wall variables

The curve for x = 400 mm, β = -0.18 showed two major differences from the other turbulent profiles. The profile for this data has a different shape than the other boundary layer profiles in Figure 5-101 with a highly pronounced difference at lower values of y^+. The second major difference is in the values for u^+. For all other profiles in this figure, there is a trend showing a shift to lower values of u^+ with an increase in momentum thickness. The curve for x = 400 mm, β = -0.18 has a momentum thickness Reynolds number of 702. The trend would suggest the curve to be lower in u^+ than all other measured turbulent profiles. These two major differences suggested the flow structure near the riblets changed due to the relatively higher turbulence levels (10.3%) and thicker boundary layer (19.3 mm). Although the established adverse pressure gradient in the wind tunnel (β = -0.18) forced the flow to remain attached, these changes near the wall suggest a tendency toward separation.

Table 5-10 provides the constant values for the Law of the Wall and Law of the Wake equations describing the measured profiles shown in Figure 5-101. Again, the values of the

roughness factor (F) provided an indication of the flow condition drag augmenting or drag reducing states. The flow conditions for the first two curves in Table 5-10 show a tendency to be drag reducing based on this criteria, while all other curves show a neutral condition.

Table 5-10: Equation contants for turbulent flow

	Law of the Wall	Law of the Wake	
Profile	B	Π	F
x = 468 mm, β = 0.0	16	2.46	4
x = 400 mm, β = -0.1	15	2.255	4
x = 440 mm, β = -0.1	10	2.87	0
x = 200 mm, β = -0.18	8.5	2.050	-1
x = 400 mm, β = -0.18	7	4.1	0

The normal (v) and spanwise (w) velocity components in the boundary layer showed similar trends to those seen for the transitional flow fields. Figures 5-104 and 5-105 have larger confidence intervals near the ribletted plate for these velocity components. These figures support the conclusions discussed in section 5.9 with respect to the vortex structures at β = -0.18 pressure gradient. The secondary velocity structures were randomly occurring vortices generated by the riblets. At the higher adverse pressure gradient (β = -0.18), the vortex flow structures became more time dependent and fail to produce an organized bulk fluid motion. Figures 5-102 and 5-103 exhibit much lower confidence intervals suggesting a much lower degree of variations from the mean values for the velocity components. The normal velocity component in Figure 102 shows distinct characteristics near the riblet surface. The increased normal velocity value at the peak reducing to zero near $(y/\delta)_o = 0.3$ is consistent with the vortex motion above the riblet peaks for these flow conditions. This characteristic is less pronounced for Figure 103 due to the lower magnitude of the v-w velocity components in the vortex structures between the riblet peaks.

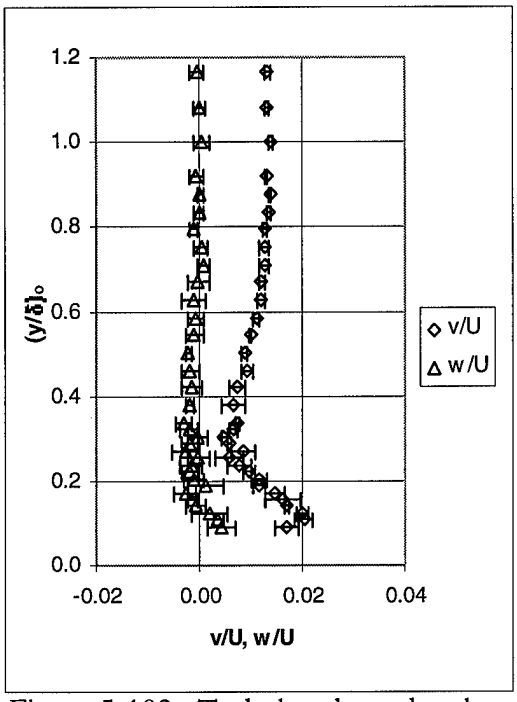

Figure 5-102: Turbulent boundary layer profile, x = 468 mm, β = 0.0

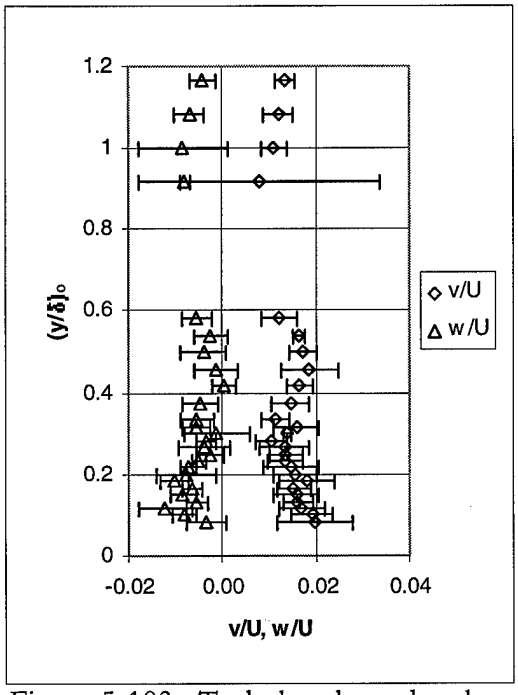

Figure 5-103: Turbulent boundary layer profile, x = 440 mm, β = -0.1

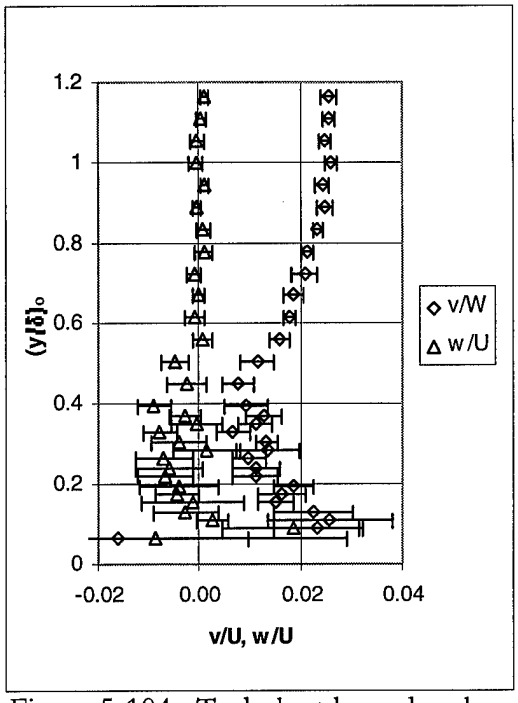

Figure 5-104: Turbulent boundary layer profile, x = 200 mm, β = -0.18

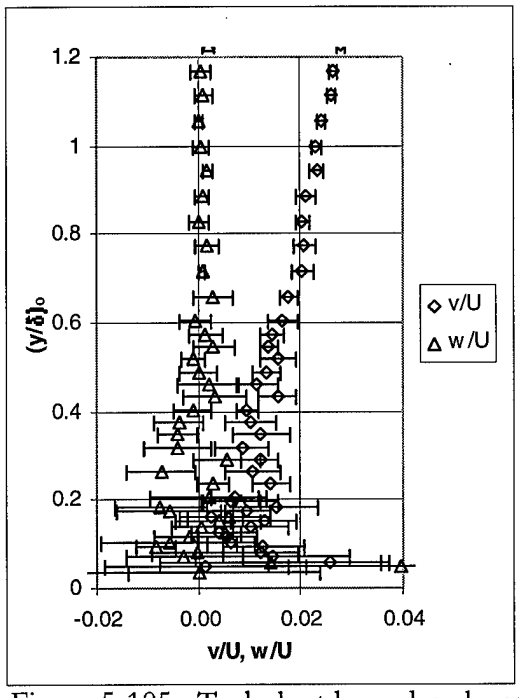

Figure 5-105: Turbulent boundary layer profile, x = 400 mm, β = -0.18

5.11 Skin Friction Coefficient Determination

The skin friction was calculated at each flow field location using Equation 2-27 and values are included in Table 5-11. For the laminar case at x = 80 mm, the magnitude of the skin friction coefficients appeared to decrease slightly with increasing pressure gradient.

Table 5-11: Calculated average skin friction coefficient

x (mm)	$\beta = 0.00$	$\beta = -0.10$	$\beta = -0.18$
80	0.005541	0.004680	0.003659
200	0.004539	0.003927	0.008258
300		0.005091	
400	0.009699	0.009149	0.008323
440		0.008127	
468	0.009136		

These values were highly sensitive to the position uncertainty with respect to the riblet surface. For this reason, Figures 5-106 through 5-108 show error bars based on a position uncertainty of ±0.1 mm. This uncertainty was a result of the traverse system tolerances and uncertainties introduced when locating the surface of the riblets. The traverse system has ±0.05 mm tolerances in the gears used to position the measurement volume. When locating the surface, positioning of the measurement volume could be aligned improperly. The laminar and turbulent curves on Figures 5-106 through 5-108 result from Equations 2-23 though 2-26 for a smooth, flat plate. The smooth, flat plate, laminar skin friction coefficients were calculated from Equation 2-23 for a zero pressure gradient and Equation 2-25 for the adverse pressure gradient conditions. The turbulent skin friction coefficients for a smooth, flat plate were calculated from Equation 2-24 for zero pressure gradient and Equation 2-26 for the adverse pressure gradient conditions. These equations provide a means to compare the calculated values to a flat plate with similar flow properties,

specifically turbulence intensity. The ribletted plate would accelerate the turbulence intensity along the streamwise coordinate when compared to a flat plate (move the transition point toward the leading edge). The flat plate data for this investigation was laminar at 400 mm under a zero pressure gradient as compared to the transitional flow field exhibited at the same streamwise location and pressure gradient for the ribletted plate. In Figures 5-106 through 5-108, a flat plate would show laminar skin friction coefficient values at distances further from the leading edge than the riblet plate shows.

The calculated skin friction coefficients showed higher drag values at all locations when compared to predicted smooth plate values. Investigations by Walsh (1982) have shown that the riblet spacing of $s^+ < 30$ and riblet height of $h^+ < 25$ would produce less drag than for a similar smooth plate. The values for the riblet spacing and height in wall variables was calculated for each location being investigated (Table 5-12). These values were all greater than the limits determined by Walsh (1982) for these flow conditions.

Table 5-12: Riblet spacing, s^+

x (mm)	$\beta = 0.00$	$\beta = -0.10$	$\beta = -0.18$
80	37.37	35.00	33.32
200	33.35	31.60	49.23
300		35.16	
400	48.55	46.89	46.96
440		43.00	
468	50.09		

Table 5-13: Riblet height, h^+

x (mm)	$\beta = 0.00$	$\beta = -0.10$	$\beta = -0.18$
80	32.39	30.33	28.88
200	28.90	27.38	42.66
300		30.48	
400	42.07	40.64	40.70
440		37.27	
468	43.41		

Figure 5-106 shows how the skin friction develops over the ribletted plate in the spanwise direction at $\beta = 0.0$. The change in drag from x = 80 to 200 mm follows the trend seen in the streamwise velocity contours. With the thinner boundary layer closer to the leading edge of the ribletted plate, it developed between the riblet peaks moving higher momentum flow closer to the surface. With this higher momentum flow near the surface, a higher rate of energy dissipation and skin friction would be expected. As the boundary layer thickness increased, the boundary layer developed over the ribletted plate (x = 200 mm) and less higher momentum flow moved into the ribletted valley. The skin friction would then be less for this case. With the increased turbulence intensity exhibited at the transitional flow condition (x = 400 mm), the skin friction increased as well. Interestingly, as the flow developed the counter rotating vortices between the riblet peaks (more organized flow pattern), the skin friction coefficient reduced slightly.

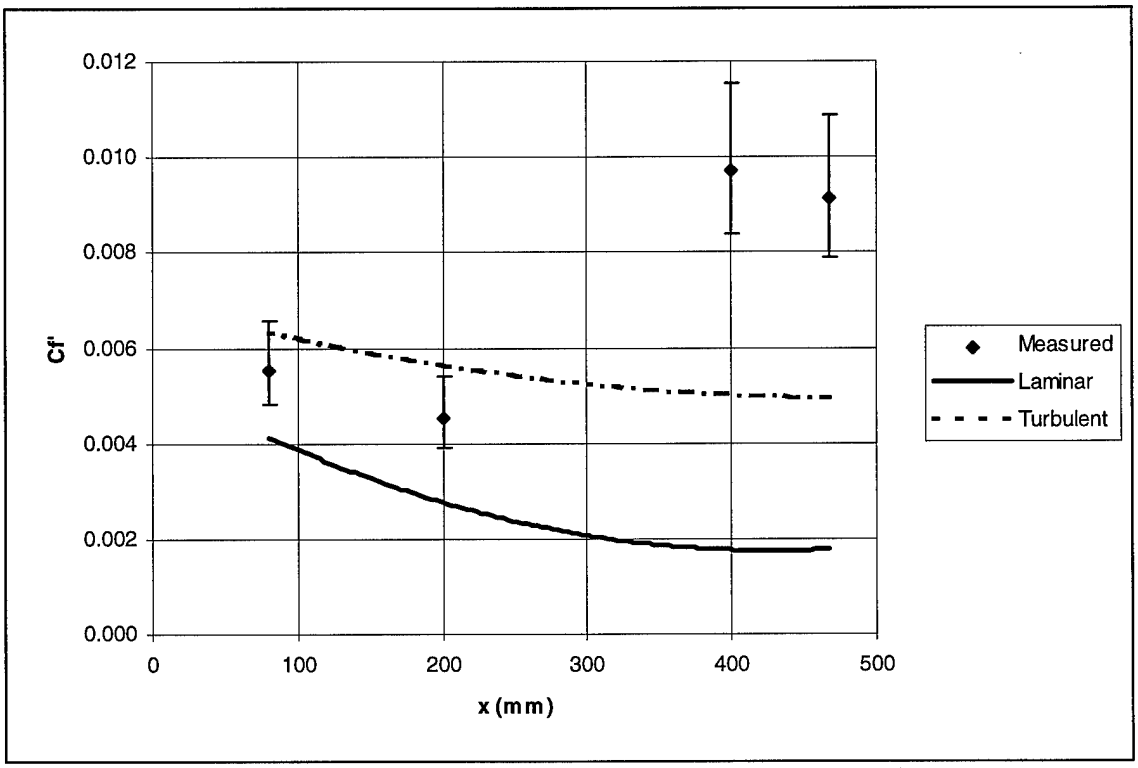

Figure 5-106: Coefficient of friction, zero pressure gradinet

As the pressure gradient increased, the difference between the calculated values and predicted values for the skin friction coefficient also increased. The relative magnitudes of the coefficients did not change dramatically, though. At $\beta = -0.1$ in Figure 5-107, the same development was evident. The skin friction coefficient reduced slightly from the leading edge where the boundary layer thickness was less than the riblet spacing. At x = 200 where the boundary layer thickness increased, the boundary layer fully developed above the ribletted plate instead of in the valley. As the turbulence intensity increased so did the skin friction coefficient. Once again, the skin friction coefficient appeared to reduce slightly when the flow field developed the more organized flow structures seen in the fully turbulent flow field (counter rotating vortices).

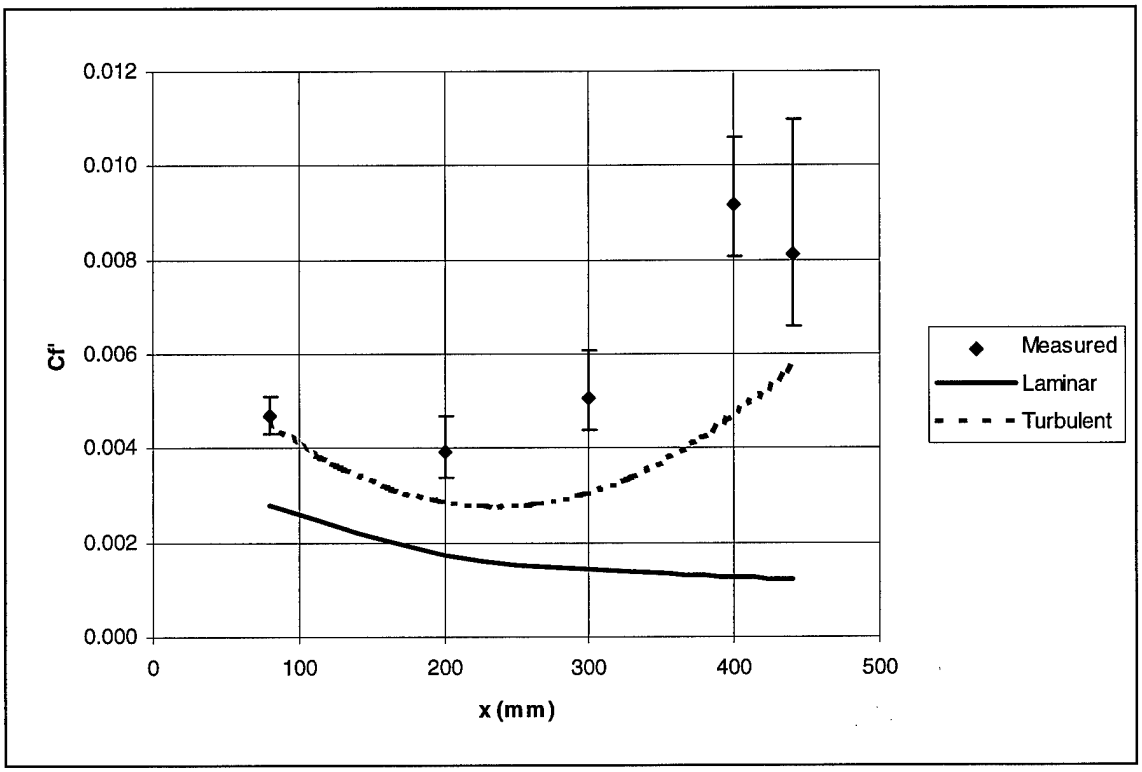

Figure 5-107: Coefficient of friction, $\beta = -0.1$

At the most severe adverse pressure gradient, β = -0.19, the flow field became fully turbulent at less than 200 mm from the leading edge. The difference between the calculated and predicted values is larger than those for the lesser adverse pressure gradient conditions. Also, there is no slight reduction in the highly turbulent flow field. This corresponds with the observations seen when examining the v-w velocity vector. There were no sustained vortex structures observed between the riblet peaks for these flow conditions.

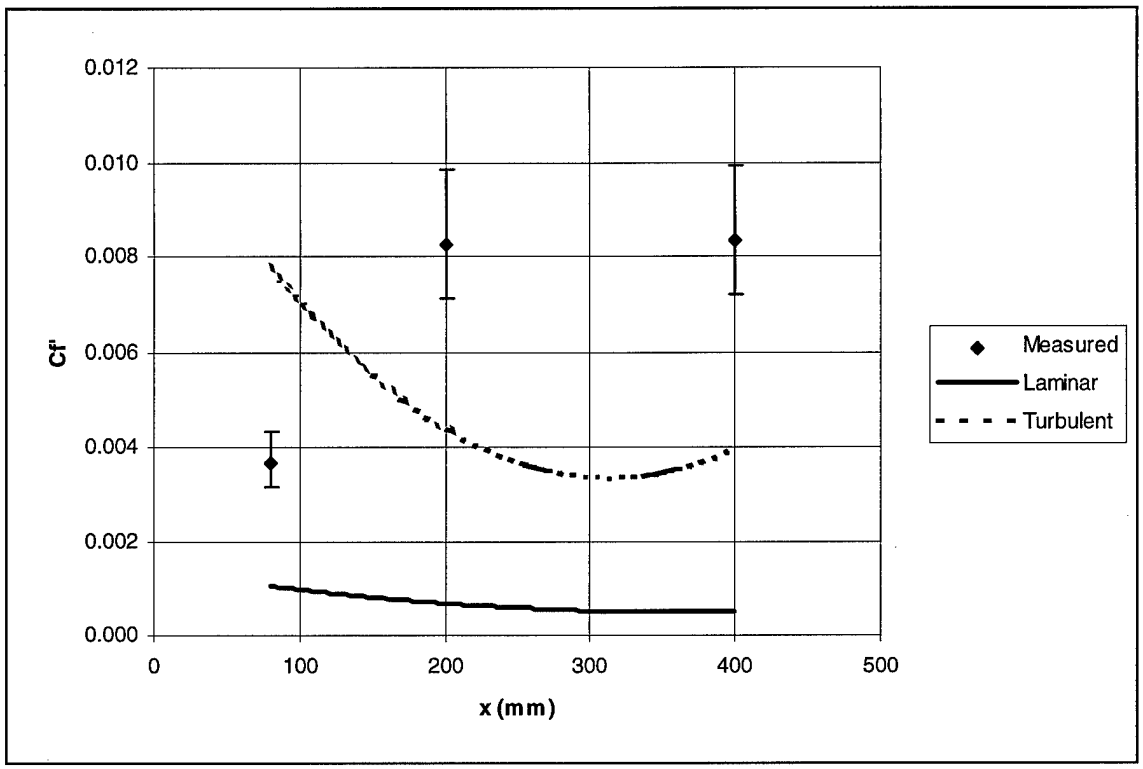

Figure 5-108: Coefficient of friction, β = -0.18

To compare changes between the skin friction coefficients at the same locations as the adverse pressure gradient increased, all values were plotted together in Figure 5-109. This figure shows how the flow properties developed over the riblet plate as discussed earlier. More importantly, the values at a give streamwise location exhibits small magnitude decreases with increases in the adverse pressure gradient. The exception is at 200 mm for β = -0.18. At this flow condition, the turbulence intensity would dominate the viscous energy

production causing the skin friction drag to be significantly higher than for $\beta = 0.0$ or -0.1 (laminar flow fields).

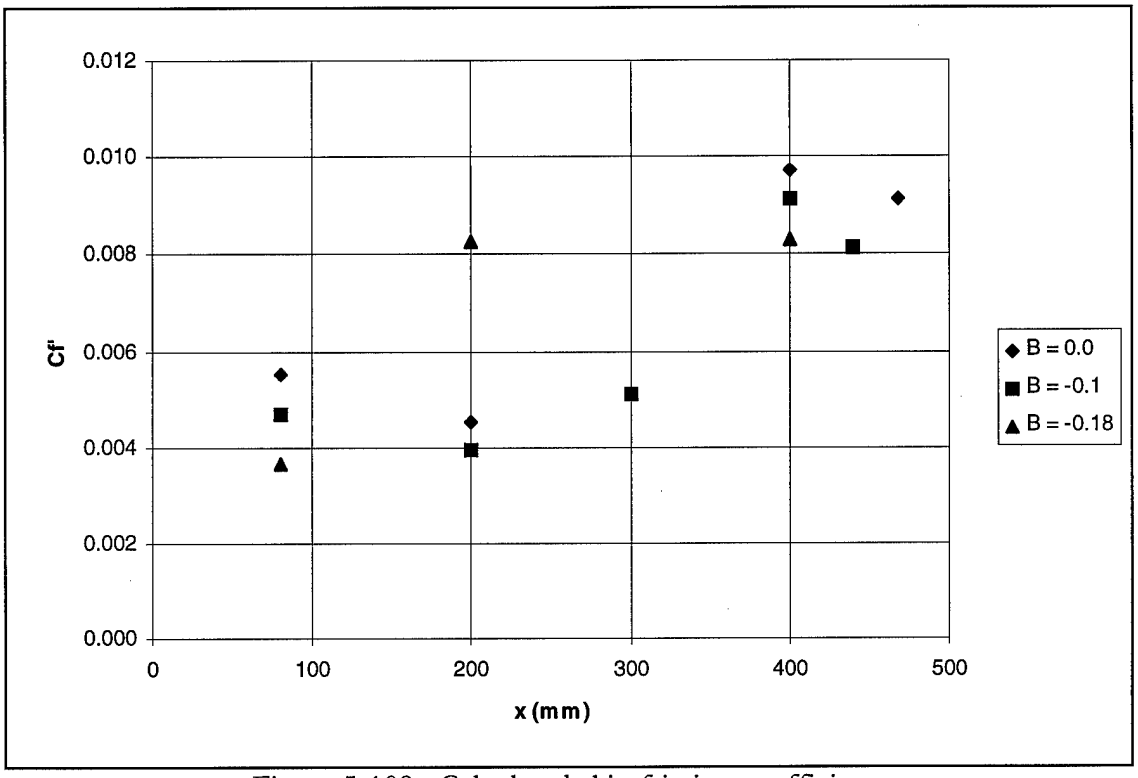

Figure 5-109: Calculated skin friction coefficients

5.12 Effects of Asymmetric Surface Roughness and Yawed Freestream Flow

In satisfying the objectives of this investigation two significant phenomena were observed, effects of flow angle on the vortex structures between the riblets and the effects of asymmetric roughness on the riblet surfaces.

5.12.1 Effects of Flow Angle on Velocity Structures Over a Ribletted Plate

By intentionally introducing a spanwise component of velocity with respect to the riblets, the flow structures inside the riblet valley changed. Walsh (1990) has shown the drag reducing properties to be relatively unaffected by yawed flows by a flow angle to the riblets by as much as fifteen degrees under a zero pressure gradient. The flow velocity structures

were affected, though. Figure 5-110 shows a v-w vector profile between two riblet peaks under a spanwise velocity in the freestream of 0.15U (freestream yawed 8.5 degrees from the riblet orientation). These measurements were taken at x = 400 mm, β = 0.0. This transitional flow regime produced a steady flow pattern with some bulk fluid motion into the riblet valley for streamwise flow aligned with the riblets. Figure 5-109 exhibits larger amounts of higher momentum flow moving closer to the riblet walls. This suggests flow angle in the transitional flow regime will affect the drag reducing capabilities of the ribletted plate.

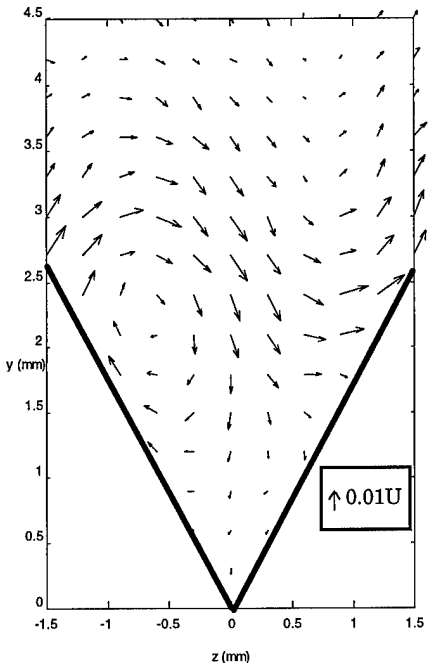

Figure 5-110: Transitional, v-w vector/U, x = 400 mm, β = 0.0, crossflow effect

5.12.2 Asymmetric Surface Roughness

With the riblets having been machined out of plexiglass, differences in surface roughness are very possible. Obtaining valid velocity information between two riblet peaks required ensuring the roughness was somewhat constant for the entire riblet valley. The v-w vector

mapping provided a means to recognize differences in the surface roughness and could be verified visually with a spotting scope at those locations exhibiting differences in roughness. Differences in surface roughness would cause the boundary layer to grow in the rougher region more quickly than anywhere else. Figure 5-111 shows a boundary layer difference in the spanwise direction and how it was characterized in a nearly laminar flow. Higher values of the normal velocity (v) component near the surface with a higher roughness were apparent. In Figure 5-111, the higher level of surface roughness would occur near the riblet peak at z = -1.5 mm. The visual inspection using a spotting scope of the ribletted plate verified the asymmetric surface condition for this flow condition to be just below the peak. The measurements for the riblet investigation were repeated between different peaks at a distance from this specific valley in Figure 5-111 to eliminate any influence of this asymmetric roughness effect.

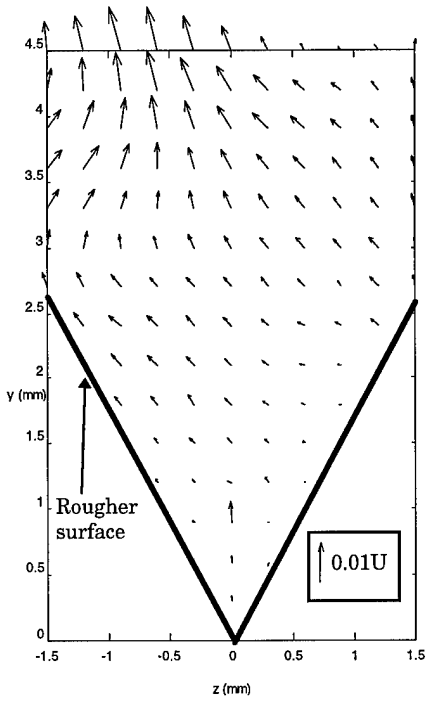

Figure 5-111: Laminar, v-w vector/U, x = 80 mm, β = 0.0, asymmetric roughness

6. Conclusions and Recommendations

This investigation studied many aspects of the flow properties over a ribletted plate under three specified pressure gradients (β = 0.0, -0.1, and -0.18). Several locations along the plate were investigated to include laminar, transitional, and turbulent flow fields. The investigator considered three objectives for these flow conditions:

1. Determine the flow field state (laminar, transitional, or turbulent) based on turbulence intensity and boundary layer profile.
2. Investigate the various flow parameters describing the flow over the riblets including any relation to skin friction properties.
3. Calculating average, local skin friction coefficients at various location along the ribletted plate and compare them with predicted smooth plate values.

Velocity measurements were made at each investigated location using the LDA system. These measurements allowed the determination of the studied flow parameters including velocities, turbulence intensities, Reynolds stress, skewness, flatness, and vortex structures.

6.1 Flow Field State

Turbulence measurements made in the boundary layer as well as the streamwise velocity boundary layer profiles helped determine the flow field state. Final determination of the flow field state used both criteria, but considered the flow character (boundary layer profiles) to be a more decisive discriminator. Table 5-4 provides the flow locations studied and the flow field state determinations made for this investigation.

The peak turbulence intensity levels in the boundary layer were compared to the criterion established earlier to determine the flow state. This criterion established laminar flow fields having turbulence intensity less than 3% of the freestream velocity as calculated

by Equation 2-5. Fully turbulent flows were considered to have peak turbulence intensity levels in the boundary layer above 9% of the freestream velocity. Flow states with turbulence intensity levels between 3% and 9% were initially considered transitional.

Those flow locations considered either laminar or transitional (as determined from turbulence intensity) were compared by plotting the streamwise boundary layer profiles using a similarity variable based on the Falkner-Skan similarity variable, ηo (Equation 5-1). All laminar profiles collapse to two distinct curves (Figure 5-13). The transitional flow field boundary layer profiles did not conform to these curves. The turbulent and transitional flow (as determined from turbulence intensity) were plotted together using the edge variables shifted to the virtual origin (Equation 5-2). Figure 5-14 shows three distinct turbulent boundary layer profiles depending on the pressure gradient. The transitional flow field boundary layers did not conform to these curves.

The virtual origin was used in calculating the normal distance parameter (η_o and $(y/\delta)_o$) from the plate for both Equation 5-1 and 5-2. The virtual origin provided the location from the riblet valley equivalent to a comparable flat plate having the same drag and boundary layer profile above the plate.

6.2 Flow Parameters Over the Ribletted Plate

The flow parameters of interest for this investigation included the streamwise velocity, turbulence intensity, Reynolds stress, skewness, flatness and secondary vortex structures. These parameters were investigated in the valley between the riblet peaks. To further describe the flow over the ribletted plate, boundary layer profiles were studied.

The streamwise velocity contours were used to determine the boundary layer development between the riblet peaks and the penetration of higher momentum flow into

the valley. Laminar flow fields over the ribletted plate depend on the boundary layer thickness and can be described by the local freestream Reynolds number. For boundary layer thickness less than the riblet spacing at the locations closer to the leading edge, the boundary layer developed in the riblet valley instead of over the flat plate. As the boundary layers thickened, the boundary layer developed over the plate and boundary layer profiles above the peak and valley converged to the same velocity levels slightly above the riblet peaks. As the turbulence intensity increased (flow states from laminar to transitional to turbulent), the higher momentum flow penetrated deeper into the riblet valley. With higher momentum flow closer to the surfaces, more kinetic energy would be dissipated to the surface increasing the skin friction drag. As the pressure gradient increased, the higher momentum flow penetrated the valley less for the laminar case but did not seem to show any difference for the transitional or turbulent case. This explains the slight drag reductions experienced for the laminar state as the adverse pressure increased.

Turbulence intensities peaked near $(y/\delta)_o = 0.2$ in the boundary layer above the riblet peak for the laminar and transitional case and near $(y/\delta)_o = 0.1$ for the turbulent cases. Turbulence intensity contours in Figures 5-30 through 5-41 provide information on this parameter. All flow conditions suggest the peak turbulence occurred just above the riblet peaks except x = 400 mm, $\beta = -0.18$. At this flow condition, the flow properties changed near the ribletted surface. The laminar cases showed fairly uniform turbulence intensities between the riblets with decreases close to the riblet surfaces. The turbulence intensities for the transitional and turbulent flow conditions showed decreasing values into the valley with a large gradient near the riblet surfaces.

Reynolds stresses indicate shifts in the average production of turbulent kinetic energy which affects energy production and dissipation rates. With the established flow conditions directed along the riblets, the most significant Reynolds stress was u'v'. Since the freestream velocities exhibited some level of turbulence for all flow conditions, Reynolds stress would not be zero for any case. The values for the laminar flow conditions showed relatively uniform values in the riblet valley with decreases near the surfaces. The transitional flow cases showed higher values just above the peaks with gradual decreases into the riblet valley. This suggests the skin friction near the peaks was higher than along the surfaces in the valley. The turbulent flow fields showed similar trends to those seen for the transitional flow. For this reason, the conclusion that the skin friction near the riblet peaks was higher than along the surfaces in the valley is supported for turbulent flow fields as well.

Skewness is a measure of the variations of the local velocity from the mean value. Higher values of skewness correspond to increased dissipation of kinetic energy and an increase in skin friction. The flow developing over the ribletted plated exhibited an increasing skewness gradient into the riblet valley. A gradient was also evident along the surfaces of the riblets. As the turbulence intensity increased (flow states changing from laminar to transitional to turbulent), the skewness maximum values moved from above the mid-plane (y = 1.3 mm in laboratory coordinates, half the height of the riblets) to locations just below the mid-plane. With the maximum values at and below the mid-plane for turbulent flow field conditions, energy dissipation deep in the valley would be expected. The changes in pressure gradient showed little affect on the magnitude of the skewness for the turbulent flow conditions in this investigation. Following this trend, the riblets would be

expected to retain the drag reducing capabilities under an adverse pressure gradient for a turbulent flow field.

Flatness indicates the frequency of the velocity excursion above the mean described by the skewness factor. Higher levels of flatness correspond to the increases in higher momentum energy dissipation. For the laminar flow fields, maximum values occurred just above the mid-plane. The transitional and turbulent flow fields had maximum values at the mid-plane. This trend suggests higher momentum flow penetrated deeper into the valley for higher turbulent flow but did not penetrate below the mid-plane very frequently. Coupled with the decreased turbulence intensity and increased skewness characteristics below the mid-plane, the flatness factor indicated the energy dissipation below the mid-plane would be considerably lower than at other locations along the surface. The flatness factor showed little change with changes in the adverse pressure gradient.

Investigating the secondary velocity structures in the flow field between the riblets used the normal (v) and spanwise (w) velocities in the y-z plane. The v-w velocity vectors for the laminar flow fields showed uniform boundary layer growth with only slight spanwise velocity. Transitional flow fields appeared to be highly random with some bulk motion moving higher energy flow into the riblet valleys. Turbulent flow fields developed a pair of counter rotating vortices between the riblet peaks which moved higher momentum flow deeper into the valley. As the adverse pressure increased, the trends seen for the laminar and transitional flow fields were not significantly altered. For the turbulent case, though, the magnitude of the velocity vectors decreased and eventually the vortices became random events similar to the structures seen for the transitional flow field.

The boundary layer profiles over the ribletted plate showed several significant trends. The laminar flow conditions conformed to two distinct similarity solutions. Boundary layers thinner than the riblet spacing conformed to one similarity solution. For thicker boundary layers which developed over the plate, another solution exists. These profiles were plotted in η_o. Using edge variables, the turbulent boundary layer profiles formed distinct curves based on the pressure gradient condition. As the pressure gradient changed, the shape of the curve changed slightly. When plotting the turbulent and transitional flow field boundary layers in wall variables, the reliance on momentum thickness was evident. As the momentum thickness Reynolds number increased, the boundary layer profiles shifted lower in u^+.

These flow parameters each indicate an expected influence on the skin friction of the plate with increasing pressure gradient. The streamwise velocity profiles suggested lower momentum flow existed deeper in the valley with increasing pressure gradient (most likely due to the increased boundary layer growth) and would produce a lower level of skin friction. The turbulence intensity profiles showed an increased randomness when the adverse pressure gradient was increased to $\beta = -0.18$. This randomness suggests an increase in the dissipation of kinetic energy and skin friction drag. The Reynolds stress increased in magnitude over the ribletted plate as the pressure gradient increased. This increased results for increases in skin friction as well. While the skewness and flatness values showed trends with turbulence intensity changes, the adverse pressure gradient increase caused no effect on these parameters suggesting the ribletted plate retained much of the drag reducing ability seen in zero pressure gradient flow fields. Of particular importance was the development of the secondary velocity structures between the riblets. As the pressure gradient increase,

higher turbulence intensities were seen at closer locations to the leading edge. Also, the pair of counter rotating vortices developed under a zero pressure gradient condition in turbulent flow dissipated indicating less bulk fluid motion of higher energy flow moving into the riblet valley.

While some of the statistics in the flow field provided competing information as to the effect of the adverse pressure gradient, the reduction of the bulk fluid motion of higher momentum flow moving into the riblet valley is a strong indicator of drag reducing capability as the adverse pressure gradient is increased for turbulent flow. This is reinforced by the trend seen with the flatness and skewness parameters. Since the laminar flow field depends on uniform flow to produce low levels of drag, this mechanism was of no help in maintaining a drag reducing state and a stronger indicator would be the Reynolds stress. For this reason, the drag condition would be expected to show an increase for laminar flow fields over a ribletted plate as the adverse pressure gradient increased when compared to similar flow conditions over a flat plate.

6.3 Skin Friction Coefficient

An average skin friction coefficient was calculated for each flow condition using Equation 2-23. These values were compared with predicted laminar and turbulent values for a smooth plate. Due to the geometry and flow conditions for this investigations, all measured locations resulted in skin friction coefficients higher than predicted values for a smooth plate.

The development of the skin friction coefficient values along the streamwise direction followed the development of the boundary layer as seen in the streamwise velocity contours. At locations close to the leading edge with boundary layer thickness less than the riblet

spacing, the boundary layer developed in the valley moving higher momentum flow closer to the riblet surfaces. As the boundary layer thickness increased, the higher momentum flow penetrated the valley less and the skin friction coefficient was slightly lower. Further along the streamwise direction, the turbulence intensity dominated the flow field and higher momentum flow penetrated the valley again. For these transitional and turbulent flow field conditions, the skin friction values were much higher. As the flow developed the sustained vortex structures seen in the turbulent flow fields for $\beta = 0.0$ and -0.1 ($x = 468$ and 440 mm, respectively), the skin friction drag reduced slightly as well. This more organized flow decreased the viscous energy production slightly.

6.4 Recommendations

Based on findings from this investigation, three recommendations are being presented. The first is the addition of a better method to adjust the wind tunnel test section walls to create and manipulate the pressure gradient. The current configuration does not provide for a graduated method to adjust the side walls of the wind tunnel and limited the range of adjustments needed to remove spanwise flow found in the wind tunnel.

Another recommendation relates to the conditions measured in the test section. Further exploration of the velocity structure changes exhibited at $x = 400$, $\beta = -0.18$ are needed to fully explain the phenomena near the wall. The flow structure was forced to remain attached ($\beta = -0.18$) for the length of the test section. At this advanced location along the test plate, the flow characteristics near the wall changed causing a much thicker boundary layer, higher turbulence intensity, and maintained values of skin friction below the predicted values for a similar flat plate.

The third recommendation is a suggested research area as well. The velocity structures seen due to a velocity component in the spanwise direction could change the drag-reducing ability of this ribletted plate. Further investigation to determine the impact and magnitude of change with respect to spanwise flow components would provide more evidence to the effectiveness of riblets in more realistic flow fields.

Appendix A: Component Listing

Component	Model/Serial Number
Burst Spectrum Analyzers BSA 1 (green, 514.5 nm) BSA 2 (blue, 488 nm) BSA 3 (violet, 476.5 nm)	 Dantec 57N20 Enhanced Dantec 57N35 Enhanced Slave Dantec 57N35 Enhanced Slave
Transmitter	Dantec FiberFlow 60x41, S/N FF127
Beam Manipulators	Dantec 60x24
Photomultipliers (x3)	Dantec Photomultiplier 57x81
Laser (Argon-Ion)	1. Ion Laser Technology Model 5500A-00 (300 mW) 2. Coherent INNOVA® 70C series Ion Laser (2 Watt nominal)
Laser Probes 1-D 2-D Beam Expander (x2) Main Aperature Optics (x2)	 Dantec 60x10 Dantec 60x11 Dantec 55x12 Dantec 55x58 (f = 600 mm)
Color Separator	Dantec 55x35, S/N 9055x0353
Traverse System	Lightweight
Roscoe Fog Generator	Roscoe Model with Roscoe Fog Fluid
Atomizer	TSI model 9306, 6 jet
Computer	AST Pentium 166
Mass Flow Regulator	Grove Model 83, S/N 94710
Control Regulator	Grove Model 829 Pilot, S/N 11509
Upstream Pressure Gauge	American Instrument Corp. 25 x ¼ psi
Feedback Pressure Gauge	
Laser Power Meter	Coherent Fieldmaster Power/Energy Meter
Inclinometer	
Laser alignment plate	Dantec 9055x9551
Laser beam safety cover	Dantec 60x33
Probe supports (x2) One degree of freedom/adjustment Three degrees of freedom/adjustment	
Accelerometer	
3-D Coordinate Mapping Tool	
Feeler Gauge	

Appendix B: Transformation Matrix

B. Purpose

The purpose of the transformation matrix was to convert the measured velocity components to velocity components with respect to the wind tunnel. The need for the transformation arose from the angles and variation of the laser probe angles with respect to the test section of the wind tunnel. The transformation was handled similar to past methods by first considering probe orientation and then angle variations of the probes (Rothenflue, 1996). For this project, the probes were aligned with a 90° included angle between the beam centerlines (Figure B-1). The angles θ_1 and θ_2 were a nominal 45°.

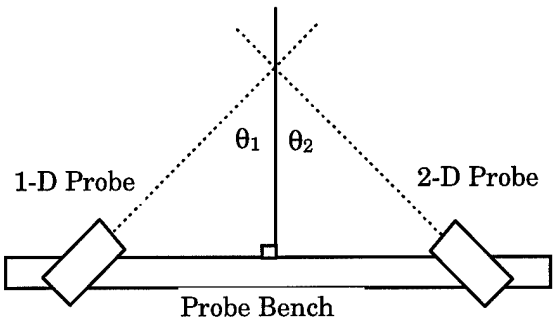

Figure B-1: Laser probe angles

The resulting measured velocity vectors were orthogonal (with the exception of small angle variations dealt with in the second step of this development). Figure B-2 shows the nominal orientation of the measured velocity vectors with the wind tunnel coordinate system. The measured vectors were resolved into wind tunnel velocity components (U, V, and W) by performing two angle rotations. After the components were resolved into the wind tunnel coordinates, the transformation included the angle variations about each of the coordinates axis.

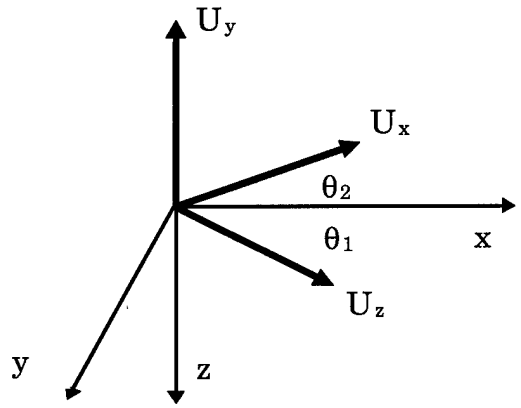

Figure B-2: Wind tunnel coordinate system with measured velocity vectors

B.1 Angle Rotations

In order to simplify the transformation process, the wind tunnel coordinate system was rotated to the measured velocity vector (optical) coordinates. This relationship was then inverted to provide the necessary transform from measured to tunnel systems. The first transform rotated the wind tunnel coordinate system about the z-axis through θ_2 degrees to align the x-axis with the U_x vector. Since this was a negative rotation about the z-axis, the resulting transform looked like:

$$\begin{bmatrix} x' \\ y' \\ z' \end{bmatrix} = \begin{bmatrix} -\cos(\theta_2) & 0 & \sin(\theta_2) \\ 0 & 1 & 0 \\ -\sin(\theta_2) & 0 & -\cos(\theta_2) \end{bmatrix} \begin{bmatrix} x \\ y \\ z \end{bmatrix} \tag{B-1}$$

with the primed coordinates as an intermediate coordinate system. The second rotation was a negative 90 degree rotation about the x-axis to align the transformed coordinates with the optical coordinates. This rotation was accomplished by

$$\begin{bmatrix} x'' \\ y'' \\ z'' \end{bmatrix} = \begin{bmatrix} 1 & 0 & 0 \\ 0 & 0 & -1 \\ 0 & 1 & 0 \end{bmatrix} \begin{bmatrix} x' \\ y' \\ z' \end{bmatrix} \tag{B-2}$$

To account for variations in θ_1 and θ_2, an angle relationship defined the z-axis in the optical system

$$\begin{bmatrix} x^* \\ y^* \\ z^* \end{bmatrix} = \begin{bmatrix} 1 & 0 & 0 \\ 0 & 1 & 0 \\ \cos(\theta_1+\theta_2) & 0 & \sin(\theta_1+\theta_2) \end{bmatrix} \tag{B-3}$$

with the stared coordinate system representing the optical coordinate system. When the three transformations were multiplied together, the resulting relationship was:

$$\begin{bmatrix} x^* \\ y^* \\ z^* \end{bmatrix} = \begin{bmatrix} -\cos(\theta_2) & \sin(\theta_2) & 0 \\ 0 & 0 & -1 \\ -\cos(\theta_2)\cos(\theta_1+\theta_2) & \sin(\theta_2)\cos(\theta_1+\theta_2) & 0 \\ -\sin(\theta_2)\sin(\theta_1+\theta_2) & -\cos(\theta_2)\sin(\theta_1+\theta_2) & \end{bmatrix} \begin{bmatrix} x \\ y \\ z \end{bmatrix} \tag{B-4}$$

To transform the measured velocity vectors to the wind tunnel coordinates, this matrix relationship was inverted to result in the rotation matrix R (Equation B-5)

$$R = \begin{bmatrix} \dfrac{-\cos(\theta_1+\theta_2)\sin(\theta_2)+\sin(\theta_1+\theta_2)\cos(\theta_2)}{\sin(\theta_1+\theta_2)} & 0 & \dfrac{-\sin(\theta_2)}{\sin(\theta_1+\theta_2)} \\ \dfrac{-\cos(\theta_1+\theta_2)\cos(\theta_2)-\sin(\theta_1+\theta_2)\sin(\theta_2)}{\sin(\theta_1+\theta_2)} & 0 & \dfrac{-\cos(\theta_2)}{\sin(\theta_1+\theta_2)} \\ 0 & -1 & 0 \end{bmatrix} \tag{B-5}$$

B.2 Angle Variations

Along with the transform, angle variations due to misalignment and laser adjustments were accounted for by considering a rotation about each axis. Positive rotations about z-, y-, and x-axes were represented by α, β, and γ. The resulting rotation matrices are Equations B-6, B-7 and B-8.

$$A = \begin{bmatrix} \cos(\alpha) & \sin(\alpha) & 0 \\ -\sin(\alpha) & \cos(\alpha) & 0 \\ 0 & 0 & 1 \end{bmatrix} \tag{B-6}$$

$$B = \begin{bmatrix} \cos(\beta) & 0 & -\sin(\beta) \\ 0 & 1 & 0 \\ \sin(\beta) & 0 & \cos(\beta) \end{bmatrix} \tag{B-7}$$

$$G = \begin{bmatrix} 1 & 0 & 0 \\ 0 & \cos(\gamma) & \sin(\gamma) \\ 0 & -\sin(\gamma) & \cos(\gamma) \end{bmatrix} \tag{B-8}$$

Multiplying these three matrices together provides the angle variation matrix T (Equation B-9).

$$T = \begin{bmatrix} \cos(\beta)\cos(\alpha) & \cos(\beta)\sin(\alpha) & -\sin(\beta) \\ \sin(\gamma)\sin(\beta)\cos(\alpha) & \sin(\gamma)\sin(\beta)\sin(\alpha) & \sin(\gamma)\cos(\beta) \\ -\cos(\gamma)\sin(\alpha) & +\cos(\gamma)\cos(\alpha) & \\ \cos(\gamma)\sin(\beta)\cos(\alpha) & \cos(\gamma)\sin(\beta)\sin(\alpha) & \cos(\gamma)\cos(\beta) \\ +\sin(\gamma)\sin(\alpha) & -\sin(\gamma)\cos(\alpha) & \end{bmatrix} \tag{B-9}$$

With the use of a digital inclinometer, these angles were measured fairly accurately. Adjustments could be made to the laser, traverse system, and wind tunnel to keep these variation angles below one degree for the entire investigation.

B.3 Total Relationship

The final relationship from the optical coordinate system to the wind tunnel coordinates is expressed by Equation 41.

$$\begin{bmatrix} U \\ V \\ W \end{bmatrix} = [T][R] \begin{bmatrix} U_x \\ U_y \\ U_z \end{bmatrix} \tag{B-10}$$

Appendix C: Laser Doppler Anemometry

C. Purpose

The Laser Doppler Anemometry (LDA) system allowed velocity measurements of the wind tunnel air flow without disturbing the actual flow often witnessed by other measuring techniques (hot wire, pitot pressure systems, etc.). It also has the ability to take measurements very close to walls and structures being tested. For these reasons, LDA was an ideal choice for measuring velocity components in the narrow riblet cavities in this investigation.

C.1 Measurement Volume

The LDA system created pairs of laser beams of the same wavelength and relative strength with the transmitter optics. One beam of each wavelength pair was shifted in frequency (with a 40 MHz signal to the Bragg Cell) and intersects the other beam at a known angle (θ) as shown in Figure C-2. The intersection defines the measurement volume (Figure C-1). This intersection is ellipsoidal in shape at approximately 150 x 150 x 250 μm. The size will vary slightly depending on the proper alignment of the beams.

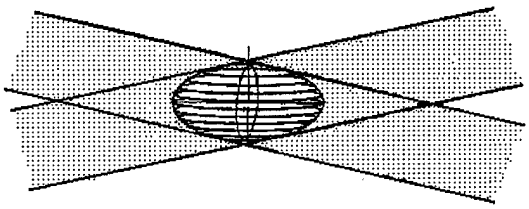

Figure C-1: Measurement volume

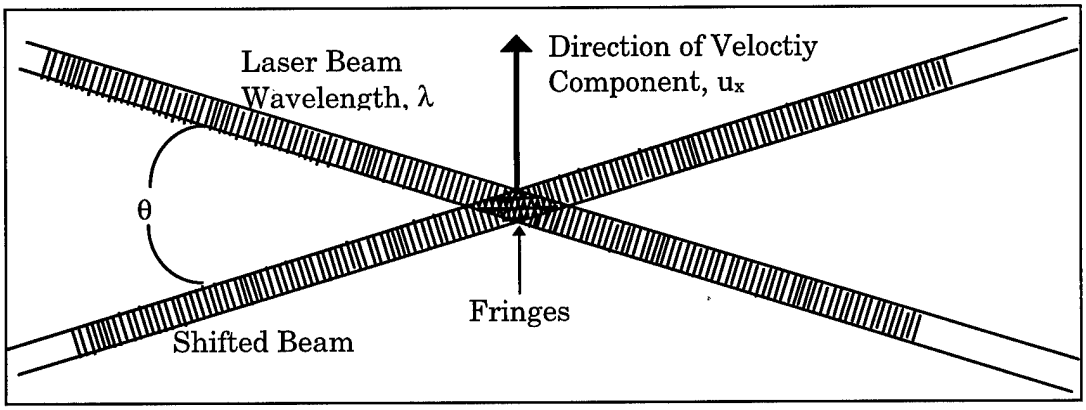

Figure C-2: Two laser beams intersecting

C.2 Doppler Bursts

As particles moved through the fringes in the measurement volume, light reflected in bursts at a specified Doppler frequency (f_D). The reflected light signal was directed by a Photomultiplier which converted the burst to an electrical signal. The signal was a frequency-modulated signal, Doppler burst (Dantec, 1990). The electrical signal was viewed on the oscilloscope and was used to help tune the optical probes. The Doppler frequency was related to the particle velocity by:

$$u_x = f_D \frac{\lambda/2}{\sin(\theta/2)} \qquad \text{(C-1)}$$

This relationship made it simple to determine the flow velocity once a particle traveled through the measurement volume. The result provided a one dimensional velocity component of a particle moving with the air flow. Care must be taken to seed the flow with particles small enough to move with the air itself. For this investigation, atomized olive oil provided sufficient seeding and served this purpose well for the atomizer. The particle size was approximately 0.6μm in diameter. The Roscoe Fog Machine used oil specifically designed for this purpose producing particles approximately 0.8 μm in diameter.

When trying to capture multiple velocity components, more pairs of laser beams were necessary. The 3-D LDA system used three pairs of beams. Each pair of beams were directed to individual Photomultipliers. Position of the receiving optics to the measurement volume was important. The optics can be positioned in either a forward scatter, greater than 90 degrees included angle, or back scatter mode, 90 degrees or less included angle. For this investigation, the back scatter method was employed due to access requirements of the measurement volume into the riblet valleys.

Appendix D: Tuning the LDA System

D. Overview

Tuning the LDA system refers to adjusting the laser and optics to provide optimal output in order to maximize data rates and accuracy. The primary objectives to obtain these results was to maximize the laser power being transmitted to the measurement volume and orient the beams to be incident on the same location in space. To accomplish these objectives, several steps were necessary. These included mounting the laser and transmitter to a bench, optimizing the laser output power, aligning the transmitter, focusing the laser into the fiber cables, and establishing the measurement volume. Several of these steps were one time operations, while others were daily events.

D.1 Mounting Laser and Transmitter to Mounting Bench

The laser and transmitter mounted to the bench using two clamps for each component. The laser was attached with the incident beam directed toward the transmitter inlet aperture. The transmitter was mounted approximately 15 cm from the laser. The laser was adjusted to ensure the beam is parallel to the bench and the beam entered the transmitter inlet aperture.

As part of the laser mounting (Coherent two Watt laser), the power supply was placed under the mounting bench. A water supply needed to be routed to the power supply to be used as the cooling source for the laser. This continuous-flow water supply provided sufficient cooling to remove the 13.5 kWatts of heat dissipated by the laser. The laser power supply used a three phase, 220 V circuit to generate the power necessary.

Mounting of the 300 mW laser was similar but simpler. This laser operated on a single phase 220 V power source and was air cooled. The laser was about one third the length and the power supply sat on the desk next to the mounting bench. The 300 mW laser tended to be fairly portable but power limited for this application.

D.2 Optimizing Laser Output Power

The 300 mW laser allowed for very little power optimization. There were two screws on the end of the laser which adjusted the mirrors inside the laser. These screws were limited to less than 90 degrees of rotation to prevent any possible damage to the mirrors. It also provided an adjustment for the laser power. The laser could be turned to a lower power setting to initially align the optics and prevent damaging any of the fiber cables. The mirrors were set at the factory to be optimized for the maximum output of the violet (476.5 nm) wavelength due to the low energy levels this Argon Ion laser produced.

The two Watt laser provided easier to use and more accessible adjustments. The power source had a control and status panel which sat next to the laser. The laser was turned on from this panel, and the power level could be adjusted as well. The laser provided an internal power meter to measure the laser output and determined the current used by the laser. These methods provided an accurate means to determine laser output. The power meter could be set to specific wavelengths within the laser's spectrum.

On the end of the laser was an optics adjustment and two mirror adjustment knobs. The optics adjustment allowed a reflecting optic to be positioned so the laser could be used for either single wavelength or for multiple bands. This investigation used multiple band mode. The two mirror adjustments were extremely sensitive but allowed the laser output power to be optimized by maximizing the laser power on the control panel at a specified wavelength.

D.3 Aligning the Transmitter

Transmitter alignment presented somewhat of a problem and became quite tedious. Initial alignment procedures provided by Dantec positioned the transmitter but did not account for other visible reflections from the laser. A Dantec technician, Craig Goulbourne (1997), determined the alignment mirror needed to be adjusted.

The laser power was set to a very low power setting for initial alignment. The incident laser beam entered the transmitter with the shutter at the inlet aperture directing the beam to the internal alignment mirror. Although a reflected beam was clearly visible, adjusting the transmitter to reflect this beam back into the laser was not possible due to the misalignment of the mirror. To properly align the laser, removal of the beam shield on the transmitter (between the manipulators) was necessary. Generation of flow visualization (Fog machine, humidifier, atomizer, etc.) showed the incident and reflected beams. Using the thumb wheel and position adjustments on the base of the transmitter, the reflected beam was directed along the same path as the incident beam. This ensured proper transmitter alignment.

D.4 Focusing the Laser into the Fiber Cables

Focusing the laser into the fiber cables involved several adjustments for each beam. After the beams were focused, a power balance for each beam pair was necessary. Initially, this involved adjusting the Bragg Cell level and the Bragg Cell itself. Once Bragg Cell settings were established for a given laser configuration and transmitter alignment, no further adjustments were necessary.

D.4.1 Beam Focusing

The manipulators attached to the transmitter directed the beams into the fiber plug. The fiber plug allowed for a focus adjust. With the optic cables and laser probes attached and in

place, adjustments ensured each of the laser beam power levels were maximized at the measurement volume. To ensure no damage occurred to the ends of the fiber optic cables, the laser was first reduced in power by the adjustment screw on the side of the laser or by the control panel for the two Watt laser. The laser was set to the minimum power levels while still being visible. The laser beams were initially set up to intersect by visual inspection. A power meter placed at the intersection of the beams provided the power levels. This limited the need to reposition the power meter for each individual beam. Closing the shutters on the manipulators turned off each of the beams. The shutter on the beam being adjusted was opened. Each beam was first maximized for power output by adjusting the focusing ring on the fiber plug.

The four adjustments on the manipulator were then adjusted in turn until each of them produced a maximum power level on the power meter readout. This process was often repeated several times until no more adjustments on the manipulator made any increases in the power output of the laser beam. The focusing ring was then readjusted. The focusing ring and manipulator adjustments were repeated until reaching a maximum power level. This process was accomplished for each of the six beams coming out of the manipulator. Adjustment times ranged from four hours initially to approximately 30 minutes.

D.4.2 Power Balance

The power balance involved three primary tasks, adjusting the Bragg Cell level, adjusting the Brag Cell, and defocusing the higher power beam of each pair. The Bragg Cell adjustments were based on a trend in the three pairs of beams. Since the violtet (476.5 nm) beams were the lowest powered beams, they established the setting for the Bragg Cell.

First, the power levels of the three pairs must be maximized. Due to fiber losses and differences in optics quality, the power levels of the beam pairs was different. The fiber plugs on the pair of beams were attached to the manipulators such that the three unshifted beams produced the higher power level. Proper book keeping was essential due to the fiber plug locations. The orientation of the beam pairs determined the velocity vector direction for each measured component. The transformation matrix in Appendix B was based on the resulting fiber plug orientation.

The Bragg Cell level adjust was first used to see if the power imbalance could be resolved. This adjustment was a slot screw in a hole on the back of the transmitter near the inlet aperture end. Since the power level of the violet needed to be maximized, this set of beams was monitored with the power meter. The level was adjusted until these beams were the same power. The level adjust could not equalize the power level, therefore the Bragg Cell needed to be adjusted.

The Bragg Cell adjustment was inside the transmitter. The housing near the inlet aperture end needed to be removed. The Bragg Cell adjustment was on the opposite side from the level adjust and used a hex wrench. Again, the violet beam pair balance determine the needed adjustments.

With the violet beams of equal power, the green and blue pairs needed some further adjustments. With the unshifted beams being of higher power, they were defocused using the focusing rings on the fiber plug until they provided the same power level as the shifted beams. The power levels between the beam pairs needed to be within 20% to ensure reliable readings at acceptable data rates (Wiseman, 1997).

D.4.3 Establishing The Measurement Volume

For the most reliable and accurate data, the LDA system configuration employed the off-axis back scatter measurement method. The receiving optics returned the return signal from the 2-D probe to the violet (476.5 nm) Photomultiplier , while the return signal from the 1-D probe went to the color separator and into the green (514.5 nm) and blue (488 nm) Photomultipliers. The focal length for both the transmitted beams and received bursts was 600 mm. For this reason, it was very important, that all six beams were able to intersect at a single point. An even more important reason for a single intersection was the ability to employ coincidence filtering on the data.

Coincidence filtering ensured the three pairs of beams all measured the velocity components from the same oil droplet passing through the measurement volume at the same time. This LDA system allowed for both hardware and software coincidence filtering to increase the reliability of the data. By forcing the collected data be from a coincident burst of light, the entire velocity vector of the air flow was known for that instant in time. The Burst Spectrum Analyzers performed a hardware filtering using BSA #1 as the master clock. The software filtering also increased the validity and accuracy of the data collected. The software ensured the burst from the three analyzers are within one millisecond of each other. This value can be adjusted to smaller values but provided little additional benefit for the data of this investigation.

To establish the measurement volume, the procedure was time consuming. Initially, the Dantec instructions suggest using a pin hole to align the beam intersection. This procedure did not necessarily provide a good intersection. A more efficient step to place the beams close was to adjust the measurement probes so the beams intersect by visual inspection.

This method was also preferred by the Dantec technician, Craig Goulbourne. The atomizer seeded the flow inside the test section and made the laser beams visible.

With the traverse system and laser beams adjusted with the intersection inside the test section and not close to any surfaces, the beams were further adjusted to take data. Initial flow seeding from the atomizer without any mass flow from the main air flow system provided sufficient means to further adjust the beams. An oscilloscope attached to BSA #1, Doppler output signal, monitored the return Doppler signal. The software settings in Burstware® were set to take data (High Voltage ON, etc.) The three axis adjustments on the 1-D measurement probe were then swept through ranges to find the location which would result in a burst signal on the scope. Each of the adjustments were optimized to increase the frequency and strength of the bursts being measured. To ensure a good measurement volume, the other two BSA Doppler signals were checked and fine tuning adjustments to the 1-D probe were made as necessary. Although the LDA setup took data a fairly good rates, the system was optimized further for even further refinement.

To adjust the measurement volume for the best data rate, mass flow through the tunnel was employed. A sufficient amount of air was blown through the tunnel (no specific mass flow target). With the computer monitor visible from the 1-D measurement probe, the three axis adjustments were manipulated in turn to increase data rates. The Burstware® software was set to the real time data screen. Although the data rates were somewhat erratic, large data rate changes were observed. The adjustments on the 1-D measurement probe micro-knobs were extremely sensitive for these adjustments. A slight movement could reduce the data rates dramatically. The three knobs each had varying sensitivity as well. The tilt adjustment on the back of the probe base was the most sensitive. Adjustments were often

performed with a pair of pliers to increase the moment arm and reduce the adjustment increment. The rotation about the axis of the base was the next sensitive. Changes in this adjustment were immediately seen in the data rates. The translational adjustment moving the probe toward the measurement volume was the least sensitive and proved to be difficult to adjust at times. Appreciable change in the data rate required large movements. The adjustment of the measurement volume was iterative. The adjustments on the three knobs were repeated until the data rates were maximized. This process could take several hours to accomplish. Eventually, acceptable data rates were obtained within only a few minutes.

D.4.4 Frequency

Those task needing to be accomplished more frequently included optimizing the laser output power, focusing the laser into the fiber cables, and establishing the measurement volume. Once the laser and transmitter were mounted and aligned, they needed no further adjustments unless being remounted (i.e. when the two Watt laser was introduced to the set up). The laser power from the 300 mW laser did not vary from the factory settings as measured by the direct measuring power meter. The two Watt laser could be monitored from the control panel continuously. Periodic checks provided indications (lower power output levels) when adjustments were necessary on this laser.

The two adjustments requiring more attention were the focusing of the laser into the fiber cables and the measurement volume. The focusing was performed as a daily routine before taking data. This task ensured laser power to the measurement volume was maximized and balanced between the pairs. The power levels were also observed while taking data. Operating the tunnel for several hours continuous often required the beams to be readjusted. With the beams visible in the seeded flow, relative intensities between each

beam pair were monitored. When one beam was excessively dimmer than the other, the power level was readjusted. Power differences between the beam pairs also reduced the overall data rate. Misalignments in the measurement volume affected the data rates as well. Adjustments to the measurement volume were not needed as often, though. As long as the probes were not disturbed, adjustments were infrequent. When data rates did diminish during a data acquisition phase, both focusing of the beams and measurement volume adjustments were checked.

D.5 Recommendations

Often much time can be lost when adjusting the LDA system, specifically the power levels and measurement volume. By using laser power levels and Doppler signal strength as goals, the objective of the project was obscured. Once a data rate was established, benefits existed for maximizing the rate but required more time to achieve than the benefits were worth. This investigation considered 1000 Hz data rates in the freestream to provide sufficiently reliable and timely data samples. While data rates as high as 2,500 Hz sustained were observed, these rates tended to stretch the limit of the atomizer. When taking the final data, the Roscoe Fog Generator was employed and could produce sustainable data rates over 6,000 Hz. To increase reliability in the data and average the readings over time better, the software settings were set to take data at rates near 2,000 Hz in the freestream.

Appendix E: Burstware® Software

E. Software Acquisition Parameters

The software program, Burstware®, had many important parameters which controlled the entire data acquisition and reduction process. These parameters were established in the four main areas of the software; Configuration, Setup and Acquisition, Process, and Presentation. . A definition of each of the parameters can be found in the Burstware® User's Manual (1990).

E.1 Configuration.

The configuration allowed the settings for a printer, the traverse system, and working directories. Of these, the traverse system was the most important. The traverse system settings included establishing one, two, and three axis movement systems. For this configuration, a three axis traverse system was used. The configuration section contained the traverse calibration and velocity settings as well. Maximum velocity settings for this traverse system were 25 and 40 mm/s. At these values, the traverse system vibrated for several seconds after each movement. For this reason, the velocity setting needed to be set at 1 mm/s. At this setting, the vibration in the traverse system damps out instantly. This was verified by attaching an accelerometer to the end of the 1-D probe and moving the traverse system. At the maximum traverse rates, the optic probes needed six seconds before the vibration damped out.

E.2 Setup and Acquisition.

The setup and acquisition section of the software required the most time and understanding of the different parameters which control the LDA system. This area of the program had many different menus. Important settings include the BSA settings, optic parameters, software filtering settings, traverse system control, and acquisition control.

E.2.1 BSA Settings.

The Burst Spectrum Analyzers (BSAs) have several primary settings. The menu settings appear as those in Table E-1

Table E-1: Burst spectrum analyzer parameters

Parameter	BSA #1	BSA #2	BSA #3
Velocity Units	m/s	m/s	m/s
Center Frequency (m/s)	4.	0.0	4.
Bandwidth (m/s)	6.92	8	8
Record Length (# of samples)	32	32	32
Signal Gain (dβ)	40	40	40
High Voltage (V)	1704	1704	1704
Pedestal Attenuation (dβ)	0	0	0
High Voltage ON	Yes	Yes	Yes

Settings for these parameters tended to be an iterative procedure. When taking data, the important aspect was to ensure the validity of the data remained high while trying to maximize the data measurement rates. Data rates were highly sensitive to the High Voltage and Signal Gain settings. The High Voltage was the amount of voltage sent to power the PM tubes to convert the Doppler signal to an electrical signal. These PM tubes could be set from 0 to 2004 V. The Signal Gain provided a similar function with settings from 0 to 57 dβ. A higher signal gain was necessary to get meaningful data and higher data rates but care had to be exercised to prevent noise being added to the signal. While monitoring the

Doppler signal on the oscilloscope, various values for the High Voltage and Signal Gain were tried. The values producing the lowest levels of constant noise and the largest amplitude Doppler bursts were used. The High Voltage values fell in the range between 1504 V and 17004 V. The corresponding Signal Gains ranged between 35 and 40 dβ.

Bandwidth and record length affected data rates as well. With larger bandwidths and record lengths, the data rate would be adversely affected. Although, the record length needed to be at least 32 (settings included 8, 16, 32 and 64) to ensure good and accurate data. The bandwidth was set to include the full range of expected velocities expected in the boundary layer profiles.. Typical bandwidths were on the order of 8.0 m/s. An appropriate center velocity was set to ensure the measured velocities remained within this bandwidth (i.e. the measured range was -1.0 to 7.0 m/s for most test runs).

E.2.2 Optics Parameters.

The optics parameters were used by the software to calculate the velocity parameters. Table E-2 shows the various parameters and settings used for this project.

Table E-2: Optics parameter settings

Parameter	BSA #1	BSA #2	BSA #3
Wavelength (nm)	514.5	488.0	476.5
Beam Separation (mm)	75	75	75
Focal Length (mm)	600	600	600

E.2.3 Software Coincidence and Filtering.

These settings were used to process the raw data into meaningful velocities. Table E-3 shows the parameters and settings used during this investigation.

Table E-3: Software coincidence and filtering settings

Parameter	BSA #1	BSA #2	BSA #3
Timer Clock	Master	Slave	Slave
Coincidence Mode	Master	Master	Master
Arrival timebase	Internal	Internal	Internal
Burst Detection	Both	Both	Both
Oversize Rejection	1	1	1
Buffer Mode	One Shot	One Shot	One Shot
Max. Anode Current (mA)	1.6	1.6	1.6
Quality Factor (%)	0	0	0
Collection Mode	Burst	Burst	Burst

The timer clock gave the BSAs a reference time for each to perform coincidence filtering. If set to the Private setting, each BSA would use it's own internal clock without performing any coincidence filtering. With the settings as shown in Table E-3, one BSA acts as the clock and the others use this clock to determine coincidence bursts with BSA #1. The coincidence mode settings include Master, Slave, and Private. With all three set to Master mode, the most amount of coincidence filtering possible was performed on the incident Doppler burst signal. All three BSAs had to record a Doppler burst at the same time stamp as determined by the Master BSA (BSA#1).

E.2.4 Traverse system control and positioning.

After establishing the software parameters, the traverse system control in the software program positioned the measurement volume at the initial data point. This investigation used three basic data acquisition profiles; boundary layer velocity profile, freestream velocity profile and grid profile (between the riblets). The freestream velocity profile started taking data at 80 mm in the x-direction and spanned to the 480 mm location, performed at 30 mm from the test plate. The boundary layer profile started at a point just off of the plate surface

(for both the flat plate and ribletted plate) and measured points at successive locations away from the plate in the y-direction. It was necessary to locate the surface within 0.1 mm.

E.3 Process

Processing the data allowed for further software filtering as well as coordinate transformations to laboratory coordinates. These settings established specific criteria with which to reduce the velocity data from the BSAs further into meaningful wind tunnel values. Once processed, the data was either exported to text files, further manipulated using various filtering methods, or viewed using the Burstware® presentation software.

The processing filtered the data to ensure valid data which coincided for all three channels (BSA #1, #2, and #3). This software coincidence filtering had several possible settings. Burstware® provided specific filtering schemes to be used for various different applications. Most of these schemes only provided complexity to the data processing and very little benefit. A standard coincidence scheme using a time based window to ensure the bursts measured by each of the BSAs were the same oil droplet was sufficient for this investigation. The window limited the coincidence to one millisecond for the processing of the Doppler bursts.

During the processing, converted data included three velocity components with corresponding variations, third moments (skewness), fourth moments (flatness), and cross moments (Reynold's stresses). The three velocity components were used to describe the flow characteristics, while the RMS values were used to calculated local turbulence levels. The raw data was converted to lab coordinates by inputting the transformation matrix as determined in Appendix A.

E.4 Presentation

The presentation ability of the software provided a good first look at the data to ensure proper shapes of the curves and low variability at each data point. Each BSA output at each data point could be viewed as well as the entire velocity profile for the data run.

For viewing 2-D profiles of the vector velocities, the presentation software proved to be extremely helpful. Since the primary interest was the velocity structures between the riblets, a vector map of the velocity components in the y-z wind tunnel coordinates system was necessary. Graphical representations of the grid profile provided clues as to the flow characteristics in the wind tunnel.

References

1. Bechert, D.W. and M. Bertenwerfer. "The Viscous Flow on Surfaces with Longitudinal Riblets," Journal of Fluid Mechanics, 206: 105-129 (1989).

2. Burstware® Users' Manual. DANTEC Measurement Technology, 1990.

3. Choi, Haecheon, Priz Moin, and John Kim. "Direct Numerical Simulation of Turbulent Flow Over Riblets," Journal of Fluid Mechanics, 255: 503-539 (1993).

4. Choi, Haecheon, Parviz Moin, and John Kim. "On the Effects of Riblets in Fully Developed Laminar Channel Flows," Phys. Fluids, A3: 1892-1897 (August 1991).

5. Dement, Franklin L. "Experimental Investigation of Adverse Pressure Gradient Effects on Vortex Formation over a Ribletted, Flat Plate," MS Thesis in Progress, School of Engineering, Air Force Institute of Technology (AU), Wright-Patterson AFB, OH, December, 1996.

6. Djenidi, L. and R.A. Antonia. "Laser Doppler Anemometer measurements of Turbulent Boundary Layer Over a Riblet Surface," AIAA Journal, 34: 1007-1012 (May 1996).

7. Goldstein, Richard J. Fluid Mechanics Measurements. Washington: Hemisphere Publishing Corporation, 1983.

8. Goulbourne, Craig. Dantec technician. Site visits, 1997.

9. Kiemele, Mark J. Basic Statistics: Tools for Continuous Improvement. Colorado Springs: Air Academy Press, 1990.

10. King, Paul I. "Chauvenet's Criteriaon for Rejecting a Reading,", class handout for SENG 516, Air Force Institute of Technology, Spring 1997.

11. Kreyszig, E. Advanced Engineering Mathematics. Seventh Edition, NY: John Wiley and Sons, 1988.

12. Niewstadt, F.T.M., W. Wolthers, H. Leijdens, K. Krishna Prasad, and A. Scharz-van Manen. "The Reduction of Skin Friction by Riblets Under the Influence of an Adverse Pressure Gradient," Experiments in Fluids, 15: 17-26 (1993).

13. Park, Seong-Ryong and James M. Wallace. "Flow Alterations and Drag Reduction by Riblets in a Turbulent Boundary Layer," AIAA Journal, 32: 31-38 (January 1994).

14. Rothenflue, James A. "Riblet Effects on Gortler Vortex Development Over a Concave Surface," PhD Dissertation. School of Engineering, Air Force Institute of Technology (AU), Wright-Patterson AFB OH, December, 1996.

15. Rothenflue, J.A. and P.I. King. "Vortex Development Over Flat Plate Riblets In a Transitioning Boundary Layer," AIAA Journal, 33: 1525-1526 (August 1995)

16. Rothenflue, James A. "Experimental Investigation Into the Effects of Riblets on Compressor Cascade Performance," MS Thesis, School of Engineering, Air Force Institute of Technology (AU), Wright-Patterson AFB, OH, December 1991.

17. Suzuki, Yuji and Nobuhide Kasagi. "Turbulent Drag Reduction Mechanism Above a Riblet Surface," AIAA Journal, 32: 1781-1790 (September 1994).

18. Vukoslavcevic, P., J.M. Wallace and J.L. Balint. "Viscous Drag Reduction Using Streamwise-Aligned Riblets," AIAA Journal, 30: 1119-1122 (April 1992).

19. Walsh, M.J. "Turbulent Boundary Layer Drag Reduction Using Riblets," AIAA Paper, 82-0169 (January 1982).

20. Walsh, M.J. "Riblets," in Viscous Drag Reduction in Boundary Layers, 123, Ed. D.M. Bushnell and J.N. Hefner. Washington, DC: , American Institute of Aeronautics and Astronautics, Inc., 1990.

21. White, Frank M. Viscous Fluid Flow. Second Edition, NY: McGraw-Hill, 1991.

22. Wiseman, Cliff. Dantec representative, phone interviews, 1997.

23. Wiseman, Cliff. An Informative Session on LDA and PDA Measurement Techniques. Mahwah: Dantec Measurement Technology, Spring 1997.

REPORT DOCUMENTATION PAGE

Form Approved
OMB No. 0704-0188

1. AGENCY USE ONLY *(Leave blank)*	2. REPORT DATE	3. REPORT TYPE AND DATES COVERED
	Nov 97	Final Master's Thesis

4. TITLE AND SUBTITLE
Velocity Profiles and Skin Friction in a Ribletted Flat Plate in Adverse Pressure Gradient

5. FUNDING NUMBERS

6. AUTHOR(S)
Richard D. Branam

7. PERFORMING ORGANIZATION NAME(S) AND ADDRESS(ES)
Ari Force Institute of Technology
WPAFB, OH 45433-6583

8. PERFORMING ORGANIZATION REPORT NUMBER
AFIT/GAE/ENY/97D-01

9. SPONSORING/MONITORING AGENCY NAME(S) AND ADDRESS(ES)
Dr. Richard Rivir, AFRL/POTT

10. SPONSORING/MONITORING AGENCY REPORT NUMBER

11. SUPPLEMENTARY NOTES

12a. DISTRIBUTION AVAILABILITY STATEMENT
Approved for public release; distribution unlimited.

12b. DISTRIBUTION CODE

13. ABSTRACT *(Maximum 200 words)*

This project investigated the flow field characteristics over a flat, ribletted plate and the effects of an adverse pressure gradient on this flow field. Testing examined the development of the flow over the ribletted plate from laminar through fully turbulent flow fields. The flow field states (laminar, transitional, and turbulent) were determined using local turbulence intensity values and boundary layer profiles. Several parameters were examined to help better describe the flow characteristics, boundary layer profiles, and influence on skin friction drag. The skin friction drag coefficients were calculated using a numerical integration technique to determine an average value and scaled to the planform area of the plate to compare results with smooth plate values. Although the geometry and flow conditions produced a drag augmenting case, skin friction followed trends described by the other flow parameters; streamwise velocity, Reynolds stress, etc. Other significant findings included boundary layer behavior and secondary velocity structures. The laminar boundary layers also conformed to a modified similarity solution. Secondary velocity stuctures were of further significance. The flow developed counter rotating vortices in the fully turbulent flow field but dissipated with increased adverse pressure gradient.

14. SUBJECT TERMS
riblets, ribletted plate, boundary layer, counter rotating vortices, LDA system, skin friction, adverse pressure gradient

15. NUMBER OF PAGES
175

16. PRICE CODE

17. SECURITY CLASSIFICATION OF REPORT	18. SECURITY CLASSIFICATION OF THIS PAGE	19. SECURITY CLASSIFICATION OF ABSTRACT	20. LIMITATION OF ABSTRACT
Unclassified	Unclassified	Unclassified	UL